UNIVERSITAT POLITÈCNICA DE CATALUNYA BARCELONATECH

Zirconium oxide conversion coating and biobased organic coatings for aluminum protection

Vitor Bonamigo Moreira

UFRGS
UNIVERSIDADE FEDERAL DO RIO GRANDE DO SUL

UNIVERSITAT POLITÈCNICA DE CATALUNYA
BARCELONATECH

Zirconium oxide conversion coating and bio-based organic coatings for aluminum protection

Vitor Bonamigo Moreira

Zirconium oxide conversion coating and bio-based organic coatings for aluminum protection

Vitor Bonamigo Moreira

Directors: Dr. Elaine Armelin (UPC)
Dr. Alvaro Meneguzzi (UFRGS)

Department of Chemical Engineering
Polytechnic University of Catalonia – UPC

Post-Graduation Program in Mining, Metallurgical and Materials Engineering – PPGE3M
Universidade Federal do Rio Grande do Sul – UFRGS

Barcelona and Porto Alegre, 2021

Acknowledgements

I would like to thank my supervisor at UPC, Prof. Elaine Armelin, for embracing this project when it was at its first steps and taking it to another level with her ambitious way of thinking. Her attitude and courage had a fundamental impact not only in the way I have carried out this work, but certainly in my professional and personal development.

I had the privilege of sharing the past 8 years of my academic career with my supervisor at UFRGS, Prof. Alvaro Meneguzzi. He will always be a role model for me both as a scientist and as a human being. His supportive behavior has given me the necessary audacity to experiment and try to reach bigger goals.

I thank all of my colleagues and professors at LACOR, IMEM and PSEP. They were the ones responsible for making these environments so pleasant places to work in and to teach me many important things for this work. More than results, my time in these laboratories has provided me friendship and numerous fulfilling experiences. Prof. Jane Zoppas and Dr. Henrique Piaggio deserve a special mention for their kindness in sharing their knowledge and experience and for providing valuable guidance at some points even without being directly involved in this work.

I am thankful to the Brazilian People that through its government has provided me 24 years of high quality education.

I feel fortunate to share more than the working space with Ina Keridou, who has the unmatched ability of cheering me up and making me believe things will always be fine. Her importance through the accomplishment of this work is unique and invaluable.

Thanks to my brother Manassés and my sister Letícia, who have been a safe harbor even during the hardest times. No distance can ever reduce the importance of both in my life.

There has never been, and there will never be, a single achievement in my life that is not shared with my mother Lúcia. Her unconditional support for my decisions has always made me feel safe to pursue my dreams.

To my father Ângelo, whose passing has left an unfillable void, instead of feeling sad for what the rest of our lives could have been, I will always be thankful for the 32 years we shared. This enlightened person, who has left an imprint in so many lives, has given me the privilege of being his son and I hope I can always be worthy of this.

Abstract

During the past century the way humans relate to the environment has undergone important changes, and currently it is a global consensus that our well-being should not be achieved at the expense of enlarging our footprint in the planet. The metal finishing industry is no exception to this trend. Because of that, there is the urgency to replace surface treatments such as chromate conversion coatings (CCC) or phosphating moving towards more sustainable technologies; as well as reducing the use of petroleum derivatives in the formulation of raw materials for the coatings and adhesives industries. A promising substitute for CCC are the zirconium oxide based conversion coatings (ZrCC), which have been under continuous development for nearly 30 years as a powerful tool for metal passivation with lower environmental impact. In this work, the electro-assisted deposition (EAD) technique was used to improve the ZrCC's deposition properties on aluminum substrates by stimulating electrochemically the coating formation, in a process that would typically be carried out relying exclusively in surface spontaneous reactions. On the other hand, this necessity of covering such passivation layer with organic coatings that act as long-term barrier protection against corrosion is another usual industrial process. Nevertheless, the constant generation of plastic waste has led to the need to search for sustainable, bio-degradable and/or recyclable polymers for replacing the essentially synthetic ones. In this way, the present thesis reports the production, characterization and application of thermoset epoxy polymers containing a bio-based epoxy prepolymer derived from limonene (PLCO) and industrial hardeners. For that, these results were compared to those of the traditional epoxy prepolymer diglycidyl ether of bisphenol A (DGEBA). The results indicate that PLCO has some enhanced properties in comparison to the synthetic epoxy polymer due to its chemical structure (a polymer with cyclic limonene units, carbonate groups and oxyrane) and its optimal molecular weight. The ZrCC layer is stable and adherent. Once combined with the epoxy derived from limonene it originates a dual layer with protective properties against the corrosion of aluminum, whilst the thermoset polymer could be used as a solvent-based adhesive for this same substrate. Therefore, this work approaches both environmental aspects of those new coatings and a complete characterization of all of the studied systems.

Resumen

A lo largo del último siglo la manera como la humanidad se relaciona con el medio ambiente ha sufrido cambios importantes y, actualmente, es un consenso global que nuestro bienestar no debe ser obtenido al coste de aumentar la huella negativa que dejamos en el planeta. La industria de acabado de metales no es una excepción a esta tendencia. Por ello, urge la sustitución de tratamientos de superficie, como los recubrimientos de conversión de cromados (CCC) o fosfatados, hacía tecnologías más sostenibles; así como urge reducir el uso de derivados del petróleo en la formulación de materia-primera para la industria de pinturas y adhesivos. Un sustituto prometedor para los CCC son los recubrimientos de conversión a base de óxido de zirconio (ZrCC), cuyos procesos se han ido desarrollando de forma continuada, alrededor de unos 30 años, como una potente alternativa de menor impacto ambiental para la pasivación de metales. En este trabajo, la técnica de deposición electro-asistida (EAD) fue empleada para mejorar las propiedades de deposición del ZrCC en substratos de aluminio, estimulando su generación electroquímicamente, en un proceso que típicamente sería realizado dependiendo exclusivamente de reacciones superficiales espontáneas. Por otro lado, la necesidad de recubrir esta capa pasivante con sistemas orgánicos que actúan de barrera eficaz a largo plazo contra la corrosión, es otro proceso industrial habitual. Sin embargo, la constante generación de residuos plásticos ha llevado también a la necesidad de buscar polímeros sostenibles, biodegradables y/o reciclables en sustitución a los esencialmente sintéticos. En este sentido, la presente tesis reporta la producción, caracterización y aplicación de polímeros epóxidos termoestables, conteniendo un prepolímero epóxido de origen natural derivado del limoneno (PLCO) y endurecedores comerciales. Para ello se ha comparado los resultados obtenidos con el prepolímero epóxido tradicional, conocido como diglycidyl ether of bisphenol A (DGEBA). Los resultados indican que el PLCO tiene algunas propiedades mejoradas con respecto a la resina epoxi sintética, gracias a su estructura química (un polímero con unidades cíclicas de limoneno, grupos carbonato y oxirano) y a su óptimo peso molecular. La capa pasivante de ZrO_2 es estable y adherente. Una vez combinada con la epoxi derivada del limoneno, da origen a un sistema dual de recubrimientos con buenas propiedades de protección del aluminio contra la corrosión, a la vez que el termoestable podría ser empleado como material adhesivo en base solvente para este mismo tipo de substrato. Por tanto, la presente memoria aborda tanto aspectos medioambientales de estos nuevos recubrimientos como una completa caracterización de todos los sistemas estudiados.

List of acronyms

^{1}H NMR	Proton nuclear magnetic resonance
1-MI	1-methylimidazole
AES	Auger electron spectroscopy
AFM	Atomic force microscopy
AHEW	Amine hydrogen equivalent weight
Al^{Me}	Aminotriphenolate Al(III) complex
ANOVA	Analysis of variance
CCC	Hexavalent chromate conversion coatings
CI	Confidence interval
CPE	Constant phase element
DC	Dip-coating
DCM	Dichloromethane
DETA	Diethylenetriamine
DFT	Dry film thickness
DGEBA	Bis-phenol A diglycidyl ether
DSC	Differential scanning calorimetry
EAD	Electro-assisted deposition
E_b	Breakdown potential
ECH	Epichlorohydrin
E_{corr}	Corrosion potential
EDX	Energy dispersive X-ray spectroscopy
EEC	Electrical equivalent circuit
EEW	Epoxy equivalent weight
EIS	Electrochemical impedance spectroscopy
ESO	Epoxidized soybean oil
FIB	Focused ion beam
FTIR	Fourier-transform infrared spectroscopy
GDOES	Glow discharge optical emission spectroscopy
HMMM	Hexa-methoxy methyl melamine
HR-SEM	High resolution scanning electron microscopy

HSB	Hue, saturation and brightness
ITO	Indium-tin oxide
j_{corr}	Corrosion current density
LCL	Lower confidence limit
LO	Limonene oxide
mCPBA	3-chlorobenzoperoxoic acid
MEK	Methyl ethyl ketone
OCP	Open circuit potential
OEM	Original equipment manufacturers
PC	New terpolymeric polycarbonate
PCO	Polycarbonate with two epoxy groups obtained by post-synthetic oxidation of PC
PEI	Polyethylenimine
PLC	Poly(limonene carbonate)
PLCO	Poly(limonene-8,9-oxide) carbonate
PLDC	Poly(limonene dicarbonate)
PPNCl	Bis-triphenylphosphine iminium chloride
PTFE	Polytetrafluoroethylene
REACH	Registration, Evaluation, Authorization and Restriction of Chemicals by the European Union
RGB	Red, green and blue
R_p	Polarization resistance
SCE	Saturated calomel electrode
SD	Standard deviation
SEM	Scanning electron microscopy
SHE	Standard hydrogen electrode
Si-NPs	Silica nanoparticles
TCP	Trivalent chromium process
T_d	Degradation temperature
T_g	Glass transition temperature
TGA	Thermogravimetric analysis
THF	Tetrahydrofuran

ToF-SIMS	Time-of-flight secondary ion mass spectrometry
UCL	Upper confidence limit
VCHO	Vinyl cyclohexene oxide
VOC	Volatile organic compounds
WCA	Water contact angle
XPS	X-ray photoelectron spectroscopy
XRF	X-ray fluorescence microscopy
ZrCC	Zirconium-based conversion coatings
Zr-DC	Zirconium-based conversion coating generated by dip-coating
Zr-EAD	Zirconium-based conversion coating generated by electro-assisted deposition

Table of contents

1. Introduction

1.1 *Conversion coatings on aluminum substrates*

A high strength to weight ratio and the ease of formability into complex shapes make aluminum a key metal for a wide range of industrial applications, with its durability and recyclability favoring its use as well. Additionally, its demand has continuously increased since the beginning of the XX century and it is expected to follow the same trend in the near future, as the use of lightweight materials is important in order to reduce the emissions in the transport sector. Interestingly, contrasting with this potential positive consequence of its applications, the production of aluminum raises concerns because of the use of non-renewable energy sources to supply the growing need for energy in this process.[1,2]

For most structural uses the mechanical properties of pure aluminum do not comply with the minimum requirements, therefore the use of alloying elements is important to widen the range of possible applications by tuning both composition and microstructure to obtain the desired characteristics. Most alloying elements have low solubility (> 1 %) in aluminum matrix, and their presence in aluminum produces second phase compounds, which act as microstructural agents. This formation of insoluble compounds is the core of the age-hardening treatments for aluminum, which can increase the yield strength of aluminum up to a factor of 80 compared to pure aluminum. The most used structural Al alloys are the Cu-rich (AA2000 series) and the Zn-rich (AA7000) ones.[2–4]

In a report from 1933,[5] Edwards and Wray already mentioned that the natural resistance of pure aluminum to atmospheric corrosion has not motivated significant research for its protection, but this scenario changed with the introduction of aluminum alloys, meaning that the benefits provided by the heterogeneous microstructure of these alloys do not come without a disadvantage.

In the case of pure aluminum, its naturally formed oxide layer when exposed to the atmosphere can provide corrosion resistance in mild environments, an effect that can be further improved in the anodizing process.[2,6] When the aluminum composition is altered with the use of alloying elements, the resultant phases, generally intermetallic particles, represent heterogeneities on the metal

surface. This may lead them to act as local galvanic cells, as the intermetallics may have different reactivity from the aluminum matrix.[7–10] The presence of such intermetallics may also hinder the protection provided by the aluminum oxide with the alloying elements incorporation in the oxide layer, generating defects.[10] The combination of such conditions creates the need for corrosion protection of aluminum alloys when an extended lifespan is desired.

The structure of the aluminum oxide layer is known to be porous. Therefore, sealing the oxide pores is a widely used method to improve the layer's properties.[10–13] Although other surface treatments, such as thermal sealing[12] and phosphate-based coatings,[14] may be used for this purpose, **hexavalent chromate conversion coatings (CCC)** have been successfully used for decades in high responsibility applications, such as the aircraft and automotive industries, providing corrosion protection as well as paint adhesion, and to this date it remains the benchmark surface treatment for other conversion coating systems used in aluminum protection.[3,10]

Although their first uses can be traced back to the beginning of the XX century, modern CCC are dated from the late 1940's, when these surface treatments started to be carried out at near room temperature and at shorter times (ranging from seconds to several minutes). This evolution relied mainly on the use of **surface activators**, such as the fluoride ion, and accelerators, leading to a diversity of formulations in commercially available baths. These additions to the bath could improve film thickness to a factor of at least 30, resulting in major improvements in corrosion protection.[14]

The formation of CCC is not the simple deposition of a chromate-containing film on the substrate. The conversion coating procedure starts with the oxidation of the metallic substrate, and its cathodic half reaction locally increases the pH on the cathodic sites of the surface through dissolved oxygen reduction or water reduction reactions. This pH shift results in the precipitation of the dissolved metals in oxide or hydroxide form, and the generated film containing elements from both the bath and the substrate, with a gradient of substrate concentration being observed along the conversion coating thickness. This lack of a clear

metal/coating interface creates satisfactory film adhesion.[14] A simplified scheme is shown in **Figure 1.1.1** in order to illustrate the complex set of chemical reactions taking place in the CCC formation.[14,15]

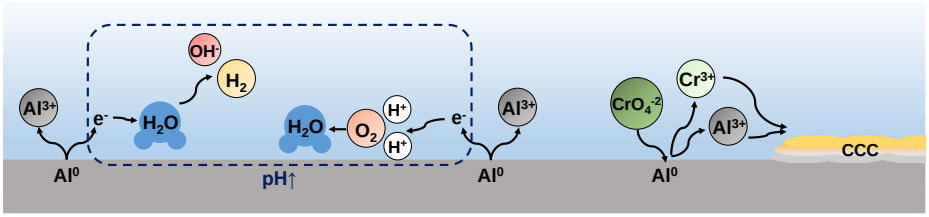

Figure 1.1.1. Deposition mechanism of chromate conversion coatings on aluminum. The species sizes and abundance do not necessarily represent the actual dimentions and concentration. Arbitrary scale.

The protection provided by CCC combines a barrier effect of the insoluble Cr^{3+} oxides/hydroxides, which are the main components of the coating, and a self-healing effect generated by the presence of highly soluble Cr^{6+} ions enclosed in the film. When these chromate ions diffuse in aqueous electrolytes and react with the exposed metal they can be electrochemically reduced to their trivalent state, regenerating the protective layer in damaged areas.[3,16] This is the widely known self-healing effect promoted by CCC technology, commented above, and nowadays there is no alternative as efficient as CCC in the market. In addition to the corrosion protection, chromate films promote the adhesion of organic coatings by enabling mechanical interlocking, in case the coating has a crackled morphology, and offering reactive area for acid-base interactions and hydrogen bonds, providing both physical and chemical mechanisms for paint adhesion.[15]

Despite their excellent performance in both corrosion protection and promotion of paint adhesion with cost-effectiveness, CCC are expected to be replaced by other surface treatments in the near future, and have already been banished in some industrial applications. This happens because of the environmental concern that the use of CCC generates,[17] which will be briefly discussed in the next section.

1.1.1 Environmental and health hazards associated to chromate conversion coatings

The risks related to hexavalent chromate ions have been identified since the 1920's, and workers in direct contact with chromate-containing compounds have shown relatively high incidence of nose and lung cancer.[17,18] A report from 1890 already evidenced the development of cancer by a worker exposed to chrome pigment, as well as a perforation in his nasal septum, which was also observed in some of his co-workers, and it is the first documented case of cancer associated to chrome exposure.[19] Surprisingly, it was not until the 1970's and the 1980's that the health and environmental hazards caused by such substances have been officially reported by the World Health Organization.[17]

The two most important oxidation states of chromium regarding human health and the environment are the trivalent and the hexavalent ones. Whilst the trivalent state is considered non-toxic, being necessary for the normal development of animals, including human beings, the hexavalent one is harmful.[20,21] Trivalent chromate compounds have limited solubility, contrasting with the high solubility and activity of its hexavalent counterpart.[22,23] This has been mentioned as the combination of characteristics that promotes the notable self-healing ability of CCC, but ironically it is the main drawback in CCC current use.

Besides the direct contamination of workers in industrial processes, water sources may be contaminated with chromate-containing wastewater. Regardless of the route of exposure, chromate easily penetrates the cells via anion-exchange channels due to its similarity to sulphate and phosphate molecules. This may result in the accumulation of chromate in living organisms and hinder their vital functions, because its reduction to the trivalent state inside the cells generates reactive intermediates that cause cytotoxicity[I] and genotoxicity[II]. This way, the

[I] Cytotoxicity: cell death caused by direct contact or leaching of toxic substances assessed through an *in vitro* test.[127]

[II] Genotoxicity: capability of a compound to cause alteration in the genetic information within a living organism.[128]

harmful character of Cr^{6+} originates mainly from its ability to penetrate the cells.[24,25]

This combination of factors is the driving force for the replacement of CCC, but despite decades of global research, no universal alternative has been developed to match the CCC's properties yet. While some industries may apply alternative treatments with inferior properties, fields with stricter demands of performance and safety cannot afford the same concessions. In the aircraft industry, for instance, workers are exposed to chromate-containing vapor or dust inhalation during the production, maintenance and removal of coatings and there is still an unsupplied necessity for harmless efficient aluminum pretreatments.[26] This causes not only the obvious health hazard for the workers, but also the extra expense for obtaining the authorization by regulatory agencies to continue using this restricted surface treatment for a limited time.[17]

The ongoing search for efficient alternatives has already brought to light many surface treatments. One of these being the **trivalent chromium process (TCP)**, consisting of a conversion bath containing trivalent chromium and zirconium as the main precursors for film formation. It has a low concentration, if any, of chromium in the hexavalent state, which may comply with regulation at the expense of performance, as the self-healing ability is sacrificed.[17,27] It may also face environmental restrictions in the future because of the suspicion of genotoxicity and carcinogenicity of some Cr^{3+} compounds, making it a non-ideal alternative for the complete replacement of CCC.[3,17]

As noticed, the requirements are high on performance, cost-effectiveness and environmental/health concerns,[28] so other studied pretreatments, such as silanes,[29] rare earth metals,[30,31] vanadate,[32] titanium[28,33] and lithium-based[34,35] coatings, have not yet succeeded in fulfilling all the necessities. In the present work, another studied coating for chromate replacement in aluminum alloy surfaces will be approached. One that has already reached performance levels that enabled its commercial use in industry but has still need of further development:[28,36,37] the **zirconium-based conversion coatings (ZrCC)**.

1.1.2 Zirconium-based conversion coatings

As mentioned in the previous section, the CCC technology had great improvements in the 1940's that led to the consolidation of CCC in modern industry. Among these improvements was the addition of fluorine, which acted as a surface activator by decreasing the interfacial tension of the native aluminum oxide, and **hexafluorozirconates** were used with this purpose since the 1950's.[38] However, it was not until two decades later that they would be used as the main component of a protective film.

J. W. Davis, in his technical paper from 1983,[39] already made reference to zirconium-based conversion coatings being used as a replacement for CCC for aluminum protection, with the technology being developed through the 1970's and further refined in the early 1980's. This culminated with the registration of patents that enabled the establishment of commercial treatments based in hexafluorozirconate in that decade.[28] The interest in the topic has motivated the publication of scientific research articles in a growing number through the 1990's and maintains its relevance until the present days.

Although some studies used baths containing dipotassium hexafluoro compounds or other zirconium salts for the production of ZrCC, the most common precursor in the literature is the **hexafluorozirconic acid (H_2ZrF_6)**. These precursors are the source of zirconate for the coating formation. In addition to the precursor, the typical aqueous conversion bath contains acids or bases in order to adjust the solution pH, which has an important role in the coating formation. Bath additives may be present in the bath as well, not only in commercial products but also in research works. These additives are used for improving film formation, its structure (control of coating porosity, crystallinity, etc.) and characteristics such as paint adhesion (decreasing the surface tension energy, increasing the surface interfacial forces, etc.) or corrosion inhibition (promoting self-healing effect, higher impermeability to electrolytes, etc.).[28,37]

When an aluminum substrate is immersed in the conversion bath it undergoes an attack by the hexafluoride ions, causing a partial dissolution of the native aluminum oxide layer due to the following reaction:[28]

$$Al^{3+} + ZrF_6^{2-} \rightarrow AlF_6^{3-} + Zr^{4+} \quad \textbf{(1.1)}$$

Meanwhile, on cathodic sites of the substrate, oxygen dissolved in the solution is reduced and hydrogen evolution is observed, shifting the local pH to higher values (alkaline):[40]

$$O_2 + 4H^+ + 4e^- \rightarrow 2H_2O \quad \textbf{(1.2)}$$

$$2H^+ + 2e^- \rightarrow H_2 \quad \textbf{(1.3)}$$

The cathodic sites of aluminum substrates are usually intermetallic particles originated in the alloying process, as mentioned in section 1.1. The most relevant intermetallic particles for this phenomenon in the AA2000 series are the ones containing Cu, such as S-phase (Al_2CuMg) and theta phase (Al_2Cu),[10,41,42] because their cathodic character relative to the aluminum matrix provides more active sites on the metallic surface for the **Equations (1.2)** and **(1.3)** to happen.[8,28,43,44]

The local pH increase stimulates the precipitation of hydrated zirconium oxides from the zirconate complexes in the bath, which are stable at a limited range of pH depending on the specimens' concentration and the temperature.[40,45] Cardoso, Rapacki and Ferreira[45] concluded that with a Zr^{4+} concentration of 4 mmol/L, at 25 ºC, a shift to pH 4 would induce the precipitation of the film. This happens due to the hydrolysis of the fluorometalates in the solution. Two commonly proposed deposition reactions are:[28,40,45,46]

$$ZrF_6^{-2} + 4OH^- \rightarrow ZrO_2 \,.\, 2H_2O + 6F^- \quad \textbf{(1.4)}$$

$$Zr^{4+} + 4H_2O \rightarrow ZrO_2 \,.\, 2H_2O + 4H^+ \quad \textbf{(1.5)}$$

Despite the simplicity of the reaction proposed above, the precipitation of the Zr-based coating probably occurs through a more complex mechanism, with the formation of intermediate products and generating hydrated oxyhydroxides. Verdier and coworkers have proposed the following steps for the film deposition:[47]

a) The Zr^{+4} ions hydrolyses with the local pH increase forming $[Zr(OH)(OH_2)_7]^{3+}$;

b) Further hydrolysis generates $[Zr(OH)_2(OH_2)_6]^{2+}$;

c) The olation[III] of the latter produces the cyclic polycation $[Zr_4(OH)_8(OH_2)_{16}]^{8+}$, which is stable in aqueous solution;

d) This polycation then forms a gelatinous compound, $ZrO_{2-x}(OH)_{2x}\cdot_y H_2O$ or it may undergo oxolation[IV] to form hydrated ZrO_2 with different levels of hydration.

Considering the simplified mechanism proposed on **Equation (1.4)**, the pH increase resulting from the substrate attack leaves the reaction unbalanced, with an excess of one of its reagents (OH^-). According to Le Chatelier's principle, the system would respond to this unbalance with the generation of more products, namely the Zr compounds that form the ZrCC.

The resulting coating is composed mainly of hydrated zirconium oxyhydroxides (ZrO_2; $ZrO_2 \cdot 2H_2O$; $ZrO_{2-x}(OH)_{2x} \cdot nH_2O$) and it may contain fluorine compounds (ZrF_4; $AlOF^-$; ZrO_xF_y) as well.[8,28,47,48] Studies of the composition of the coatings along its depth profile have indicated that there is not a clear interface between the underlying substrate and a homogeneous ZrCC layer. They observed a concentration gradient across the coating, with a decreasing content of Zr atoms towards the core of the substrate, i.e. in the interface metal-coating; with a simultaneous increase of Zr atoms concentration in the outer coating layer.[49–52] This is a consequence of the film formation mechanism, which depends on a substrate interaction with the solution in order to enable the precipitation of the Zr-compounds, unlike methods of more straightforward coating deposition such as painting or electrodeposition.

ZrCC films tend to reproduce the substrate topography, with the coating being typically formed by spheroidal zirconium oxide particles.[48,50,53] As the

[III] Olation: the formation of polymeric oxides from metal ions in an aqueous solution through μ-(OH) bridges.[129]

[IV] Oxolation: the formation of an oxo bridge (—O—) between two metal centers in a condensation reaction.[130]

coatings' thicknesses are usually under 100 nm,[28] they are not expected to level irregularities such as machining or polishing grooves.

These coatings provide moderate corrosion protection,[28] mostly by blocking the active sites on the surface, affording barrier protection against corrosive electrolytes because of the ceramic nature of the film. This is a result of the deposition mechanism of ZrCC, with the precipitation of the coating starting on the localized galvanic couples of the surface.[54,55] An unusual self-sealing effect was observed by Šekularac using hexafluorozirconic acid for treating Si-rich (AlSi7Mg0.3)[51] and a Mn-rich (AA3005)[56] aluminum alloys in a phenomenon that has not been further explored or observed by other authors and may be important for future improvements and applications of ZrCC.

Although some corrosion protection is provided, the nanometric scale of the film thickness limits the impermeability and homogeneity of the films. The main role of these conversion coatings should be the promotion of the adherence of further organic coatings layers.[28]

The paint adherence provided by such pretreatments can be based on two basic mechanisms: physical adherence and chemical adherence. For the physical adherence to happen the surface must have its roughness altered in a way that mechanical interlocking between the pretreatment and the organic coating would occur. Given the size of the formed particles and the way the film reproduces the metal texture, this should not be the main mechanism for paint adhesion on ZrCC. A more significant effect can be expected by the chemical mechanism, as it has already been observed that ZrCC increase surface free energy, enhance interfacial acid-base interactions and improve the surface hydroxyl fraction, enabling a higher amount of secondary bonds in the metal/paint interface.[57–61]

The factors that affect ZrCC film formation in metallic substrates have been studied by several authors along the past decades, being the **concentration of the bath**, the **pH** and the **immersion time** the most influential ones. Other parameters, such as temperature[62–64] and agitation,[43] have also been assessed.

Regarding concentration, it has been found to be a determinant factor for the film formation. There is no direct relation between higher H_2ZrF_6 concentrations and more efficient film deposition.[47] In fact, the concentration must be dialed to an intermediate that should provide enough acid for the initial attack of the metal to occur without being an excessively aggressive medium for the film stability. This way, typical H_2ZrF_6 concentrations are within a range between 0.5 and 5 mmol/L.[28,65]

The bath pH also has an important role, as the film deposition has been proved to be a pH driven process. The pH of the solution should be slightly lower than the limit of solubility of the Zr^{4+} compounds, maintaining the solution's stability and avoiding the undesired precipitation of the coating components in the bath container without offering an excess of acidity that could neutralize the pH increase in the surface or promote the coating's dissolution. Most authors reported as satisfactory pH values between 2.5 and 4.5.[45,47,62,63]

During the immersion of the substrate in the precursor solution, it has been observed that in the first 30 to 100 seconds there is an intense surface activation with the native oxide dissolution, followed by the formation of clusters of Zr compounds, which grow laterally throughout time to form the film.[51,58,66] In a similar way to the precursor concentration, the time of immersion must be optimized in order to avoid film growth to disproportionate thicknesses. Because of the coating ceramic character, an increase in the thickness and the size of the zirconium oxide clusters may also increase the films brittleness. The result of this undesired effect is the formation of cracked films as the hydrated compounds gradually dehydrate. Typical deposition times do not exceed 10 minutes.[28,48,51]

The simplicity of the film production process and the promising results regarding corrosion protection and paint adhesion make **ZrCC an important alternative** for conventional surface pretreatments such as CCC or phosphate conversion coatings, but there are still issues to be tackled, such as the lack of a consistent self-healing ability, the limited thickness, the restricted homogeneity of the films and the dependence on surface metallurgy. Only when these issues are completely elucidated ZrCC could be set as a universal replacement for CCC.

1.1.3 Electro-assisted deposition (EAD) technique

As the spontaneous mechanism of deposition of the ZrCC films depends exclusively on surface interactions between the substrate and the compounds present in the conversion bath, one possibility of improving film formation would be to give an extra driving force for the zirconium oxides and hydroxides to precipitate. One common additive that is present in commercial products and is used to improve the deposition is Cu,[8,37] as it will precipitate on the aluminum surface and generate more localized galvanic couples for the film formation to happen. Another approach would be to, instead of tackling the initiation of the deposition reactions as done with Cu, focus on the precipitation reaction of ZrCC (Equation 5). This reaction balance could be disturbed by changing the components' concentration on the active sites, using Le Chatelier's principle to predict the outcome.[67]

Analyzing the mentioned reaction, the availability of Zr^{4+} complexes cannot be drastically increased because of the limitation regarding the concentration of hexafluorozirconic acid, discussed in section 0. The precipitated products do not affect the chemical equilibrium because they are in solid phase, and water does not influence it because it is a pure liquid reagent. This leaves the possibility of decreasing the H^+ concentration, consuming a product of the reaction in order to promote products formation. The consumption of H^+ can be easily achieved with the electrolysis of water, which occurs according to the two following reactions when in acidic medium:[68–70]

$$\text{Anodic reaction: } H_2O \rightarrow 2H^+ + \tfrac{1}{2}O_2 + 2e \qquad \textbf{(1.6)}$$

$$\text{Cathodic reaction: } 2H^+ + 2e^- \rightarrow H_2 \qquad \textbf{(1.7)}$$

The hydrogen evolution in the cathodic reaction (**Equation 1.7**) can be the source of perturbation in the precipitation equilibrium. This would enable the precipitation reaction to happen not only in the localized galvanic couples in the substrate, but in the entire substrate if it is set as a cathode in an electrochemical cell with an inert counter electrode and the conversion bath being the electrolyte. This advantage is expected to provide films with controllable thickness and

homogeneity, [69,71,72] which is of great importance for corrosion protection applications.

This electrochemical procedure is called **electro-assisted deposition (EAD)**, and it differs from electrophoretic deposition methods because it does not imply the reduction of an ion to its metallic state. Instead of providing electrons for a metallic ion to reduce, as done in the electrodeposition of metals, for instance, the applied potential will stimulate the generation of a favorable condition for the film deposition, namely by increasing the pH, in a mechanism driven by electrochemical reactions.[73]

This technique has been studied for various coating procedures that are benefited by this local pH increase.[73] Shacham, Avnir and Mandler, in a study focused on the EAD of silane films.[71] They proved that the pH on the surface of the substrate could shift from 3.5 to more than 8.2 with the application of an overpotential of −1.3 V. Comparing this pH with the values observed on the surface of metallic substrates when depositing Zr-based films by dip-coating[40,45] it should be enough to stimulate the ZrCC deposition. Additionally, this study was carried out using indium-tin oxide (ITO) substrates, giving an indication that this technique may also enable the deposition of the coatings on substrates that would not undergo the necessary reactions for the initiation of the film precipitation process (*i.e.*, in conductive ceramic materials).

The use of the EAD technique adds one critical factor for the film deposition in comparison with the conventional dip-coating procedure, which is the overpotential that is applied on the electrochemical cell. Although high overpotentials would be expected to improve film formation, the consequent hydrogen evolution may have a detrimental effect on the coating integrity. Excessive hydrogen formation may produce failures on the coating's structure such as holes or cracks, and it may happen due to the use of excessively cathodic overpotentials or long generation times.[48,74]

Gal-Or, Silberman and Chain[75,76] have generated ZrO_2 films on both graphite and titanium substrates from the precursor $ZrO(NO_3)\cdot nH_2O$ in a galvanostatic

regime. They have detected a direct relation between the applied current density and the thickness of the films, but the crackled morphology of these films indicated that the excessive thickness led to film brittleness.

In a study dedicated to the formation of ZrO_2 films on Co-Cr alloys for dental applications,[74] Hsu and Yen used aqueous $ZrO(NO_3)_2$ and a potentiostatic approach. They have observed that excessively cathodic potentials may hinder the coating integrity because of the hydrogen evolution, therefore films generated at -0.7 V_{SCE} were more efficient than the ones generated at -1.5 V_{SCE} for corrosion protection in artificial saliva.

Using the same precursor solution as in his previous work,[74] Yen and coworkers have carried out the EAD method on AISI 316L stainless steel,[77] titanium,[78] and ASTM F-75 Co-Cr-Mo alloy[79] substrates with satisfactory corrosion protection. Special attention was dedicated to the film annealing, with the coatings undergoing thermal treatments in temperatures ranging from 250 to 900 °C. He observed that the film thickness could not exceed 0.2 μm in order to avoid film cracking during the annealing procedure. Even though the authors do not mention it, the annealing of coatings on metallic substrates should be studied taking into account the microstructural changes that the metal may undergo. For the aluminum alloy AA2024-T3 and other alloys in the AA2XXX series, for instance, artificial ageing heat treatments are carried out in temperatures around 200 °C,[80,81] so the annealing of the zirconium-based coating with these substrates at such temperatures might undesirably affect the properties of the metal.

Shacham and coworkers, who had already used EAD for the deposition of silane films,[71] extended their expertise to the deposition of zirconia thin films from zirconium tetra-n-propoxide solution on ITO and gold substrates.[69] They observed that the deposition potential influences the thickness of the coating, with more negative potentials resulting in thicker films. Another studied parameter was the deposition time, and it has been observed that the film growth is fast in the first 10 minutes of deposition, but for longer periods, the thickness reaches a nearly steady plateau. According to the authors this happens because the film itself acts as a barrier for the diffusion of the reactive species, therefore the proposed

mechanism would be adequate for the deposition of coatings on a nanometer scale on conductive substrates.

Giacomelli *et al.*[82] used a $ZrOCl_2 . 8H_2O$ solution to produce EAD zirconia films on NiTi alloy in a pontentiostatic procedure. The films were amorphous, which is in agreement with previous reports of similar coatings produced at room temperature,[76,77] and provided corrosion protection by increasing the breakdown potential of the passive layer. The authors also reported the inefficiency of using excessively high potentials as they increase hydrogen evolution, causing the appearance of porosity in such passive layers.

Trivalent Chromium Process (TCP) is a non-chromate conversion coating with a similar deposition mechanism as described above and which commercial composition is based on zirconium and trivalent chromium, resulting in the formation of hydrated zirconia films containing $Cr(OH)_3$.[54] Dong *et al.*[83] have observed that the use of EAD in TCP resulted in thicker and denser films when compared to the simple immersion or dip-coating process. Therefore, the conventional process used for the film deposition is self-limiting, because the growth of the coating reduces the available area for reacting with the conversion solution. Another report from the same research group focused on corrosion study of pure aluminum substrates[68] and revealed that the film acts as a barrier providing corrosion protection, remaining passive below the pitting potential in Cl^--rich medium. Once the pitting potential is reached, the films are degraded and the underlying substrate is oxidized.

Qi *et. al.*[84] have also studied the use of the EAD technique with a Cr(III)-based coating containing zirconium with exclusive interest in understanding the influence of the deposition potential in the valence of the chromium present in the coating. Their report evidences the transition of some of the trivalent chromium ions to the hexavalent form depending on the applied potential. Although this can add improved properties to the film it may generate concern about the presence of Cr(VI).

A summary of the previously reported main conditions for the Zr-based films formation by EAD is presented in **Table 1.1.1**.

Table 1.1.1. Summary of conditions for EAD of Zr-based coatings on various substrates.

Substrate	Zr-containing solution	Deposition conditions	Reference
Graphite and titanium	0.1 M $ZrO(NO_3)$. nH_2O; pH = 2.3	Galvanostatic (15 to 100 mA/cm²); 10 to 60 minutes	75,76
Co-Cr alloy	0.0625 M $ZrO(NO_3)_2$; pH = 2.46	Potentiostatic (− 0.7 V_{SCE} and − 1.5 V_{SCE}); 500 seconds	74
AISI 316L stainless steel	0.0125 M, 0.00625 M and 0.003125 M $ZrO(NO_3)_2$; pH = 2.25, 2.5 and 2.7	Potentiostatic (− 0.85 V_{SCE}); 500 seconds	77
Titanium	0.0125 M $ZrO(NO_3)_2$; pH = 2.2	Galvanostatic (0.5 to 40 mA/cm²); 5 to 50 minutes	78
ASTM F-75 Co-Cr-Mo alloy	0.0625 M $ZrO(NO_3)_2$; pH = 2.2	Galvanostatic (2 mA/cm²); 500 seconds	79
ITO and gold	1.12 M zirconium tetra-n-propoxide with 0.1 M $LiClO_4$ in 2-propanol with variable amounts of water (until 900 ppm)	Potentiostatic (+ 2.5 V_{SHE} to − 1.5 V_{SHE}); 0.5 to 90 minutes	69
Nickel and nickel/yttria-stabilized zirconia composite	0.5 mM to 10 mM $ZrOCl_2$; pH not reported	Galvanostatic (1 to 10 mA/cm²); 8 minutes	72
Equiatomic NiTi alloy	0.0625 M $ZrOCl_2$. $8H_2O$; pH = 1.8	Potentiostatic (− 0.65 V_{SCE} to − 1.6 V_{SCE}); 15 to 40 minutes	82
AA2024 aluminum alloy	TCP commercial solution; pH = 3.75	Potentiostatic (− 1.55 V_{SHE}); 1, 2 and 4 minutes	83

Aluminum	0.002 M $KCr(SO_4)_2$ and 0.003 M K_2ZrF_6; pH = 3.5	Potentiostatic (− 1.25 V_{SCE} and − 1.5 V_{SCE}); pH = 3.5	68
Aluminum	Commercial Cr(III) bath containing Zr; pH = 3.9	Potentiostatic (− 0.5 V_{SCE} and − 1.5 V_{SCE}); 20 and 40 minutes	84

Notes: SCE = Saturated Calomel Electrode; SHE = Standard Hydrogen Electrode

Despite the positive effects on the coatings' properties and the possibility of depositing Zr-based films in multiple conductive electrodes that other researchers have noticed, there are two important aspects that have not been previously explored to the knowledge of the author.

Firstly, none of the previous works referred in **Table 1.1.1** used H_2ZrF_6 as a precursor for the film formation. This subject should not be neglected, as this acid is the main component of the vast majority of the baths used for the production of ZrCC. Secondly, none of the mentioned reports studied the application of organic coatings on top of the Zr-based coatings produced by EAD. This is an important matter for the metal finishing industry, as ZrCC is expected to replace traditional pretreatments for painting.[28]

To finish this introduction, in the following section, the state-of-art in the development of bio-based organic coatings for the protection of metal substrates will be addressed, that is the second main objective to explore the efficiency of the ZrCC and Zr-EAD pretreatment methods.

1.2 *Epoxy coatings*

1.2.1 Synthetic epoxy resins and two-components coatings

The majority of the studies that proposed the use of Zr-based pretreatments followed by the application of an organic coating in dual or multi-layer protective systems used top coats based on epoxy resins.[55,63,85–91] This can be justified by the fact that epoxy resins can be cured to form highly cross-linked coatings with superior mechanical properties and chemical and thermal stability.[92]

The resins that have epoxide functional groups (also called oxirane groups) in their structure are called **epoxy**, therefore there is a wide variety of polymers

that are comprised under this classification. These various polymers may also contain other functional groups, as ether, ester or amine, for instance, and their chemical structures will influence the material properties. In order to obtain a finished **thermoset polymer**, the epoxy resin must undergo a cross-linking stage, which can happen in a catalytic homopolymerization process or through chemical reaction with other reagents, usually called **hardeners** (or curing agents).[92] Amines are the most used hardeners in the production of epoxy thermosets, but amides, anhydrides and polyphenols, among others, may be used as well.[93–95] Although the polymer no longer has the epoxide functional group from the original prepolymer after the curing step, it is still commonly identified as an epoxy polymer or epoxy resin.[96]

The most common mechanism for the curing of epoxy/amine systems is started by the opening of the epoxide cycle by the amine forming a hydroxyl group, in a procedure that can be carried out with or without a catalyst. This opening is shown in **Figure 1.2.1**.

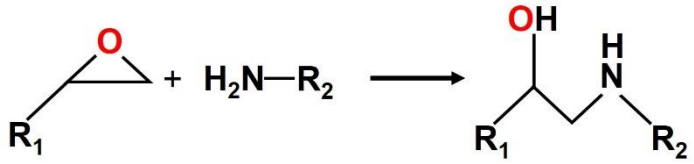

Figure 1.2.1. Oxyrane opening by the action of an amine.

The epoxide opening is activated by the formation of hydrogen bond-based complexes between the hardener and the epoxide, and it can be catalyzed by other proton donor species, therefore the generated hydroxyl may catalyze further epoxy/amine reactions. This reaction also generates an amine with one more C-N bond, transforming a primary amine into a secondary one, and a secondary into a tertiary one.

Crosslinking then takes place through the reactions of the secondary amine with an unreacted epoxy group (**Figure 1.2.2a**) or by an etherification reaction (**Figure 1.2.2b**).[97,98] This curing process may be carried out at different

temperatures, depending on the reactivity of the reagents and the desired properties.[99,100]

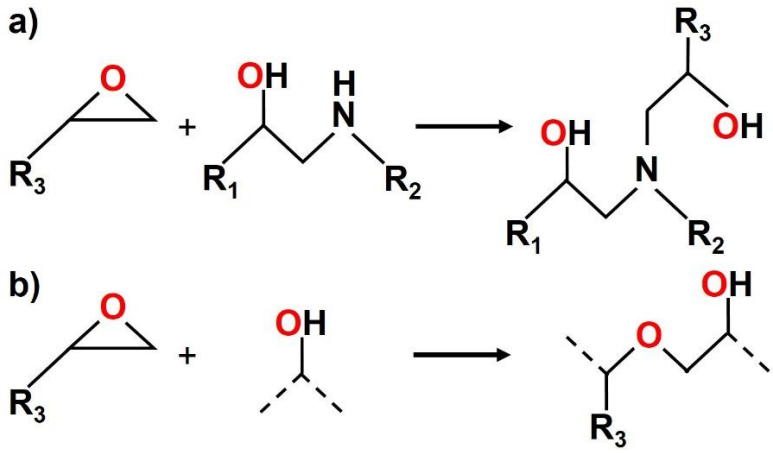

Figure 1.2.2. Crosslinking reactions of epoxy resins: **a)** addition of a secondary amine and **b)** etherification of an epoxy prepolymer by OH-epoxy reaction.

Formulations of epoxy/amine systems need to be designed considering the availability of reactive epoxy and amine groups. These systems are known as **two-components epoxy paints** (or 2K epoxy coatings, in global market). What gives the reference for calculating the proper proportions of the reagents are the **epoxy equivalent weight (EEW)** and the **amine hydrogen equivalent weight (AHEW)**. EEW indicates the mass of epoxy resins containing 1 mol of epoxy groups that it has prior to the cross-linking reactions. Therefore, a high EEW indicates a low content of epoxy groups. In a similar way, AHEW gives the mass of the amine molecule relative to the quantity of N-H groups. Therefore, different masses may be necessary to have a stoichiometric proportion of the two reagents, and these proportions can be dialed in order to obtain materials with different properties from the same set of reagents.[100]

The EEW of epoxy resins can be experimentally determined by a titration procedure using perchloric acid, described in the standard test method ASTM D1652 – 11(2019). The following equation expresses the EEW calculation:

$$EEW = \frac{100W}{AN}$$

Where W is the mass of the epoxy resin sample, in grams, A is the volume of perchloric acid used in the titration, in mL, and N is the normality of the perchloric acid solution.

The AHEW of an amine can be easily calculated if the molecular structure of the compound is known. The subsequent equation can be used:[101]

$$AHEW = \frac{M}{Number\ of\ active\ hydrogen}$$

Where M stands for the molar mass of the amine.

The presence of polar functional groups in the epoxy resin molecular structure facilitates the adsorption of epoxy polymers on metallic surfaces. These well adhered, highly cross-linked polymers with satisfactory mechanical properties provide long term corrosion protection by diminishing the electrolyte permeation to the substrate. This effect can be further improved with paint additives, which may block the electrolyte penetration or provide corrosion inhibition on the metallic surface.[92]

Most of the epoxy compositions are based on **bisphenol A diglycidyl ether (DGEBA)**, which is a product of the reaction between bisphenol A and epichlorohydrin.[92] Its molecular structure is depicted in **Figure 1.2.3**.

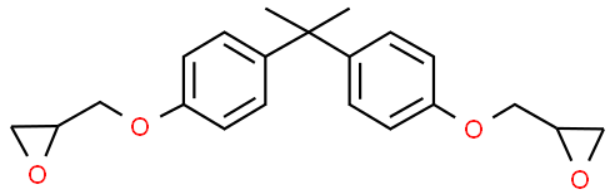

Figure 1.2.3. Molecular structure of diglycidyl ether of bisphenol A (DGEBA).[102]

The toxicity of bisphenol A has been studied, with it being classified as an endocrine disrupting chemical with mutagenic and carcinogenic effect.[103] Consequently, its use faces restrictions in many countries for applications like children's bottles and tin coating in food industry, being replaced by bisphenol S or other analogues.[94,103,104] Nevertheless, it is still allowed in coatings and adhesive fields for non-biomedical applications.

Besides the toxicity of bisphenol A, DGEBA has another reason to be replaced in the synthesis of epoxy polymers. It is a petroleum-based synthetic chemical, and both the volatility of petroleum prices and the non-renewable character of this raw material make the replacement of DGEBA a priority for the production of more environmentally friendly materials, in a market in which the coatings industry represents 50 % of the global demand.[93,94] Thus, in the next section, the state-of-art of bio-based alternatives to synthetic epoxy resins will be addressed.

1.2.2 Bio-based epoxy resins

An ideal replacement for DGEBA should, besides matching its properties and reactivity, be produced from renewable sources with economic viability. There is a wide diversity of studied candidates for replacing DGEBA, including microorganism-produced itaconic acid, sugar-derived furans and plant-based compounds, such as epoxidized vegetable oils, lignin or rosin.[105,106]

Itaconic acid, for example, is industrially produced through the fermentation of carbohydrates using *Aspergillus terreus*, a fungus, and the epoxidation of its double bonds and carboxylic acid functions provides epoxy aliphatic prepolymers. The resulting polymers may have comparable characteristics with those from DGEBA, and their properties can be tuned by copolymerization with different comonomers.[107,108]

Other interesting class of bio-based raw material is the sugar-based furans. Furans are heterocyclic compounds comprising one aromatic ring formed by one oxygen and four carbon atoms.[109] Sugar-based furans are obtained from hexose and pentose sugars. These sugars can be derived from cellulose and hemicellulose, which are currently available in industrial scale. This contributes for them to be seen as promising candidates for petroleum-based replacement in resin formulations. The epoxy resins produced with furans, because of their aromatic nature, typically have high thermal resistance and their mechanical properties are enhanced in comparison to those of aliphatic prepolymers.[96]

Among bio-based epoxies, epoxidized vegetable oils are the most investigated to supplant DGEBA resins. In epoxidized vegetable oils the epoxy group is obtained by the reaction of the double bonds of unsaturated vegetable oils, such as soybean, linseed or sunflower oils, with peracids (*i.e.*, after double-bonds oxidation).[104]

Soybean oil is widely used in the polymer industry as a plasticizer or, in its epoxidized form, as an alternative to conventional petroleum derivatives for epoxy resins. Its relatively low price and high availability provide favorable conditions for its economic viability.[96] Although, from a structural point of view, the low oxirane content of epoxidized soybean oil (ESO) may hinder the crosslinking density. This causes the polymer to have poor thermal and mechanical properties. Additionally, unreacted oil may act as a plasticizer in the resin, adding an extra factor for these polymers not being used as structural materials.[110]

In order to improve the reactivity of the prepolymer and the properties of the cured polymer, the ESO can undergo a ring-opening reaction with acrylic acid, providing acrylated ESO. This material has already been used in UV-curable organic coatings with satisfactory results.[111,112]

Linseed oil is another popular alternative because of its high double bond content, enabling the production of a highly epoxidized oil.[96] Peres *et al.*[104] have produced epoxy coatings using epoxidized linseed oil and amine curing agents. This has provided more flexible materials than the DGEBA-based ones, forming uniform films with lower water uptake than their petroleum-based counterparts.

Castor oil is obtained from the seeds of the castor plant (*Ricinus comunis*). Its main component (approximately 90 %) is ricinoleic acid. The presence of a hydroxyl group and a double carbon-carbon bond in its structure allow its chemical modification, including its epoxidation.[113] Castor oil derivatives, such as acrylated castor oil and epoxidied methacrylated castor oil, have been studied for the production of thermoset polymers with applications in composite materials and have originated materials with increased toughness in comparison to commercial epoxy thermosets.[114]

One important aspect that is common among most of these alternatives compared to DGEBA is the lower reactivity of the epoxy groups in the aliphatic monomers and the lower glass transition temperature (T_g), which is limited by the presence of long alkyl chains in the produced epoxidized vegetable oils. This may result in these polymers being unable to compete with DGEBA-based products for most applications. Given this conditions, the non-aliphatic monomers are more desirable for achieving satisfactory thermal and mechanical properties.[115,116]

Another possibility contemplated by researchers is the addition of bio-based compounds in DGEBA-based epoxy formulations, in an attempt to reduce the use of DGEBA without compromising the prepolymer reactivity. These combinations may even provide more flexibility to the typically brittle DGEBA products, which may be beneficial for some applications.[96,117]

More recently, limonene has emerged as a novel candidate for using renewable raw material for polymer production.[118] It is a cyclic monoterpene (**Figure 1.2.4**) that is abundantly found in nature and is currently extracted from citrus fruits, mainly from orange, at industrial levels.[118,119] It is the main component of orange oil, which underwent such an increase in demand that made its extraction more profitable than the orange juice production in relatively small scale production sites in the Italian region of Sicily.[119]

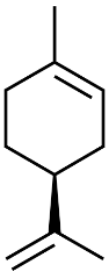

Figure 1.2.4. Molecular structure of limonene.[120]

A study on the economic viability of using limonene for replacing toxic volatile organic compounds (VOC) as solvent[121] has showed that, depending on regional and cultural factors, it could substitute toluene aromatic solvent in the cleaning sector. Some countries like Spain and Brazil, with a high production of

citrus, could make great profit of their situation to move towards greener industries. This makes limonene a chemical compound that should be of major interest in both of the countries where the research presented in this thesis has been carried out.

Limonene is reacted with perchloric acid in order to obtain limonene oxide (LO), as seen in **Figure 1.2.5**.[122,123]

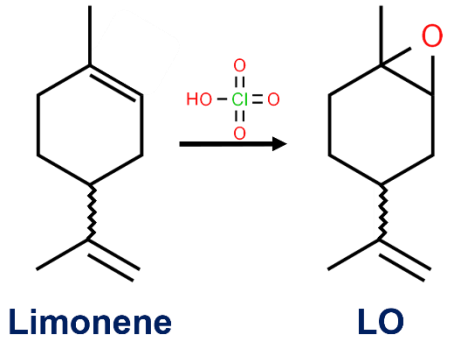

Figure 1.2.5. Schematic representation of the synthesis of limonene oxide (LO) from limonene.

This oxide is a tri-substituted epoxy that, through copolymerization with carbon dioxide and by using organic-inorganic complexes as catalysts, can be transformed into poly(limonene carbonate) (PLC), which is studied as a new bio-based prepolymer for polymer formulations.[119,122,124–126]

With the aim of obtaining a poly(limonene) dicarbonate (PLC), Kindermann, Cristòfol and Kleij have reported its synthesis starting from LO.[124] LO was transformed to PLC by copolymerization with CO_2 using a binary catalyst composed by bis-triphenylphosphine iminium chloride (PPNCl) and an aminotriphenolate Al(III) complex (Al^{Me}) in a pressurized reactor with CO_2 atmosphere. PLC went then through an oxidation with dichloromethane and meta-chloroperoxybenzoic acid, originating **poly(limonene-8,9-oxide) carbonate (PLCO)**. The synthesis sequence is depicted in **Figure 1.2.6**.

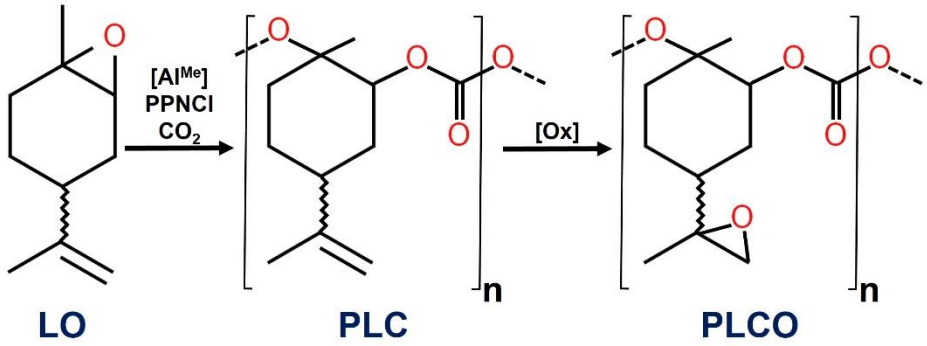

Figure 1.2.6. Schematic representation of the synthesis of PLCO as performed by Kindermann, Cristòfol and Kleij.[124]

The structure of PLCO differs from PLC because of the conversion of a terminal double bond by an epoxide function. A brief description of the two steps of synthesis was described in the paragraph above. Further details about this synthesis, such as purification procedures and reaction time and temperature, can be found in Kindermann et al. report.[124]

Although their goal was to obtain the polycarbonate PLDC, the authors went through the production of PLCO, which has a yet unexplored potential for being used for the preparation of bio-based epoxy resins, once its epoxide group may undergo the same reactions as described previously on the obtaining of synthetic epoxy thermosets (**Section 1.2.1**). This step is one of the objectives of this thesis (**Chapter 2**), since the Innovation in Materials and Molecular Engineering Biomaterials for Regenerative Therapies Group (IMEM-BRT), together with Synthetic Polymers: Structure and Properties (PSEP), both from UPC, joined their efforts to collaborate with Kleij Group and Catalyst Solutions and Optimization Laboratory (CSOL) Centre from Institut Català d'Investigació Química (ICIQ, Tarragona) in such project.

Thus, the present work was carried out with the scope of bringing together the ZrCC nanometric passivation, especially carried out with the EAD technique, and the preparation of the new epoxy thermosets from PLCO (and PLCO derivatives) with different amine hardeners. The combination of these studies can generate a new two-coat system for the protection of aluminum alloys. Therefore,

the novelty of the thesis is the combination of ZrCC pretreatment generated by EAD followed by the application of a new bio-based thermoset epoxy, as topcoat, for corrosion protection. The new materials were envisaged for coatings and adhesive technologies applications.

1.3 *References*

(1) Saevarsdottir, G.; Kvande, H.; Welch, B. J. Aluminum Production in the Times of Climate Change: The Global Challenge to Reduce the Carbon Footprint and Prevent Carbon Leakage. *JOM* **2020**, *72* (1), 296–308. https://doi.org/10.1007/s11837-019-03918-6.

(2) Scamans, G. M.; Birbilis, N.; Buchheit, R. G. Corrosion of Aluminum and Its Alloys. *Shreir's Corros.* **2010**, 1974–2010. https://doi.org/10.1016/B978-044452787-5.00095-0.

(3) Becker, M. Chromate-Free Chemical Conversion Coatings for Aluminum Alloys. *Corros. Rev.* **2019**, *37* (4), 321–342. https://doi.org/10.1515/corrrev-2019-0032.

(4) Dursun, T.; Soutis, C. Recent Developments in Advanced Aircraft Aluminium Alloys. *Mater. Des.* **2014**, *56*, 862–871. https://doi.org/10.1016/j.matdes.2013.12.002.

(5) Edwards, J. D.; Wray, R. I. Painting Aluminum. *Ind. Eng. Chem.* **1933**, *25* (1), 23–26. https://doi.org/10.1021/ie50277a006.

(6) Vargel, C. *Corrosion of Aluminium*, 1st ed.; Elsevier: Amsterdam, 2004.

(7) Ezuber, H.; El-Houd, A.; El-Shawesh, F. A Study on the Corrosion Behavior of Aluminum Alloys in Seawater. *Mater. Des.* **2008**, *29* (4), 801–805. https://doi.org/10.1016/j.matdes.2007.01.021.

(8) Sarfraz, A.; Posner, R.; Lange, M. M.; Lill, K.; Erbe, A. Role of Intermetallics and Copper in the Deposition of ZrO2 Conversion Coatings on AA6014. *J. Electrochem. Soc.* **2014**, *161* (12), C509–C516. https://doi.org/10.1149/2.0121412jes.

(9) Zhu, Y.; Sun, K.; Frankel, G. S. Intermetallic Phases in Aluminum Alloys and Their Roles in Localized Corrosion. *J. Electrochem. Soc.* **2018**, *165* (11), C807–C820. https://doi.org/10.1149/2.0931811jes.

(10) Martínez-Viademonte, M. P.; Abrahami, S. T.; Hack, T.; Burchardt, M.; Terryn, H. A Review on Anodizing of Aerospace Aluminum Alloys for Corrosion Protection. *Coatings* **2020**, *10* (11), 1–30. https://doi.org/10.3390/coatings10111106.

(11) Figueroa, R.; Nóvoa, X. R.; Pérez, C. Hydrophobic Surface Treatments for Improving the Corrosion Resistance of Anodized AA2024-T3 Alloys. *Electrochimica Acta*. 2019, pp 56–66. https://doi.org/10.1016/j.electacta.2019.02.034.

(12) Pinheiro, J. S.; Regio, G.; Cardoso, H. R. P.; Oliveira, C. T.; Ferreira, J. Z. Influence

of Concentration and PH of Hexafluorozirconic Acid on Corrosion Resistance of Anodized AA7075-T6. *Mater. Res.* **2019**, *22* (suppl 1), 1–11. https://doi.org/10.1590/1980-5373-MR-2019-0048.

(13) Hu, N.; Dong, X.; He, X.; Browning, J. F.; Schaefer, D. W. Effect of Sealing on the Morphology of Anodized Aluminum Oxide. *Corrosion Science*. 2015, pp 17–24. https://doi.org/10.1016/j.corsci.2015.03.021.

(14) Hagans, P. L.; Haas, C. M. Chromate Conversion Coatings. In *ASM Handbook: Surface Engineering*; ASM International, 1994; Vol. 5, pp 405–411. https://doi.org/10.1361/asmhba0001275.

(15) Osborne, J. H. Observations on Chromate Conversion Coatings from a Sol-Gel Perspective. *Prog. Org. Coatings* **2001**, *41* (4), 280–286. https://doi.org/10.1016/S0300-9440(01)00143-6.

(16) Lunder, O.; Walmsley, J. C.; MacK, P.; Nisancioglu, K. Formation and Characterisation of a Chromate Conversion Coating on AA6060 Aluminium. *Corros. Sci.* **2005**, *47* (7), 1604–1624. https://doi.org/10.1016/j.corsci.2004.08.012.

(17) Gharbi, O.; Thomas, S.; Smith, C.; Birbilis, N. Chromate Replacement: What Does the Future Hold? *npj Mater. Degrad.* **2018**, *2* (1), 23–25. https://doi.org/10.1038/s41529-018-0034-5.

(18) Birk, T.; Mundt, K. A.; Dell, L. D.; Luippold, R. S.; Miksche, L.; Steinmann-Steiner-Haldenstaett, W.; Mundt, D. J. Lung Cancer Mortality in the German Chromate Industry, 1958 to 1998. *J. Occup. Environ. Med.* **2006**, *48* (4), 426–433. https://doi.org/10.1097/01.jom.0000194159.88688.f8.

(19) Langard, S. One Hundred Years of Chromium and Cancer: A Review of Epidemiological Evidence and Selected Case Reports. *Am. J. Ind. Med.* **1990**, *17* (2), 189–214. https://doi.org/10.1002/ajim.4700170205.

(20) Cieślak-Golonka, M. Toxic and Mutagenic Effects of Chromium(VI). A Review. *Polyhedron* **1996**, *15* (21), 3667–3689. https://doi.org/10.1016/0277-5387(96)00141-6.

(21) Chen, Q. Y.; DesMarais, T.; Costa, M. Metals and Mechanisms of Carcinogenesis. *Annu. Rev. Pharmacol. Toxicol.* **2019**, *59*, 537–554. https://doi.org/10.1146/annurev-pharmtox-010818-021031.

(22) Prasad, S.; Yadav, K. K.; Kumar, S.; Gupta, N.; Cabral-Pinto, M. M. S.; Rezania, S.; Radwan, N.; Alam, J. Chromium Contamination and Effect on Environmental Health and Its Remediation: A Sustainable Approaches. *Journal of Environmental Management*. 2021. https://doi.org/10.1016/j.jenvman.2021.112174.

(23) Oliveira, J. C. G.; de Moraes Ferreira, R.; Stapelfeldt, D. M. A. Use of Salvinia Sp on the Adsorption of Hexavalent Chromium. *Environ. Sci. Pollut. Res.* **2019**, *26* (29), 30463–30471. https://doi.org/10.1007/s11356-019-06127-5.

(24) Kim, J. H.; Park, H. J.; Kang, J. C. Alterations in Growth Performance and Stress Responses in Juvenile Rockfish, Sebastes Schlegelii, Exposed to Dietary Chromium with Varying Levels of Dietary Ascorbic Acid Supplementation.

Chemosphere **2017**, *189*, 672–678. https://doi.org/10.1016/j.chemosphere.2017.09.071.

(25) Costa, M. Potential Hazards of Hexavalent Chromate in Our Drinking Water. *Toxicol. Appl. Pharmacol.* **2003**, *188* (1), 1–5. https://doi.org/10.1016/S0041-008X(03)00011-5.

(26) Abrahami, S. T.; de Kok, J. M. M.; Terryn, H.; Mol, J. M. C. Towards Cr(VI)-Free Anodization of Aluminum Alloys for Aerospace Adhesive Bonding Applications: A Review. *Front. Chem. Sci. Eng.* **2017**, *11* (3), 465–482. https://doi.org/10.1007/s11705-017-1641-3.

(27) Whitman, B. W.; Li, L.; Swain, G. M. Anti-Corrosion Properties of a TCP Pretreatment Conversion Coating on Aluminum Alloy 2024-T3 during Moist SO 2 Atmospheric Testing: Effects of Galvanic Coupling. *J. Electrochem. Soc.* **2017**, *164* (4), C135–C147. https://doi.org/10.1149/2.0731704jes.

(28) Milošev, I.; Frankel, G. S. Review—Conversion Coatings Based on Zirconium and/or Titanium. *J. Electrochem. Soc.* **2018**, *165* (3), C127–C144. https://doi.org/10.1149/2.0371803jes.

(29) Iribarren-Mateos, J. I.; Buj-Corral, I.; Vivancos-Calvet, J.; Alemán, C.; Iribarren, J. I.; Armelin, E. Silane and Epoxy Coatings: A Bilayer System to Protect AA2024 Alloy. *Prog. Org. Coatings* **2015**, *81*, 47–57. https://doi.org/10.1016/j.porgcoat.2014.12.014.

(30) Markley, T. A.; Mardel, J. I.; Hughes, A. E.; Hinton, B. R. W.; Glenn, A. M.; Forsyth, M. Chromate Replacement in Coatings for Corrosion Protection of Aerospace Aluminium Alloys. *Mater. Corros.* **2011**, *62* (9), 836–840. https://doi.org/10.1002/maco.200905597.

(31) Kozhukharov, S.; Girginov, C. Recent Trends of the Use of Rare Earth Elements for Efficient Environmentally Compliant Corrosion Protection of Aluminum and Its Alloys; 2020; pp 437–445. https://doi.org/10.1007/978-94-024-2018-0_35.

(32) Iannuzzi, M.; Frankel, G. S. Mechanisms of Corrosion Inhibition of AA2024-T3 by Vanadates. *Corros. Sci.* **2007**, *49* (5), 2371–2391. https://doi.org/10.1016/j.corsci.2006.10.027.

(33) Eivaz Mohammadloo, H.; Sarabi, A. A.; Asemani, H. R.; Ahmadi, P. A Comparative Study of Eco-Friendly Hybrid Thin Films: With and without Organic Coating Application. *Prog. Org. Coatings* **2018**, *125*, 432–442. https://doi.org/10.1016/j.porgcoat.2018.09.023.

(34) Kosari, A.; Visser, P.; Tichelaar, F.; Eswara, S.; Audinot, J. N.; Wirtz, T.; Zandbergen, H.; Terryn, H.; Mol, J. M. C. Cross-Sectional Characterization of the Conversion Layer Formed on AA2024-T3 by a Lithium-Leaching Coating. *Applied Surface Science*. 2020. https://doi.org/10.1016/j.apsusc.2020.145665.

(35) Buchheit, R. G.; Bode, M. D.; Stoner, G. E. Corrosion-Resistant, Chromate-Free Talc Coatings for Aluminum. *Corrosion* **1994**, *50* (3), 205–214. https://doi.org/10.5006/1.3293512.

(36) Ota, Y.; Kojima, T. Surface Treatment Technologies of Aluminum Alloy for

Automobiles. *R D Res. Dev. Kobe Steel Eng. Reports* **2017**, *66* (2), 82–85.

(37) Liu, X.; Vonk, D.; Kisslinger, K.; Tong, X.; Halada, G.; Petrash, S.; Foster, K.; Chen-Wiegart, Y. C. K. Unraveling the Formation Mechanism of a Hybrid Zr-Based Chemical Conversion Coating with Organic and Copper Compounds for Corrosion Inhibition. *ACS Appl. Mater. Interfaces* **2021**, *13* (4), 5518–5528. https://doi.org/10.1021/acsami.0c19203.

(38) Chidambaram, D.; Clayton, C. R.; Halada, G. P. The Role of Hexafluorozirconate in the Formation of Chromate Conversion Coatings on Aluminum Alloys. *Electrochim. Acta* **2006**, *51* (14), 2862–2871. https://doi.org/10.1016/j.electacta.2005.08.022.

(39) Davis, J. W. Chemical Conversion Coatings. *SAE Tech. Pap.* **1983**, 219–222. https://doi.org/10.4271/831834.

(40) Li, L.; Desouza, A. L.; Swain, G. M. In Situ PH Measurement during the Formation of Conversion Coatings on an Aluminum Alloy (AA2024). *Analyst* **2013**, *138* (15), 4398. https://doi.org/10.1039/c3an00663h.

(41) Zemanová, M.; Lokaj, J.; Karľová, M.; Madejová, J. Influence of Pre-Treatment on Zirconium Based Conversion Coating on AA2024. *Acta Chim. Slovaca* **2017**, *10* (2), 101–106. https://doi.org/10.1515/acs-2017-0018.

(42) Kuchariková, L.; Liptáková, T.; Tillová, E.; Kajánek, D.; Schmidová, E. Role of Chemical Composition in Corrosion of Aluminum Alloys. *Metals (Basel).* **2018**, *8* (8), 581. https://doi.org/10.3390/met8080581.

(43) Lunder, O.; Simensen, C.; Yu, Y.; Nisancioglu, K. Formation and Characterisation of Ti–Zr Based Conversion Layers on AA6060 Aluminium. *Surf. Coatings Technol.* **2004**, *184* (2–3), 278–290. https://doi.org/10.1016/j.surfcoat.2003.11.003.

(44) Nordlien, J. H.; Walmsley, J. C.; Østerberg, H.; Nisancioglu, K. Formation of a Zirconium-Titanium Based Conversion Layer on AA 6060 Aluminium. *Surf. Coatings Technol.* **2002**, *153* (1), 72–78. https://doi.org/10.1016/S0257-8972(01)01663-2.

(45) Cardoso, H. R. P.; Rapacki, C.; Ferreira, J. Z. Monitoring of a Zr-Based Conversion Coating on Galvanised Steel and Its Performance against Corrosion. *Corros. Eng. Sci. Technol.* **2019**, *54* (8), 726–730. https://doi.org/10.1080/1478422X.2019.1657703.

(46) Verdier, S.; van der Laak, N.; Dalard, F.; Metson, J.; Delalande, S. An Electrochemical and SEM Study of the Mechanism of Formation, Morphology, and Composition of Titanium or Zirconium Fluoride-Based Coatings. *Surf. Coatings Technol.* **2006**, *200* (9), 2955–2964. https://doi.org/10.1016/j.surfcoat.2004.10.139.

(47) Verdier, S.; Delalande, S.; van der Laak, N.; Metson, J.; Dalard, F. Monochromatized X-Ray Photoelectron Spectroscopy of the AM60 Magnesium Alloy Surface after Treatments in Fluoride-Based Ti and Zr Solutions. *Surf. Interface Anal.* **2005**, *37* (5), 509–516. https://doi.org/10.1002/sia.2042.

(48) Moreira, V. B.; Puiggalí-Jou, A.; Jiménez-Piqué, E.; Alemán, C.; Meneguzzi, A.; Armelin, E. Green Nanocoatings Based on the Deposition of Zirconium Oxide: The Role of the Substrate. *Materials (Basel).* **2021**, *14* (4), 1–18. https://doi.org/10.3390/ma14041043.

(49) Taheri, P.; Lill, K.; de Wit, J. H. W.; Mol, J. M. C.; Terryn, H. Effects of Zinc Surface Acid-Based Properties on Formation Mechanisms and Interfacial Bonding Properties of Zirconium-Based Conversion Layers. *J. Phys. Chem. C* **2012**, *116* (15), 8426–8436. https://doi.org/10.1021/jp209422d.

(50) Cerezo, J.; Vandendael, I.; Posner, R.; de Wit, J. H. W.; Mol, J. M. C.; Terryn, H. The Effect of Surface Pre-Conditioning Treatments on the Local Composition of Zr-Based Conversion Coatings Formed on Aluminium Alloys. *Appl. Surf. Sci.* **2016**, *366*, 339–347. https://doi.org/10.1016/j.apsusc.2016.01.106.

(51) Šekularac, G.; Kovač, J.; Milošev, I. Prolonged Protection, by Zirconium Conversion Coatings, of AlSi7Mg0.3 Aluminium Alloy in Chloride Solution. *Corrosion Science*. 2020. https://doi.org/10.1016/j.corsci.2020.108615.

(52) Andreatta, F.; Paussa, L.; Lanzutti, A.; Rosero Navarro, N. C.; Aparicio, M.; Castro, Y.; Duran, A.; Ondratschek, D.; Fedrizzi, L. Development and Industrial Scale-up of ZrO2 Coatings and Hybrid Organic–Inorganic Coatings Used as Pre-Treatments before Painting Aluminium Alloys. *Prog. Org. Coatings* **2011**, *72* (1–2), 3–14. https://doi.org/10.1016/j.porgcoat.2011.01.011.

(53) Zhou, P.; Liu, Y.; Liu, L.; Yu, B.; Zhang, T.; Wang, F. Critical Role of Pretreatment on the Corrosion Resistance of Zr Conversion Coating on 6061 Aluminum Alloy: The Combined Effect of Surface Topography and Potential Difference between Different Phases. *Surf. Coatings Technol.* **2019**, *377* (July). https://doi.org/10.1016/j.surfcoat.2019.124904.

(54) Shruthi, T. K.; Swain, G. M. Communication—Role of Trivalent Chromium on the Anti-Corrosion Properties of a TCP Conversion Coating on Aluminum Alloy 2024-T3. *J. Electrochem. Soc.* **2018**, *165* (2), C103–C105. https://doi.org/10.1149/2.1301802jes.

(55) Andreatta, F.; Paussa, L.; Aldighieri, P.; Lanzutti, A.; Raps, D.; Fedrizzi, L. Corrosion Behaviour of Sol–Gel Treated and Painted AA2024 Aluminium Alloy. *Prog. Org. Coatings* **2010**, *69* (2), 133–142. https://doi.org/10.1016/j.porgcoat.2010.04.012.

(56) Šekularac, G.; Milošev, I. Electrochemical Behavior and Self-Sealing Ability of Zirconium Conversion Coating Applied on Aluminum Alloy 3005 in 0.5 M NaCl Solution. *J. Electrochem. Soc.* **2020**, *167* (2), 021509. https://doi.org/10.1149/1945-7111/ab6b0d.

(57) van Dam, J. P. B.; Abrahami, S. T.; Yilmaz, A.; Gonzalez-Garcia, Y.; Terryn, H.; Mol, J. M. C. Effect of Surface Roughness and Chemistry on the Adhesion and Durability of a Steel-Epoxy Adhesive Interface. *Int. J. Adhes. Adhes.* **2020**, *96* (October), 102450. https://doi.org/10.1016/j.ijadhadh.2019.102450.

(58) Fockaert, L. I.; Taheri, P.; Abrahami, S. T.; Boelen, B.; Terryn, H.; Mol, J. M. C. Zirconium-Based Conversion Film Formation on Zinc, Aluminium and

Magnesium Oxides and Their Interactions with Functionalized Molecules. *Appl. Surf. Sci.* **2017**, *423*, 817–828. https://doi.org/10.1016/j.apsusc.2017.06.174.

(59) Fockaert, L. I.; Pletincx, S.; Ganzinga-Jurg, D.; Boelen, B.; Hauffman, T.; Terryn, H.; Mol, J. M. C. Chemisorption of Polyester Coatings on Zirconium-Based Conversion Coated Multi-Metal Substrates and Their Stability in Aqueous Environment. *Applied Surface Science*. 2020. https://doi.org/10.1016/j.apsusc.2019.144771.

(60) Fockaert, L. I.; Ankora, M. V. E.; Van Dam, J. P. B.; Pletincx, S.; Yilmaz, A.; Boelen, B.; Hauffman, T.; Garcia-Gonzalez, Y.; Terryn, H.; Mol, J. M. C. Effect of Organic Additives in Fluoacid-Based Ti and Zr-Treatments for Galvanized Steel on the Stability of a Polymer Coated Interface. *Progress in Organic Coatings*. 2020. https://doi.org/10.1016/j.porgcoat.2020.105738.

(61) Ghanbari, A.; Attar, M. M. Surface Free Energy Characterization and Adhesion Performance of Mild Steel Treated Based on Zirconium Conversion Coating: A Comparative Study. *Surf. Coatings Technol.* **2014**, *246*, 26–33. https://doi.org/10.1016/j.surfcoat.2014.02.057.

(62) Eivaz Mohammadloo, H.; Sarabi, A. A.; Sabbagh Alvani, A. A.; Sameie, H.; Salimi, R. Nano-Ceramic Hexafluorozirconic Acid Based Conversion Thin Film: Surface Characterization and Electrochemical Study. *Surf. Coatings Technol.* **2012**, *206* (19–20), 4132–4139. https://doi.org/10.1016/j.surfcoat.2012.04.009.

(63) Eivaz Mohammadloo, H.; Sarabi, A. A.; Mohammad Hosseini, R.; Sarayloo, M.; Sameie, H.; Salimi, R. A Comprehensive Study of the Green Hexafluorozirconic Acid-Based Conversion Coating. *Prog. Org. Coatings* **2014**, *77* (2), 322–330. https://doi.org/10.1016/j.porgcoat.2013.10.006.

(64) Liu, X.; Vonk, D.; Jiang, H.; Kisslinger, K.; Tong, X.; Ge, M.; Nazaretski, E.; Ravel, B.; Foster, K.; Petrash, S.; et al. Environmentally Friendly Zr-Based Conversion Nanocoatings for Corrosion Inhibition of Metal Surfaces Evaluated by Multimodal X-Ray Analysis. *ACS Appl. Nano Mater.* **2019**, *2* (4), 1920–1929. https://doi.org/10.1021/acsanm.8b02309.

(65) Cardoso, H. R. P. Obtenção de Revestimento de Conversão Hidrofóbico à Base de Zircônio e Ácido Carboxílico Sobre Aço Galvanizado, Universidade Federal do Rio Grande do Sul, 2019.

(66) Schoukens, I.; Vandendael, I.; De Strycker, J.; Saleh, A. A.; Terryn, H.; De Graeve, I. Effect of Surface Composition and Microstructure of Aluminised Steel on the Formation of a Titanium-Based Conversion Layer. *Surf. Coatings Technol.* **2013**, *235*, 628–636. https://doi.org/10.1016/j.surfcoat.2013.08.041.

(67) Treptow, R. S. Le Chatelier's Principle: A Reexamination and Method of Graphic Illustration. *J. Chem. Educ.* **1980**, *57* (6), 417–420. https://doi.org/10.1021/ed057p417.

(68) Dong, X.; Argekar, S.; Wang, P.; Schaefer, D. W. In Situ Evolution of Trivalent Chromium Process Passive Film on Al in a Corrosive Aqueous Environment. *ACS Appl. Mater. Interfaces* **2011**, *3* (11), 4206–4214. https://doi.org/sw.

(69) Shacham, R.; Mandler, D.; Avnir, D. Electrochemically Induced Sol–Gel Deposition of Zirconia Thin Films. *Chem. - A Eur. J.* **2004**, *10* (8), 1936–1943. https://doi.org/10.1002/chem.200305469.

(70) Gal-Or, L.; Silberman, I.; Chaim, R. Electrolytic Zr02: I. Electrochemical Aspects. *J. Electrochem. Soc.* **1991**, *138* (7).

(71) Shacham, R.; Avnir, D.; Mandler, D.; others. Electrodeposition of Methylated Sol-Gel Films on Conducting Surfaces. *Adv. Mater.* **1999**, *11* (5), 384–388.

(72) Zhitomirsky, I.; Petric, A. Electrolytic Deposition of Zirconia and Zirconia Organoceramic Composites. *Mater. Lett.* **2000**, *46* (1), 1–6. https://doi.org/10.1016/S0167-577X(00)00133-6.

(73) Liu, L.; Mandler, D. Electrochemical Deposition of Sol-Gel Films. In *Handbook of Sol-Gel Science and Technology*; Springer International Publishing: Cham, 2018; pp 531–568. https://doi.org/10.1007/978-3-319-32101-1_113.

(74) Hsu, H. C.; Yen, S. K. Evaluation of Metal Ion Release and Corrosion Resistance of ZrO2 Thin Coatings on the Dental Co–Cr Alloys. *Dent. Mater.* **1998**, *14* (5), 339–346. https://doi.org/10.1016/S0109-5641(99)00002-0.

(75) Gal-Or, L.; Silberman, I.; Chaim, R. Electrolytic ZrO2 Coatings: I. Electrochemical Aspects. *J. Electrochem. Soc.* **1991**, *138* (7), 1939–1942. https://doi.org/10.1149/1.2085904.

(76) Chaim, R.; Silberman, I.; Gal-Or, L. Electrolytic Zr02 Coatings: II. Microstructural Aspects. *J. Electrochem. Soc.* **1991**, *138* (7), 5.

(77) Yen, S. K. Characterization of Electrolytic ZrO2 Coating on AISI 316L Stainless Steel. *J. Electrochem. Soc.* **1999**, 5.

(78) Yen, S.-K. Mechanism of Electrolytic ZrO2 Coating on Commercial Pure Titanium. *Mater. Chem. Phys.* **2000**, *63* (3), 256–262. https://doi.org/10.1016/S0254-0584(99)00232-1.

(79) Yen, S. .; Guo, M. .; Zan, H. . Characterization of Electrolytic ZrO2 Coating on Co–Cr–Mo Implant Alloys of Hip Prosthesis. *Biomaterials* **2001**, *22* (2), 125–133. https://doi.org/10.1016/S0142-9612(00)00133-2.

(80) Maji, P.; Nath, R. K.; Karmakar, R.; Paul, P.; Meitei, R. K. B.; Ghosh, S. K. Effect of Post Processing Heat Treatment on Friction Stir Welded/Processed Aluminum Based Alloys and Composites. *CIRP J. Manuf. Sci. Technol.* **2021**, *35*, 96–105. https://doi.org/10.1016/j.cirpj.2021.05.014.

(81) Alexopoulos, N. D.; Velonaki, Z.; Stergiou, C. I.; Kourkoulis, S. K. The Effect of Artificial Ageing Heat Treatments on the Corrosion-Induced Hydrogen Embrittlement of 2024 (Al-Cu) Aluminium Alloy. *Corros. Sci.* **2016**, *102*, 413–424. https://doi.org/10.1016/j.corsci.2015.10.034.

(82) Giacomelli, F. C.; Giacomelli, C.; De Oliveira, A. G.; Spinelli, A. Effect of Electrolytic ZrO2 Coatings on the Breakdown Potential of NiTi Wires Used as Endovascular Implants. *Mater. Lett.* **2005**, *59* (7), 754–758. https://doi.org/10.1016/j.matlet.2004.11.015.

(83) Dong, X.; Wang, P.; Argekar, S.; Schaefer, D. W. Structure and Composition of Trivalent Chromium Process (TCP) Films on Al Alloy. *Langmuir* **2010**, *26* (13), 10833–10841. https://doi.org/10.1021/la100699u.

(84) Qi, J.; Światowska, J.; Skeldon, P.; Marcus, P. Chromium Valence Change in Trivalent Chromium Conversion Coatings on Aluminium Deposited under Applied Potentials. *Corros. Sci.* **2020**, *167* (December 2019). https://doi.org/10.1016/j.corsci.2020.108482.

(85) Sharifi Golru, S.; Attar, M. M.; Ramezanzadeh, B. Effects of Surface Treatment of Aluminium Alloy 1050 on the Adhesion and Anticorrosion Properties of the Epoxy Coating. *Appl. Surf. Sci.* **2015**, *345*, 360–368. https://doi.org/10.1016/j.apsusc.2015.03.148.

(86) Niknahad, M.; Moradian, S.; Mirabedini, S. M. The Adhesion Properties and Corrosion Performance of Differently Pretreated Epoxy Coatings on an Aluminium Alloy. *Corros. Sci.* **2010**, *52* (6), 1948–1957. https://doi.org/10.1016/j.corsci.2010.02.014.

(87) Asemani, H. R.; Ahmadi, P.; Sarabi, A. A.; Eivaz Mohammadloo, H. Effect of Zirconium Conversion Coating: Adhesion and Anti-Corrosion Properties of Epoxy Organic Coating Containing Zinc Aluminum Polyphosphate (ZAPP) Pigment on Carbon Mild Steel. *Prog. Org. Coatings* **2016**, *94*, 18–27. https://doi.org/10.1016/j.porgcoat.2016.01.015.

(88) Sababi, M.; Terryn, H.; Mol, J. M. C. The Influence of a Zr-Based Conversion Treatment on Interfacial Bonding Strength and Stability of Epoxy Coated Carbon Steel. *Prog. Org. Coatings* **2017**, *105*, 29–36. https://doi.org/10.1016/j.porgcoat.2016.11.016.

(89) Ramanathan, E.; Balasubramanian, S. Comparative Study on Polyester Epoxy Powder Coat and Amide Cured Epoxy Liquid Paint over Nano-Zirconia Treated Mild Steel. *Prog. Org. Coatings* **2016**, *93*, 68–76. https://doi.org/10.1016/j.porgcoat.2016.01.007.

(90) Ghanbari, A.; Attar, M. M. The Effect of Zirconium-Based Surface Treatment on the Cathodic Disbonding Resistance of Epoxy Coated Mild Steel. *Appl. Surf. Sci.* **2014**, *316*, 429–434. https://doi.org/10.1016/j.apsusc.2014.07.178.

(91) Liu, Y.; Yang, Y.; Zhang, C.; Zhang, T.; Yu, B.; Meng, G.; Shao, Y.; Wang, F.; Liu, L. Protection of AA5083 by a Zirconium-Based Conversion Coating. *J. Electrochem. Soc.* **2016**, *163* (9), C576–C586. https://doi.org/10.1149/2.1021609jes.

(92) Verma, C.; Olasunkanmi, L. O.; Akpan, E. D.; Quraishi, M. A.; Dagdag, O.; El Gouri, M.; Sherif, E. S. M.; Ebenso, E. E. Epoxy Resins as Anticorrosive Polymeric Materials: A Review. *React. Funct. Polym.* **2020**, *156* (June), 104741. https://doi.org/10.1016/j.reactfunctpolym.2020.104741.

(93) Mashouf Roudsari, G.; Mohanty, A. K.; Misra, M. Green Approaches to Engineer Tough Biobased Epoxies: A Review. *ACS Sustain. Chem. Eng.* **2017**, *5* (11), 9528–9541. https://doi.org/10.1021/acssuschemeng.7b01422.

(94) Baroncini, E. A.; Kumar Yadav, S.; Palmese, G. R.; Stanzione, J. F. Recent

Advances in Bio-Based Epoxy Resins and Bio-Based Epoxy Curing Agents. *J. Appl. Polym. Sci.* **2016**, *133* (45). https://doi.org/10.1002/app.44103.

(95) Tcharkhtchi, A.; Nony, F.; Khelladi, S.; Fitoussi, J.; Farzaneh, S. *Epoxy/Amine Reactive Systems for Composites Materials and Their Thermomechanical Properties*; Elsevier Ltd., 2015; Vol. 1. https://doi.org/10.1016/B978-1-78242-307-2.00013-0.

(96) Gonçalves, F. A. M. M.; Santos, M.; Cernadas, T.; Ferreira, P.; Alves, P. Advances in the Development of Biobased Epoxy Resins: Insight into More Sustainable Materials and Future Applications. *Int. Mater. Rev.* **2021**, *0* (0), 1–31. https://doi.org/10.1080/09506608.2021.1915936.

(97) Ellis, B. *Chemistry and Technology of Epoxy Resins*, 1st ed.; Ellis, B., Ed.; Springer Netherlands: Dordrecht, 1993. https://doi.org/10.1007/978-94-011-2932-9.

(98) Vyazovkin, S.; Sbirrazzuoli, N. Mechanism and Kinetics of Epoxy-Amine Cure Studied by Differential Scanning Calorimetry. *Macromolecules* **1996**, *29* (6), 1867–1873. https://doi.org/10.1021/ma951162w.

(99) Carbas, R. J. C.; Marques, E. A. S.; Da Silva, L. F. M.; Lopes, A. M. Effect of Cure Temperature on the Glass Transition Temperature and Mechanical Properties of Epoxy Adhesives. *J. Adhes.* **2014**, *90* (1), 104–119. https://doi.org/10.1080/00218464.2013.779559.

(100) Pham, H. Q.; Marks, M. J. Epoxy Resins. In *Ullmann's Encyclopedia of Industrial Chemistry*; Wiley-VCH Verlag GmbH & Co. KGaA: Weinheim, Germany, 2005. https://doi.org/10.1002/14356007.a09_547.pub2.

(101) Cornille, A.; Serres, J.; Michaud, G.; Simon, F.; Fouquay, S.; Boutevin, B.; Caillol, S. Syntheses of Epoxyurethane Polymers from Isocyanate Free Oligo-Polyhydroxyurethane. *Eur. Polym. J.* **2016**, *75*, 175–189. https://doi.org/10.1016/j.eurpolymj.2015.12.017.

(102) Royal Society of Chemistry. Chemspider - search and share chemistry http://www.chemspider.com/Chemical-Structure.2199.html (accessed Sep 3, 2021).

(103) Michałowicz, J. Bisphenol A - Sources, Toxicity and Biotransformation. *Environ. Toxicol. Pharmacol.* **2014**, *37* (2), 738–758. https://doi.org/10.1016/j.etap.2014.02.003.

(104) Peres, R. S.; Ferreira, C. A.; Alemán, C.; Armelin, E. Development of Novel Biobased Epoxy Films with Aliphatic and Aromatic Amine Hardeners for the Partial Replacement of Bisphenol A in Primer Coatings. In *Biobased and environmentally benign coatings*; Tiwari, A., Galanis, A., Soucek, M. D., Eds.; Scrivener Publishing LLC, 2016; pp 121–148.

(105) Kumar, S.; Samal, S. K.; Mohanty, S.; Nayak, S. K. Recent Development of Biobased Epoxy Resins: A Review. *Polym. Plast. Technol. Eng.* **2018**, *57* (3), 133–155. https://doi.org/10.1080/03602559.2016.1253742.

(106) Gandini, A.; Lacerda, T. M.; Carvalho, A. J. F.; Trovatti, E. Progress of Polymers from Renewable Resources: Furans, Vegetable Oils, and Polysaccharides. *Chem. Rev.* **2016**, *116* (3), 1637–1669. https://doi.org/10.1021/acs.chemrev.5b00264.

(107) Kumar, S.; Samal, S. K.; Mohanty, S.; Nayak, S. K. Synthesis and Characterization of Itaconic-Based Epoxy Resins. *Polym. Adv. Technol.* **2018**, *29* (1), 160–170. https://doi.org/10.1002/pat.4098.

(108) Ma, S.; Liu, X.; Jiang, Y.; Tang, Z.; Zhang, C.; Zhu, J. Bio-Based Epoxy Resin from Itaconic Acid and Its Thermosets Cured with Anhydride and Comonomers. *Green Chem.* **2013**, *15* (1), 245–254. https://doi.org/10.1039/c2gc36715g.

(109) Izzotti, A.; Pulliero, A. The Effects of Environmental Chemical Carcinogens on the MicroRNA Machinery. *Int. J. Hyg. Environ. Health* **2014**, *217* (6), 601–627. https://doi.org/10.1016/j.ijheh.2014.01.001.

(110) Wang, R.; Schuman, T. P. Vegetable Oil-Derived Epoxy Monomers and Polymer Blends: A Comparative Study with Review. *Express Polym. Lett.* **2012**, *7* (3), 272–292. https://doi.org/10.3144/expresspolymlett.2013.25.

(111) Wu, Q.; Hu, Y.; Tang, J.; Zhang, J.; Wang, C.; Shang, Q.; Feng, G.; Liu, C.; Zhou, Y.; Lei, W. High-Performance Soybean-Oil-Based Epoxy Acrylate Resins: "Green" Synthesis and Application in UV-Curable Coatings. *ACS Sustain. Chem. Eng.* **2018**, *6* (7), 8340–8349. https://doi.org/10.1021/acssuschemeng.8b00388.

(112) Li, X.; Wang, D.; Zhao, L.; Hou, X.; Liu, L.; Feng, B.; Li, M.; Zheng, P.; Zhao, X.; Wei, S. UV LED Curable Epoxy Soybean-Oil-Based Waterborne PUA Resin for Wood Coatings. *Prog. Org. Coatings* **2021**, *151*, 105942. https://doi.org/10.1016/j.porgcoat.2020.105942.

(113) Chauke, N. P.; Mukaya, H. E.; Nkazi, D. B. Chemical Modifications of Castor Oil: A Review. *Sci. Prog.* **2019**, *102* (3), 199–217. https://doi.org/10.1177/0036850419859118.

(114) Nekhavhambe, E.; Mukaya, H. E.; Nkazi, D. B. Development of Castor Oil–Based Polymers: A Review. *J. Adv. Manuf. Process.* **2019**, *1* (4), 1–13. https://doi.org/10.1002/amp2.10030.

(115) Ng, F.; Couture, G.; Philippe, C.; Boutevin, B.; Caillol, S. Bio-Based Aromatic Epoxy Monomers for Thermoset Materials. *Molecules* **2017**, *22* (1). https://doi.org/10.3390/molecules22010149.

(116) Savonnet, E.; Grau, E.; Grelier, S.; Defoort, B.; Cramail, H. Divanillin-Based Epoxy Precursors as DGEBA Substitutes for Biobased Epoxy Thermosets. *ACS Sustain. Chem. Eng.* **2018**, *6* (8), 11008–11017. https://doi.org/10.1021/ACSSUSCHEMENG.8B02419.

(117) Kumar, S.; Krishnan, S.; K. Samal, S.; Mohanty, S.; K. Nayak, S. Toughening of Petroleum Based (DGEBA) Epoxy Resins with Various Renewable Resources Based Flexible Chains for High Performance Applications: A Review. *Ind. Eng. Chem. Res.* **2018**, *57* (8), 2711–2726. https://doi.org/10.1021/acs.iecr.7b04495.

(118) Ciriminna, R.; Lomeli-Rodriguez, M.; Demma Carà, P.; Lopez-Sanchez, J. A.; Pagliaro, M. Limonene: A Versatile Chemical of the Bioeconomy. *Chem. Commun.* **2014**, *50* (97), 15288–15296. https://doi.org/10.1039/c4cc06147k.

(119) Parrino, F.; Fidalgo, A.; Palmisano, L.; Ilharco, L. M.; Pagliaro, M.; Ciriminna, R. Polymers of Limonene Oxide and Carbon Dioxide: Polycarbonates of the Solar

Economy. *ACS Omega* **2018**, *3* (5), 4884–4890. https://doi.org/10.1021/acsomega.8b00644.

(120) Royal Society of Chemistry. Chemspider - search and share chemistry http://www.chemspider.com/Chemical-Structure.388386.html (accessed Sep 3, 2021).

(121) Paggiola, G.; Stempvoort, S. Van; Bustamante, J.; Barbero, J. M. V.; Hunt, A. J.; Clark, J. H. Can Bio-Based Chemicals Meet Demand? Global and Regional Case-Study around Citrus Waste-Derived Limonene as a Solvent for Cleaning Applications. *Biofuels, Bioprod. Biorefining* **2016**, *10* (6), 686–698. https://doi.org/10.1002/bbb.1677.

(122) Ciriminna, R.; Parrino, F.; De Pasquale, C.; Palmisano, L.; Pagliaro, M. Photocatalytic Partial Oxidation of Limonene to 1,2 Limonene Oxide. *Chem. Commun.* **2018**, *54* (8), 1008–1011. https://doi.org/10.1039/c7cc09788c.

(123) Couture, G.; Granado, L.; Fanget, F.; Boutevin, B.; Caillol, S. Limonene-Based Epoxy: Anhydride Thermoset Reaction Study. *Molecules* **2018**, *23* (11). https://doi.org/10.3390/molecules23112739.

(124) Kindermann, N.; Cristòfol, À.; Kleij, A. W. Access to Biorenewable Polycarbonates with Unusual Glass-Transition Temperature (Tg) Modulation. *ACS Catal.* **2017**, *7* (6), 3860–3863. https://doi.org/10.1021/acscatal.7b00770.

(125) Stößer, T.; Li, C.; Unruangsri, J.; Saini, P. K.; Sablong, R. J.; Meier, M. A. R.; Williams, C. K.; Koning, C. Bio-Derived Polymers for Coating Applications: Comparing Poly(Limonene Carbonate) and Poly(Cyclohexadiene Carbonate). *Polym. Chem.* **2017**, *8* (39), 6099–6105. https://doi.org/10.1039/c7py01223c.

(126) Hauenstein, O.; Reiter, M.; Agarwal, S.; Rieger, B.; Greiner, A. Bio-Based Polycarbonate from Limonene Oxide and CO2 with High Molecular Weight, Excellent Thermal Resistance, Hardness and Transparency. *Green Chem.* **2016**, *18* (3), 760–770. https://doi.org/10.1039/c5gc01694k.

(127) Ramakrishna, S.; Tian, L.; Wang, C.; Liao, S.; Teo, W. E. Safety Testing of a New Medical Device. *Med. Devices* **2015**, 137–153. https://doi.org/10.1016/b978-0-08-100289-6.00006-5.

(128) Maurici, D.; Aardema, M.; Corvi, R.; Kleber, M.; Krul, C.; Laurent, C.; Loprieno, N.; Pasanen, M.; Pfuhler, S.; Phillips, B.; et al. Genotoxicity and Mutagenicity. *Altern. to Lab. Anim.* **2005**, *33* (1_suppl), 117–130. https://doi.org/10.1177/026119290503301s13.

(129) Ardon, M. Olation and Structure. *Comments Inorg. Chem.* **1989**, *8* (5), 221–232. https://doi.org/10.1080/02603598908035796.

(130) Brinker, C. J.; Scherer, G. W. *Sol-Gel Science: The Physics and Chemistry of Sol-Gel Processing*; Elsevier, 1990. https://doi.org/10.1016/C2009-0-22386-5.

2. Objectives

2 Objectives

This research was carried out in a collaboration between IMEM-BRT – Innovation in Materials and Molecular Engineering - Biomaterials for Regenerative Therapies, at Universitat Politècnica de Catalunya (UPC), and LACOR – Laboratório de Corrosão, Proteção e Reciclagem de Materiais, at Universidade Federal do Rio Grande do Sul (UFRGS). Parts of this work also had the valuable cooperation of the Institut Català d'Investigació Química (ICIQ) and the Synthetic Polymers: Structure and Properties Group (PSEP), at UPC.

The first stage of this research comprises the objective of producing ZrCC on aluminum alloy substrates using the EAD technique and comparison of this method with the dip-coating process, the classical one. The specific objectives at this stage are:

a) Identify the influence of the aluminum substrate in the deposition process of ZrCC while using the EAD technique;
b) Determine the chemical composition of the ZrCC films produced by EAD on aluminum;
c) Produce thicker and more homogeneous ZrCC films in order to provide low film porosity and enhanced corrosion protection for aluminum;
d) Evaluate the corrosion protection provided by a bilayer coating system with EAD-produced ZrCC and a commercial organic coating.

The second stage of this research has the objective of producing a partially bio-based epoxy thermoset polymer with the PLCO fully bio-based prepolymer, prepared at ICIQ and, in cooperation with PSEP, measure its thermal and mechanical properties. More specifically:

a) Identify, within the commonly used solvents in the coatings industry, the adequate solvents for PLCO solid epoxy resin;
b) Find compatible commercially available amine hardeners for the preparation of a two-component thermoset epoxy with PLCO;
c) Establish a curing procedure of the studied PLCO-amine systems;

d) Study, through thermal characterization techniques, the relative reactivity of the two-component systems, the T_g of the polymers and their thermal stability;

e) Determine the mechanical properties of the studied thermoset polymers.

In the final part of this research, the combination of the findings of the two previous stages will be used with the objective of producing the optimum bilayer coating system for aluminum alloy protection, with an EAD-made ZrCC followed by the application of PLCO bio-based derivative that obtained the best thermal and mechanical properties. The specific objectives of this part comprise:

a) Provide corrosion protection to aluminum with the studied coating system;

b) Evaluate the adherence between the two layers of the coating system.

3 Green nanocoatings based on the deposition of zirconium oxide: The role of the substrate

SUMMARY

Herein, the influence of the substrate in the formation of zirconium oxide monolayer, from an aqueous hexafluorozirconic acid solution, by chemical conversion and by electro-assisted deposition, has been approached. The nanoscale dimensions of the ZrO_2 film is affected by the substrate nature and roughness. This study evidenced that the mechanism of Zr-EAD is dependent on the potential applied and on the substrate composition, whereas conversion coating is uniquely dependent on the adsorption reaction time. The zirconium oxide based nanofilms were more homogenous in AA2024 substrates if compared to pure Al grade (AA1100). It was justified by the high content of Cu alloying element present in the grain boundaries of the latter. Such intermetallic active sites favor the obtaining of ZrO_2 films, as demonstrated by XPS and AFM results. From a mechanistic point of view, the electrochemical reactions take place simultaneously with the conventional chemical conversion process driven by ions diffusion. Such findings will bring new perspectives for the generation of controlled oxide coatings in modified electrodes used, as for example, in the construction of battery cells; in automotive and in aerospace industries, to replace micrometric layers of zinc phosphate by light-weight zirconium oxide nanometric ones. This study is particularly addressed for the reduction of industrial waste by applying green bath solutions without the need of auxiliary compounds and using lightweight ceramic materials.

Publication derived from this work:

Moreira, V. B.; Puiggalí-Jou, A.; Jiménez-Piqué, E.; Alemán, C.; Meneguzzi, A.; and Armelin, E. Green Nanocoatings Based on the Deposition of Zirconium Oxide: The Role of the Substrate. *Materials* **2021**, 14, 1043. https://doi.org/10.3390/ma14041043

3.1 *Introduction*

Circular economy, life-cycle assessment, reduction of fuel consumption, reduction of industry manufacturing costs, all together drive forces to the development of environmentally friendly and lightweight new materials and devices for automotive and aerospace industry applications. Within this context, old and expensive metal pre-treatment processes, such as iron and tri-cation zinc phosphate, and green and yellow chromate, are moving towards a new generation of cleaning and surface activation processes.[1,2] Phosphating is a widely used chemical pre-treatment process for metal surface protection, actuating as both passivation layer and adhesion promoter for subsequent application of organic coatings, particularly in the automotive and in the aircraft industry.[3,4] Phosphate and chromate technologies have been substituted by chromium-free and hybrid pre-treatment coatings.[5–7] The urge for innovation in such processes and, particularly, in the replacement of hazardous substances (with potential toxicity for human life) motivate extensive research on various alternatives, among which titanium and zirconium fluorinated-complexes are recognized as one of the most promising pre-treatment coatings for body car protection, aerospace alloys, coil coatings, and other structural equipment.[8,9]

Zirconium-based conversion coating (ZrCC) has been widely used as chemical pre-treatment by dip-coating deposition and under cathodic electro-dip primer formation, mainly for the replacement of tri-cation zinc phosphate pre-treatments in the automotive original equipment manufacturers (OEM) market.[10] Such coatings, with specific weight of only 0.01 to 0.02 g/m^2, are extremely thin and represent a great advantage of cost and light-weighting final material for the producers.[1] The effectiveness of the dip-coating process by immersion of the metal substrate in hexafluorozirconic-acid-based (H_2ZrF_6-based) solution is pH limited and the homogeneity of the obtained films is sometimes poor.[11]

Previous works have demonstrated that the incorporation of auxiliary additives in the bath solutions, like copper (II), nickel (II), nitrate (NO_3^-) and hydrogen phosphate (HPO_4^{2-}) ions, are necessary to further improve the barrier property and the density of ZrCC layer.[12,13] Unfortunately, the addition of auxiliary compounds is not a good option for industrial applications because they may increase the formation of anodic sludge in tanks and the amount of water contaminants, resulting in non-sustainable and non-competitive costs for industry.

There are a lot of examples of the ZrCC applications in steel and aluminum alloys, by dip-coating method[8,14–16] and a few related to the electro-assisted deposition (EAD) method.[17,18] Nevertheless, a deep understanding of the nanocoating formation and its stability were scarcely approached. For instance, Chen-Wiegart and co-workers[12] developed environmentally friendly Zr-based conversion nanocoatings on low carbon steel by using H_2ZrF_6 solutions with very low content (ppm) of cupric nitrate as additive. By using *in situ* synchrotron X-ray fluorescence microscopy (XRF), they found that the final nanocoating composition mainly consists on ZrO_2 and Cu_2O, Cu, and CuF_2 molecules in format of clusters above the film. Therefore, Cu ions were retained by chemical reaction adsorption and were not leached to the bath solution.

Herein, we describe the controlled deposition of a hydrated zirconium oxide monolayer, free of other metals or additives, in two grades of aluminum substrates: pure Al (AA1100) and Cu-rich alloy (AA2024). The films, which were obtained using the dip-coating (ZrCC-DC, or simply DC) and the electro-assisted deposition method (Zr-EAD), were fully characterized by microscopy, spectroscopy and electrochemical analyses. A mechanism based on the substrate nature is proposed, corroborating with previous works on CCC treatments. Finally, the barrier properties are also evaluated to determine the nanocoating resistance in electrolyte solution. Considering that H_2ZrF_6 is the main

component of most Zr-based conversion treatments, this study is appealing to broad applications.

3.2 *Materials and Methods*

3.2.1 Materials

Hexafluorozirconic acid (H_2ZrF_6, 50 % w/w in water) was supplied by Sigma-Aldrich Co. (Spain); sodium hydroxide (NaOH pellets), used to regulate the pH of the solution, was purchased from Panreac S.A. (Spain). The industrial alkaline degreaser (Saloclean 667N) was kindly supplied by Klintex Insumos Industriais Ltda. (Brazil). Aluminum plates (standard name AA1100), with rectangular geometry (5.0 × 1.4 × 0.3 cm^3), and aluminum alloy (standard name AA2024-T3), with disk format (3.5 cm in diameter and 4 mm of thickness) were used as substrates for ZrCC-DC and Zr-EAD formation. AA1100 is included in the commercially pure Al series. Its composition was provided by the supplier Irmãos Galeazi Ltda. (Brazil), in weight percentage (wt. %): Cu (0.34); Fe (0.42); Si (0.19); Mn (<0.01); Ti (<0.02); Zn (<0.01) and balanced aluminum. AA2024-T3 is a structural reinforced aluminum-copper grade with metallurgical temper code T3, which is referred to a solution heat-treated, cold worked and metal naturally aged. The AA2024 bar was supplied by Balumer S.L. (Spain) and its chemical composition is (wt. %): Cu (4.63); Mg (1.66); Mn (0.55); Fe (0.36); Si (0.31); and balanced to Al. The chemical composition analysis for AA2024 alloy was determined by ICP-AES (spectrometer SPECTROMAXx). Indium tin oxide coated polyethylene terephthalate sheets (ITO coated PET sheets, surface resistivity 60 Ω/square, Sigma-Aldrich) and pure copper plates were also used as complementary substrates for specific tests, described in the next sections.

3.2.2 Preparation and cleaning of aluminum substrates

The surfaces of the aluminum alloy substrates were prepared by grinding the surface with silicon carbide paper from #600-grit, down to up #2500-grit. Some samples were cleaned in ultrasound bath with isopropanol, followed by ethanol and, at last, acetone for 5 minutes at

room temperature in each solvent. This procedure was carried out for the production of Raw samples, providing a mild cleaning, aiming for the preservation of the naturally formed aluminum oxide layer (hereafter coded as "Raw"). The rest of the samples were thoroughly washed with water and acetone, and immersed in Saloclean 667N degreasing agent (pH 9.4, 70g/L, 70°C) for 5 min. Afterwards, the specimens were washed with distilled water in a sonication bath for 5 min, dried under a hot air stream, and stored under vacuum before use. This treatment generated the samples coded as "Bare", which represents the industrial conditions of metal degreasing before coating deposition.

3.2.3 Zirconium oxide nanocoating depositions (Zr-DC and Zr-EAD)

The conversion bath consists of an aqueous solution prepared with 100 mg of H_2ZrF_6 in 1L of water (0.015% v/v). The pH was adjusted to 3.5 with NaOH solution (1M). In order to produce the Zr-DC samples, panels were immersed in the conversion solution for 4 min, followed by water rinsing and hot air stream drying (before aging step, described below). By contrary, the Zr-EAD samples were obtained by a potentiostatic electrochemical method. The depositions were carried out with an Autolab PGSTAT302N potentiostat-galvanostat (Ecochimie) equipment, by using a three electrodes cell configuration. The working electrodes consisted of aluminum plates or disks, ITO foils and copper plates; the reference electrode was Ag|AgCl (3M, saturated); and the counter electrode was composed by graphite bar. The electrolyte used for EAD assays was the same used for the chemical conversion process. The experiments were carried out after open circuit potential (OCP) measurement (30 seconds), followed by the application of the desired potential during 4 min. The potentials used in this work were $-1.0\ V_{OCP}$ and $-1.5\ V_{OCP}$, generating the samples named "EAD −1.0 V" and "EAD −1.5 V", respectively. Such potentials were chosen on the basis of our

previous experience.[19,20] Samples coated by both dip-coating and EAD were further post-treated for 2 hours at 100 ºC, as aging step treatment to achieve the dehydration of the oxide layer and the reduction of defects.[21]

In parallel, ITO substrates were sequentially rinsed in deionized water, acetone and ethanol, with each rinsing step being carried out during 5 minutes, under sonication. After the washing process, the samples were submitted to the ZrO_2 electro-assisted deposition, with the same procedure and equipment described for the aluminum specimens. Those samples were used for the AFM and SEM measurements, in order to evaluate the isolated effect of EAD in a substrate where the conversion chemical reactions do not occur and to approach the influence of substrate homogeneity and roughness on the Zr-EAD coating. Moreover, more samples were prepared by EAD method, employing longer reaction time (60 min), to achieve thicker films and measure the mechanical properties of the oxide layer by nanoindentation test. In the same way, copper plates were also cleaned and, further DC or EAD methods were applied to compare the effect of Cu metal in the ZrO_2 production and the stability in electrolyte media.

3.2.4 Physical and chemical characterization

Scanning electron microscopy (SEM) studies were conducted with a Focus Ion Beam (FIB) Zeiss Neon 40 instrument (Carl Zeiss, Germany). One specimen of each coated substrate was selected for cross-section analysis. The cross-sections were cut using Focused Ion Beam (FIB) with gallium ions. The samples were previously coated with a sputtered carbon layer and received a thin protective layer of platinum (gas injection). First, an electron beam assisted Pt deposition was carried out to achieve Pt layer thickness of about 250 nm. The platinum layer was necessary to obtain smoother cross-sections by protecting the surface against the damage of the Ga ions. An initial coarse milling was carried out at 10 nA, followed by a finer milling at 500 pA, which provided regular cross-sections. The resulting cross-sections were 15 µm long

and 3 μm deep. For SEM analysis an electron beam of 5 kV was applied. The thickness of Zr-DC and Zr-EAD coatings was evaluated after 50 measurements using high magnification images. Analysis of variance (one-way ANOVA) was carried out with a confidence level of 95 %, followed by a Turkey test for means comparison of the measured thicknesses. Atomic force microscopy (AFM) was conducted to obtain topographic information (2D Phase images) and roughness (3D height images) of the modified surfaces. The experiments were carried out with an AFM Dimension microscope, equipped with NanoScope IV controller and NanoScope Analysis software (1.20 Veeco), under ambient conditions and by using tapping mode. The equipment operated with a frequency of 150 kHz and a with force constant of 5 N/m. The scanning frequency was set between 0.6 and 0.8 Hz and the area of analysis varied with windows of 50 × 50 μm^2 and 20 × 20 μm^2. Several measurements were performed on the top of the samples, which produced reproducible images similar to those displayed in the results section.

The chemical compositions of the substrates and coatings were determined by X-ray photoelectron spectroscopy (XPS) and energy dispersive X-ray spectroscopy (EDX). XPS analyses were performed in a SPECS system equipped with a high intensity twin anode X-ray source XR50 of Mg/Al (1253 eV/1487 eV) operating with the selected Al anode at 150 W, and by using a Phoibos 150 MCD-9 XP detector. For the preparation of the samples, the bare alloys were first polished, washed three times with isopropanol, ethanol, deionized water and acetone, under ultrasound bath for 5 min, dried under nitrogen flow and vacuum. Afterwards, sputtering of the surfaces with argon gas (2 min) was applied to eliminate the surface contamination by carbon compounds. All spectra were calibrated with the C 1s peak (284.5 eV). The following elements: C 1s, O 1s, Al 2p, Zr 3d, and Cu 2p were analyzed for the high-resolution peaks and plotted after deconvolution.

Water contact angle (WCA) measurements were carried out with an OCA 15EC instrument (DataPhysics GmbH, Filderstadt) using the sessile droplet method at room temperature, to evaluate the wettability changes of the

modified surfaces. Data were recorded after the water droplet deposition (0.5 μL) and stabilization (30 s), using SCA 20 software, and were reported as an average of ten independent measures for each sample.

The hardness and elastic modulus of thin Zr-EAD films were measured using an MTS Nanoindenter XP instrument, with a Berkovich diamond tip calibrated with fused silica standard. The results were analyzed with the Oliver and Pharr method.[22,23] The sample prepared on ITO substrate, coated by EAD technique at −1.0 V during 60 minutes, was used as model to estimate the mechanical properties of the film. Long generation time was necessary to produce thick coatings in order to obtain reliable values of mechanical properties under nanoindentation forces.

3.2.5 Electrochemical characterization of zirconium oxide nanocoating

The potentiodynamic and electrochemical impedance spectroscopy (EIS) studies were performed in an Autolab PGSTAT302N potentiostat-galvanostat (Ecochemie) equipment. The electrochemical cell consisted of three electrodes, having the sample set as the working electrode, a platinum wire as counter electrode and a Ag|AgCl (KCl, 3M) as reference electrode. The tested area was 0.785 cm^2 and the electrolyte used was 0.05 M NaCl aqueous solution. The potentiodynamic curves were registered after 30 minutes of open circuit potential (OCP) stabilization. The potential sweep ranged from −0.3 V_{OCP} to +1.0 V_{OCP} with a scan rate of 1 mV/s. For short run times (0.5h), the cleaned, etched and coated substrates were evaluated per triplicate and the effect of the cathodic potential (−1.0 V or −1.5 V) used for the generation of the coating was compared.

EIS experiments were performed to evaluate the polarization resistance of the ZrO_2 nanolayer, after 30 min of time exposure to the electrolyte solution. The amplitude of the EIS perturbation signal was 10 mV, the frequency ranged from 10^5 to 10^{-1} Hz taking measurements of 10 frequencies per decade. The same cell and electrodes reported for polarization tests were used here.

3.3 *Results and discussion*

3.3.1 Influence of the substrate in the deposition of Zr-EAD films

There are some studies that corroborate the effective role of intermetallic particles in alloyed aluminum as promoters of ZrCC deposition,[8,24] but apparently their effect in the Zr-EAD has not been explored yet. Pioneer works of Zr-based coatings onto aluminum substrates were also limited to CCC treatments.[25–27] In all cases, the major drawback is the high porosity of the oxide layer and the limited thickness of the ZrO_2 film (10–80 nm), obtained by CCC processes, that preclude a good coating analysis. Therefore, this section will focus in the surface characterization of ZrO_2 with controlled deposition by EAD method.

The properties of the ZrO_2 layer will depend on the substrate nature and its roughness. Therefore, indium-tin oxide substrates, with very low roughness (4.3 ± 0.9 nm) were chosen to explore the deposition of ZrO_2 nanometric layer, taking the advantage of the low effect of the substrate roughness on the nanocoating obtaining. The other advantage of ITO substrate is that it does not undergo the reactions involved in the self-deposition of the ZrO_2 by the CCC method, *i.e.* the zirconium coating can only be obtained with the application of current or voltage (EAD method). **Figure 3.3.1** contains the topographic images of these specimens.

As seen in the topographic images, the roughness of the ZrO_2 layer is practically the same than that of the substrate without EAD coating, independently of the potential applied. This evidenced that the formed film reproduces the underlying substrate roughness, as presented in **Table 3.3.1**.

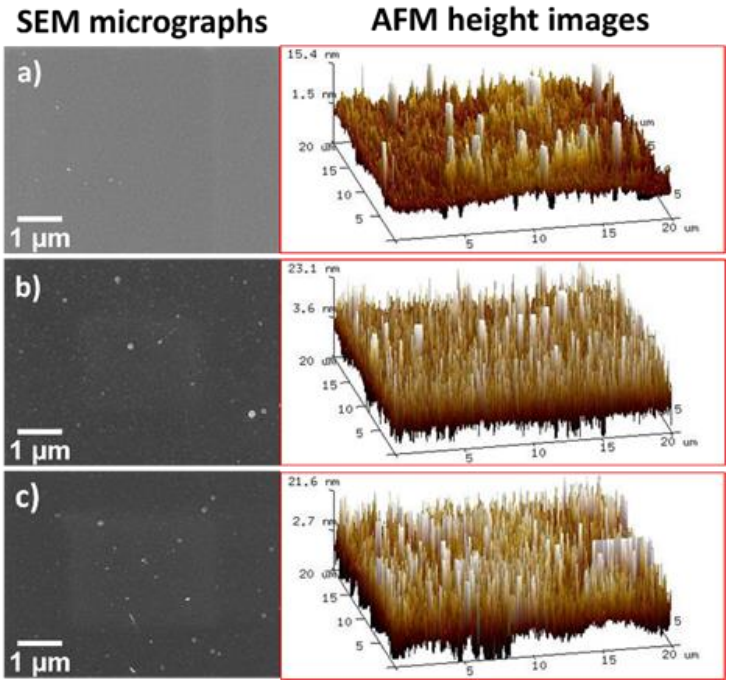

Figure 3.3.1. SEM (left) and AFM 3D height images (right) on ITO substrates: **a)** after ultrasonication bath cleaning; **b)** after Zr-EAD at −1.0 V; and **c)** after Zr-EAD at −1.5 V coating generation.

Table 3.3.1. Roughness of aluminum surfaces treated with degreasing agent (Bare) and electro-assisted deposition of zirconium conversion coating (EAD). The values of the nanocoatings deposited in the aluminum substrates (rough surface) were measured using AFM 3D topographic analyses (**Figure 3.3.10**) and were compared to that deposited in ITO substrates (smooth and very homogenous surface).

Substrate	ZrO_2 deposition method	Roughness (nm ± SD)
AA1100	Bare	57.2 ± 28.4
	EAD at −1.0 V	29.8 ± 7.4
	EAD at −1.5 V	41.4 ± 3.8
AA2024	Bare	35.6 ± 6.6
	EAD at −1.0 V	24.9 ± 2.2
	EAD at −1.5 V	49.4 ± 9.3
ITO	Bare	5.0 ± 0.4
	EAD at −1.0 V	6.6 ± 0.4
	EAD at −1.5 V	6.3 ± 0.5

The root mean square roughness (Rq) values, which were determined by AFM using a scan window size of 20 × 20 μm^2, were 5.0 ± 0.4 nm, 6.6 ± 0.4 nm, and 6.3 ± 0.5 nm, respectively for ITO bare, Zr-EAD/ITO −1.0 V and Zr-EAD/ITO −1.5 V.

Figure 3.3.2 contains the results from the nanoindentation measurements performed with the films. **Figure 3.3.2a** shows that a nearly steady plateau was reached for both hardness and elastic modulus after the nanoindenter reaches the end of the oxide layer in ITO substrates. Those values correspond to the properties of the substrate. By contrary, the nanoindentation curves obtained for AA1100 plates and AA2024 disks coated with ZrO_2 films show high deviations (**Figure 3.3.2b** and **Figure 3.3.2c**, respectively). This behavior is a consequence of a relatively high surface roughness of the substrate when compared to the nanoscale dimensions of ZrO_2 coatings. The nanoindenter experiments over aluminum plates/ZrO_2 cannot be taken into consideration for the evaluation of its mechanical properties due to the very high deviations of results, which prevent any trustful conclusions in such metallic substrates.

Increase of electrochemical reaction time (from 4 min to 60 min) led to the obtaining of thick ZrO_2 films with elastic modulus of 14.1 ± 2.1 GPa and hardness of 1.3 ± 0.1 GPa, derived from nanoindentation measurements. Such values do not correspond to solid fully dense zirconia, after sintering process (>17 GPa and 250 GPa, for hardness and elastic modulus, respectively),[28] as the coating does not undergo traditional ceramic processing, indicating that the film should have more porous microstructure than that of bulk material itself.[29–31]

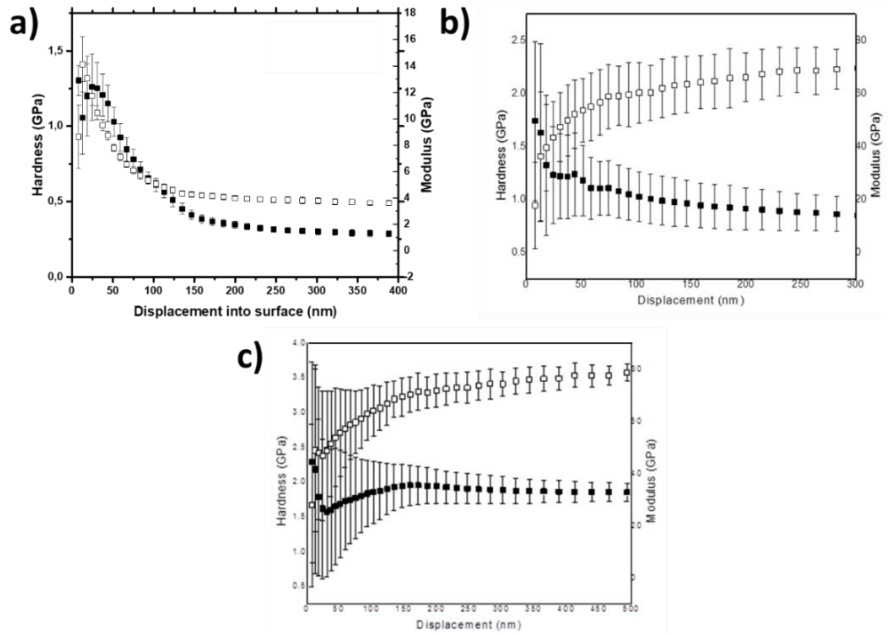

Figure 3.3.2. Elastic modulus and hardness as a function of nanoindenter penetration into sample surface: **a)** Zr-EAD −1.0 V in ITO substrate; **b)** Zr-EAD −1.0 V in AA1100 plates, **c)** Zr-EAD −1.0 V in AA2024. All coatings generated at 1h by EAD method. Hardness is given in black filled dots and elastic modulus in empty dots.

Regarding the deposition of ZrO_2 in aluminum substrates, the thickness measurement by AFM is impracticable due to the nanoscale range of the films (20-30 nm) compared to the high roughness of soft metal substrate after polishing pre-treatments. Here, such measurements were carried out with FIB-SEM microscopy. The SEM images, showing a detail of the cut provoked by the electron beam, demonstrate that ZrO_2 films are perfectly adhered to the substrate (**Figure 3.3.3**).

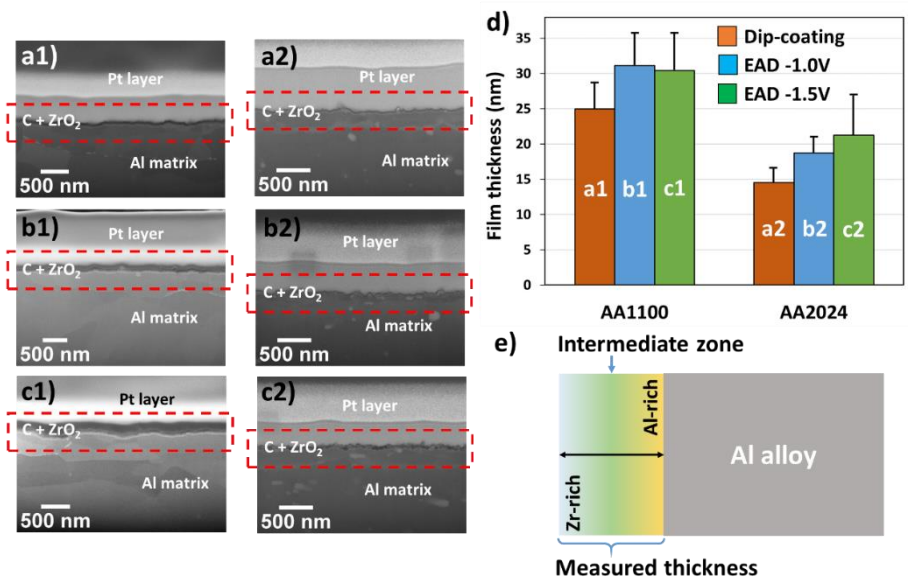

Figure 3.3.3. a-c) Cross-section of FIB-SEM micrographs showing the ZrO_2 film thickness between Pt layer and metal substrate, previously degreased with alkaline solution (Bare). **d)** Values of thicknesses and deviations of samples AA1100 and AA2024, evaluated by HR-SEM. **e)** Schematic representation of ZrO_2 layer over Al alloy surfaces. Letter codification: a) Dip-coating method; b) Zr-EAD at −1.0 V; c) Zr-EAD at −1.5 V; and number codification: 1) AA1100 and 2) AA2024 plates. SEM magnifications: a1) 81.81 kX; a2) 100 kX; b1) 72.43 kX; b2) 100 kX; c1) 85.28 kX; and c2) 100 kX. Red rectangles indicate the region used for the thicknesses measurements.

The substantial challenge is found when comparing the two substrates in **Figure 3.3.3d**. AA1100 plates have the highest film thicknesses (**Table 3.3.2**). The explanation is that the zirconium layer does not correspond exclusively to ZrO_2 compounds, as the film has a gradient in composition. The closer to the substrate interface, the higher the Al concentration, which is related to a combination of Al_2O_3/AlOOH passivation layers; whereas the outer surface is rich on Zr atoms (detected by XPS analysis, as will be discussed in section 3.3.2). This implies that there is not a defined interface between the ZrCC and the native oxide/hydroxide layer and both contribute to the measured thicknesses. A simplified profile in Zr and Al concentrations, as a function of depth, is shown in **Figure 3.3.3e**. The depth–dependent element concentration profile on zirconium-based conversion coatings has been already demonstrated by

other authors using techniques such as Auger Electron Spectroscopy (AES),[16,32] Time-of-Flight Secondary Ion Mass Spectrometry (ToF-SIMS)[33] and Glow Discharge Optical Emission Spectroscopy (GDOES).[34] The thickness of the native oxide layer was determined to be at around 30 nm.

The local deposition of Zr-oxide based coatings on AA1100 is due to its high amount of passivation layers (Al_2O_3/AlOOH), compared to the surface with copper rich sites (AA2024). Moreover, previous work proved that the local composition of ZrO_2 is conditioned by the presence of copper in the alloy surface (AA6014 contains Mg ≤0.8 wt.%, Fe ≤0.35 wt.%, Si ≤0.6 wt.%, Cu ≤0.2 wt.%, Mn ≤0.2 wt.%, the rest of Al).[35] They found higher amount of Al atoms than Zr atoms when alloys without Cu were investigated (AA1050 contains Al ≥ 99.5 wt%, Fe ≤ 0.3 wt.%); which corroborates our results. Thus, we found similar effect and the same tendency on ZrO_2 layer deposition, by using XPS analysis (next section 3.3.2). The novelty in this work is that the aluminum alloy used has the highest Cu weight percentage (AA2024 contains Cu ≥ 4.5 wt.%) among Al alloys. Therefore, the effect on the nanocoating deposition is more evident with respect to samples without copper, as for example in AA1100 and AA1050 alloys; or with very low content, as is the case of AA6014 alloy.

On the other hand, the analysis of variance followed by Turkey test for means comparison (significance level of 0.05) indicates greater film thicknesses obtained by EAD, regardless of the applied potential, when compared to the DC method (**Table 3.3.2**) on both substrates. This probably occurs due to the improved ions migration induced by potential application.

Table 3.3.2. Thicknesses of ZrO_2 nanocoatings, obtained by cross-section analysis of FIB-SEM micrographs, for samples generated with two different methods (DC and EAD), and with two different deposition potentials (−1.0 V and −1.5 V) in EAD.

Substrate	ZrO_2 deposition method	Thickness and SD (nm)
AA1100	DC	24.9 ± 6.7
	EAD at −1.0 V	31.1 ± 8.2
	EAD at −1.5 V	30.4 ± 9.8
AA2024	DC	14.5 ± 4.1
	EAD at −1.0 V	18.7 ± 4.0
	EAD at −1.5 V	21.2 ± 10.1

3.3.2 Zr-EAD nanocoating composition

The XPS survey spectra obtained from the analyzed samples are depicted in **Figure 3.3.4**. As can be seen, the presence of atoms from substrate and zirconium oxide coating is detected, as well as some carbon and fluorine atoms.

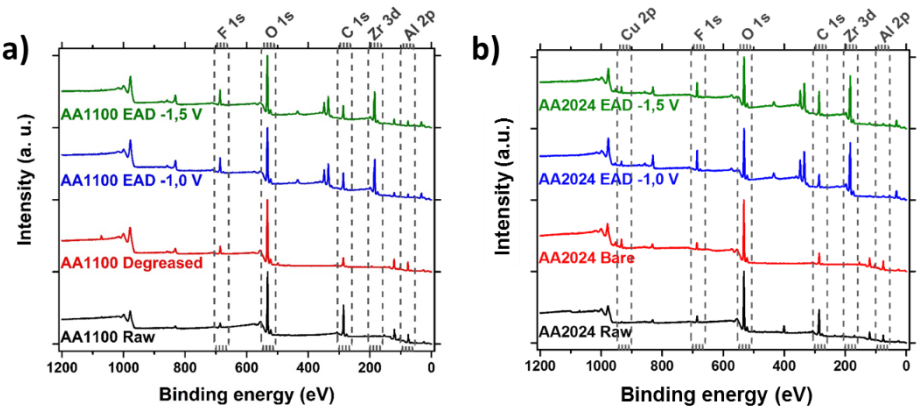

Figure 3.3.4. XPS survey spectra showing the main elements found in the surfaces of Raw, Bare and Zr-EAD samples, obtained with −1.0 V and −1.5 V in: **a)** AA1100 plates and **b)** AA2024 disks.

This analysis revealed a great contribution of some compounds present in the metal-zirconium oxide coating interface, due to the low thicknesses of such films and to the influence of metal pre-treatment. The deconvolutions of the Al 2p, Zr 3d and Cu 2p peaks are shown in **Figure 3.3.5**, **Figure 3.3.6** and **Figure 3.3.7**, respectively.

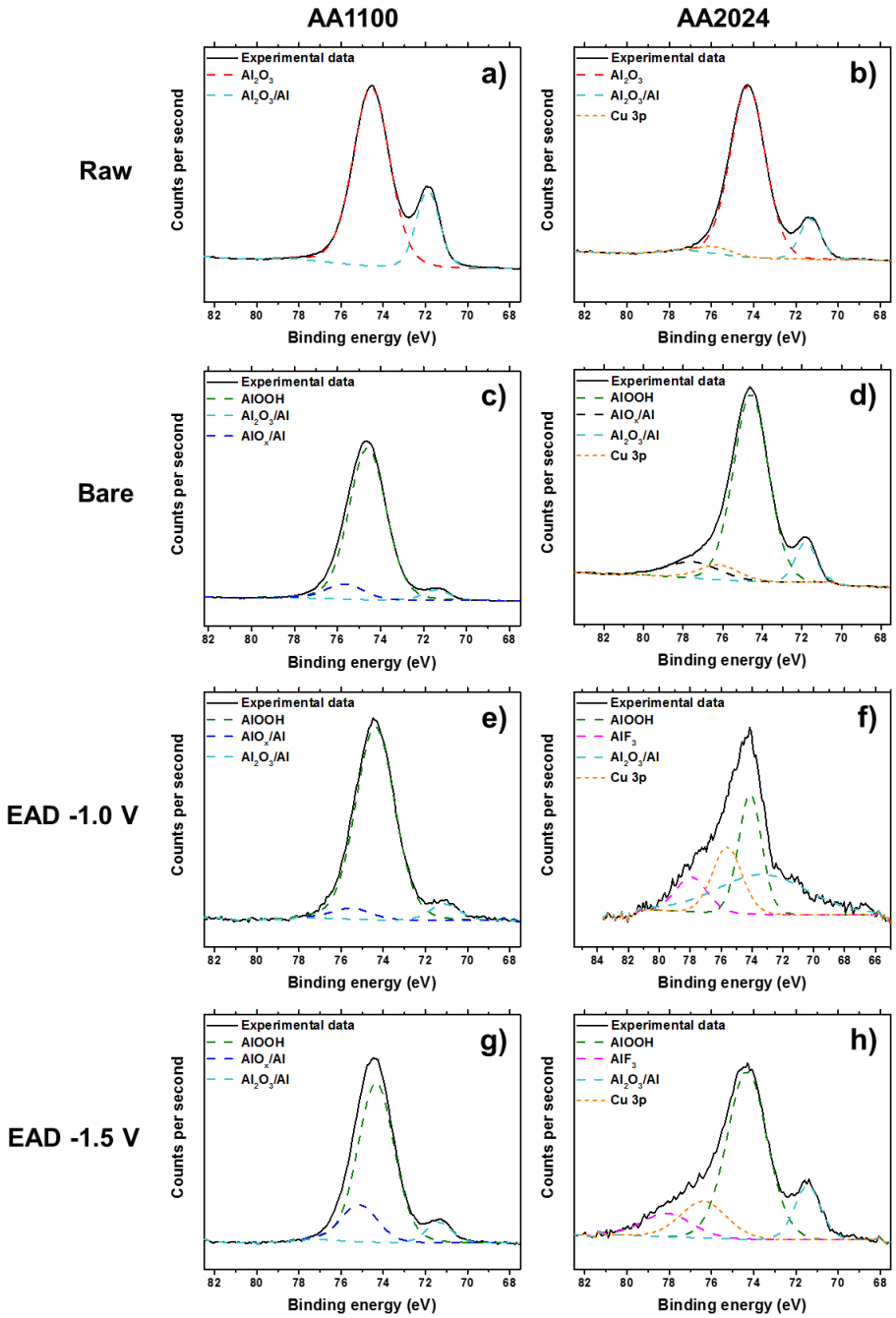

Figure 3.3.5. XPS high-resolution spectra of Al 2p region, before (Raw, **a-b**); after alkaline etching process (Bare, **c-d**); and after electro-assisted deposition of ZrO_2, generated at −1.0 V (**e-f**) and −1.5 V (**g-h**). Left: AA1100 samples and right: AA2024 samples.

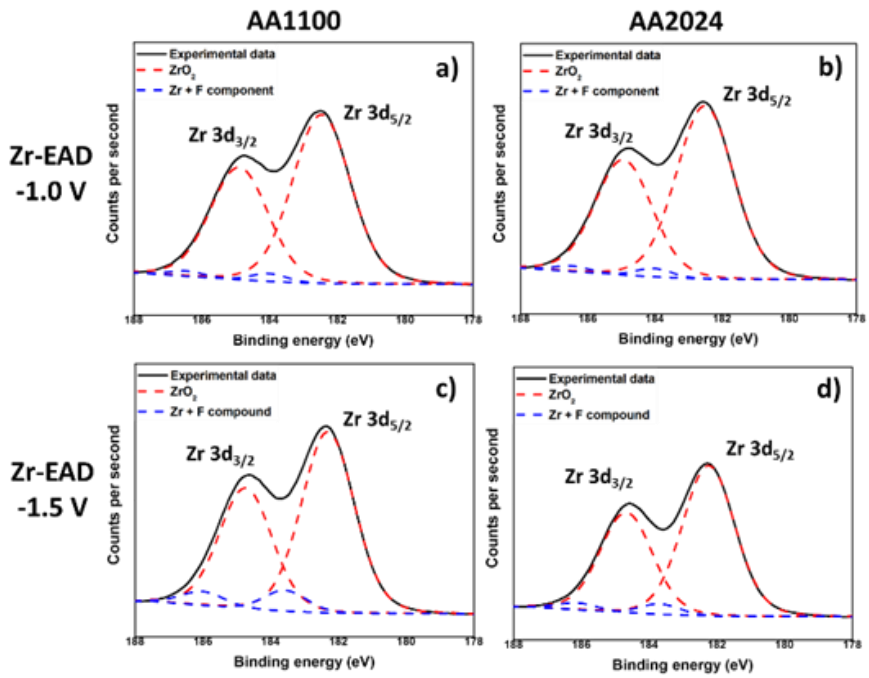

Figure 3.3.6. XPS high-resolution spectra of Zr 3d region, after electro-assisted deposition of ZrO_2: **a)** AA1100/EAD −1.0 V; **b)** AA2024/EAD −1.0 V; **c)** AA1100/EAD −1.5 V; and **d)** AA2024/EAD −1.5 V.

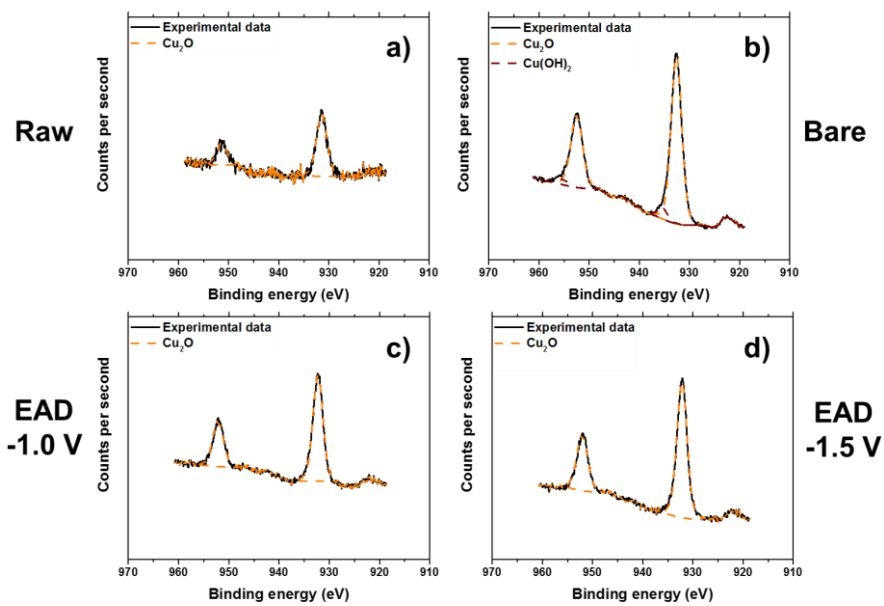

Figure 3.3.7. Cu $2p_{1/2}$ (956 eV) and Cu$2p_{3/2}$ (933 eV) XPS high resolution spectra of: **a)** Raw, **b)** Bare, **c)** Zr-EAD −1.0 V, and **d)** Zr-EAD −1.5 V, detected in AA2024 disks.

The most relevant atoms were aluminum, derived from the substrate and from oxidized Al compounds; fluorine, derived from the bath solution and further reaction with Al^{3+} (AlF_3); and copper, derived from Cu oxidation to Cu^{+1} (Cu_2O) and Cu^{2+} ($Cu(OH)_2$). The latter was exclusively detected in the AA2024 substrates, which have high content of Cu as alloying element. The abovementioned compositions were observed thanks to the careful deconvolution of the XPS high resolution experimental data and contrasting with XPS database.

It is evident that mild surface cleaning with organic solvents (Raw), for example, does not remove the native Al oxide and alloying elements from the metal surface (**Figure 3.3.5a-b**), whereas alkaline etching (Bare) causes a great effect. In a strongly alkaline environment, a powerful oxidizing agent is introduced, then the metal oxidation and the formation of one (or more) of the solid oxides (Al_2O_3/AlO_x), and metal hydroxides (AlOOH) is expected (**Figure 3.3.5c-d**).[36,37] Indeed, in the particular case of Al alloys, de-alloying of the elements close to the surface is also achieved. It was observed in the high-resolution spectra of Cu 2p, by detection of the presence of Cu_2O and $Cu(OH)_2$ molecules (**Figure 3.3.7**) and this phenomenon has been extensively reported by several authors.[38–41] Thus, the Cu atomic concentration is much higher for the Bare sample than for the other treatments in AA2024. After the zirconium deposition, the high resolution spectrum of Al 2p is almost invariable in any EAD potentials, but has much lower atomic percentage in AA2024, if compared to AA1100 (**Table 3.3.3**). It should be emphasized that Al 2p region has also a small contribution of Cu 3p content in the same region, as seen in the **Figure 3.3.5f-h**, and it must be taken into account for the calculation of the Al atomic percentage in AA2024 samples.

The atomic percentage concentrations of those elements are expressed in **Table 3.3.3**.

Table 3.3.3. Atomic concentration of Al 2p, Zr 3d, Cu 2p and O 1s, obtained from the XPS high resolution spectrum of each orbitals, and comparative apparent atomic ratios of main elements. The values of Al 2p in AA2024 samples are the neat contribution of this orbital, having docked the contribution of Cu 3p from deconvoluted peaks of Al 2p region (see **Figure 3.3.5**).

Sample code	Al 2p (%)	Zr 3d (%)	O 1s (%)	Cu 2p (%)	Al/Zr ratio	Cu/Al ratio
AA1100 Raw	27.23	-	27.47	-	-	-
AA1100 Bare	32.10	-	42.42	-	-	-
AA1100 EAD − 1.0 V	12.08	13.28	35.04	-	0.91	-
AA1100 EAD − 1.5 V	16.73	11.90	37.42	-	1.41	-
AA2024 Raw	21.25	-	29.70	0.03	-	0.001
AA2024 Bare	38.16	-	35.25	0.31	-	0.008
AA2024 EAD − 1.0 V	6.44	22.19	34.39	0.17	0.29	0.045
AA2024 EAD − 1.5 V	8.24	16.12	29.75	0.20	0.51	0.062

Taking into account the deconvolution of Zr high resolution spectrum, with two peaks of Zr $3d_{5/2}$ and Zr $3d_{3/2}$ at binding energies of 182.5 eV and 185 eV (**Figure 3.3.6**), respectively, the inorganic coating is mainly composed by zirconium oxide, whereas some minor residual fluorine complexes are probably present.[16,24,42] Fluorine element observed in EAD samples (**Figure 3.3.4**) mostly arises from the bath, whereas that detected in Raw and Bare substrates comes from some equipment contamination. Zhang *et al.*[9] have reported that conversion coatings in AA5052 aluminum alloy (Mg-rich alloy) obtained from fluorine salt solutions contains hydrated AlF_3 compound trapped among the metal oxides. As the contribution of fluorine has been measured to be between 2-3 %, and even less for Raw and Bare substrates, it has been considered to not interfere significantly in the interpretation of the results regarding the main components. The EAD coating composition found was

consistent with that reported for DC method.[24,35,42] In AA1100 samples, the Al-rich and Zr-rich zones pointed out in the scheme of **Figure 3.3.3e**, are not differentiated. The apparent atomic ratio of Al/Zr is close to unit (0.91 and 1.41, for EAD −1.0 V and EAD −1.5 V, respectively); whereas in AA2024 such values have been reduced to a factor of 1/3 and 1/2 (**Table 3.3.3**) for each applied potential, respectively. Based on XPS evidences, undoubtedly, the unique explanation for the high content of Zr atoms in AA2024 is the distribution of ZrO_2 molecules over the abovementioned surface, *i.e.* the homogeneity of the film covering the substrate, which seems to be favored by both, the use of the EAD technique and the presence of Cu-rich sites.

In conclusion, the slightly higher thicknesses measured for AA1100 samples can be the result of a thick aluminum oxide/hydroxide layer in the boundary zone between Al metal surface and zirconia layer, as explained before. So, the Zr-rich zone is expected to be more homogenous and thinner in AA2024 than in AA1100, which agrees with the known favorable effect of the intermetallic (with cathodic nature, like copper-aluminum) for the zirconium oxide film formation, described above. Additionally, comparing the two cathodic potentials used in EAD treatments, the low voltage (−1.0 V) seems to potentiate a better surface coverage, as will be explained in the next section.

3.3.3 Zr-EAD nanocoating surface topography

The morphology of the nanometric films was evaluated by SEM and AFM. In **Figure 3.3.8**, a clear cauliflower structures was evidenced after the ZrO_2 growth on top of aluminium surfaces, which is characteristic of porous materials.[43–45] The globular agglomerates observed in samples AA1100 (**Figure 3.3.8a-c**) are bigger than that obtained in AA2024 (**Figure 3.3.8d-f**) and it affects the heterogeneity of Zr-based coatings.

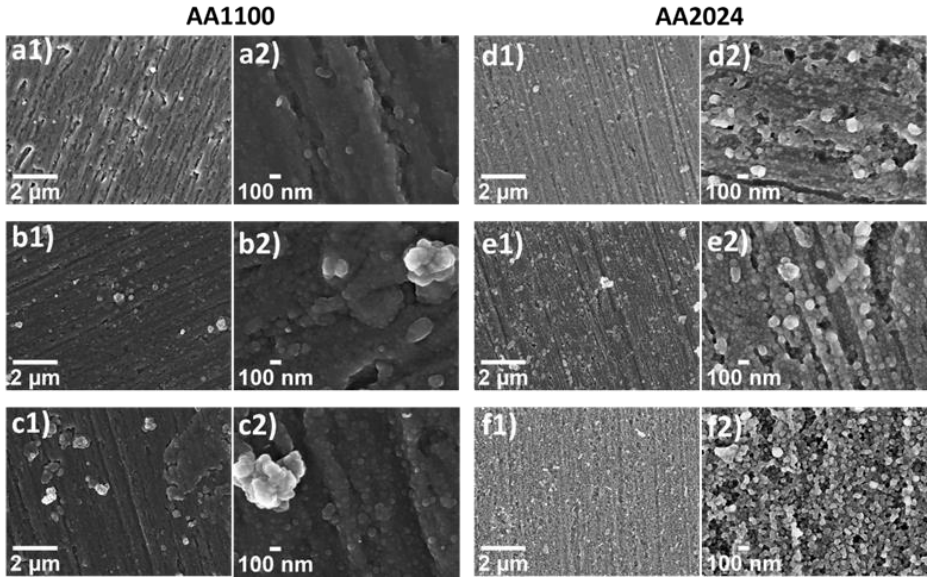

Figure 3.3.8. SEM micrographs at low (**1**, 30 kX) and high magnifications (**2**, 150 kX), evidencing the morphology of zirconium oxide in the following samples: **a)** Zr-DC/AA1100; **b)** Zr-EAD − 1.0 V/AA1100; **c)** Zr-EAD − 1.5 V/AA1100; **d)** Zr-DC/AA2024; **e)** Zr-EAD − 1.0 V/AA2024; and **f)** Zr-EAD − 1.5 V/AA2024.

Long reaction time (60 min) leads to an increase on cauliflower globular agglomerated structures (**Figure 3.3.9a**) and, therefore, to highly heterogeneous films with poor mechanical properties, showing thicker coating and cracks (**Figure 3.3.9b-c**), not desirable for industrial application aims.

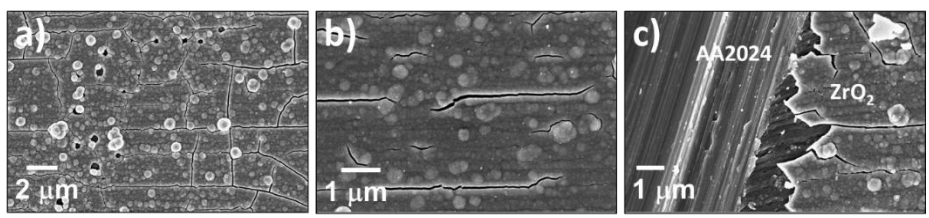

Figure 3.3.9. SEM micrographs evidencing the high density of ZrO_2 agglomerates in AA2024 coated samples (EAD generated for 60 min at potentiostatic condition). The magnifications are: **a)** 16kX; **b)** 38kX; and **c)** detail of the ZrO_2 thick layer and the substrate at 26kX.

AFM was performed in order to get a deeper understanding on the surface morphology by application of EAD method. AFM 3D height images of the surfaces of the studied coatings are shown in **Figure 3.3.10**.

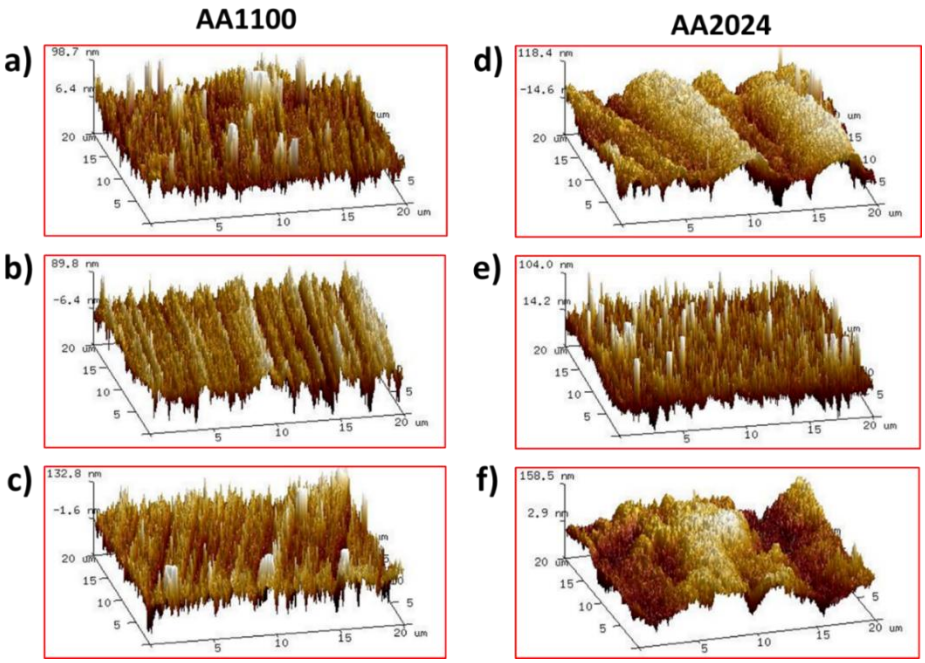

Figure 3.3.10. AFM 3D height images of: **a)** AA1100 bare sample, after raw material degreasing; **b)** Zr-EAD at −1.0 V/AA1100; **c)** Zr-EAD at −1.5 V/AA1100; **d)** AA2024 bare sample, after raw material degreasing; **e)** Zr-EAD at −1.0 V/AA2024; **f)** Zr-EAD at −1.5 V/AA2024.

The surface roughness (**Table 3.3.1**) decreased from 57.2 ± 28.4 nm in AA1100 Bare surfaces to 29.8 ± 7.4 nm and to 41.4 ± 3.8 nm, after Zr-EAD at −1.0 V and Zr-EAD at −1.5 V, respectively. Similar result was obtained for AA2024 where the roughness decreased from 35.6 ± 6.6 nm to 24.9 ± 2.2 nm after Zr-EAD at −1.0 V, whereas with Zr-EAD at −1.5 V the value increased (49.4 ± 9.3 nm) respect to Bare sample (35.6 ± 6.6 nm). By contrary, in ITO substrates, the roughness differences are negligible, as expected, thanks to the high nanometric smoothness of such surfaces, as explained in the section 3.3.1.

Particularly, detail observation of AFM 2D phase images reveals important differences among pure Al and Cu-rich Al surfaces (**Figure 3.3.11**). ZrO_2 successfully filled the valleys generated by the mechanical polishing marks, offering a more homogenous and smooth surface in AA2024 (**Figure 3.3.11e-f**) than in AA1100 samples (**Figure 3.3.11b-c**). Moreover, AFM analysis corroborated the morphology aspects observed by SEM, a high cathodic

voltage (−1.5 V) implies more roughness due to the higher density of ZrO_2 agglomerates generated. In all cases, AFM phase images presented similar and small changes in phase angle, corresponding to a homogenous coating, where no more than one material is exposed on the metallic surface.

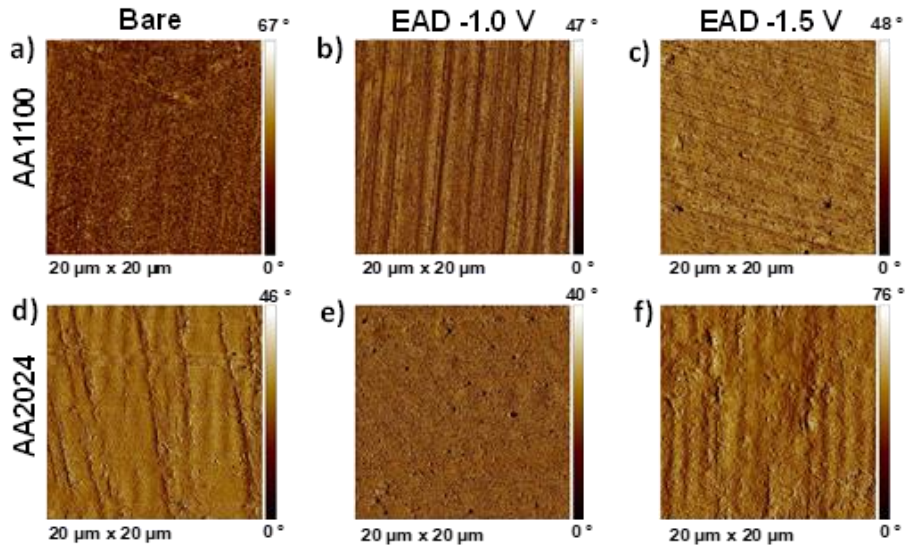

Figure 3.3.11. AFM 2D phase images of: **a)** AA1100 Bare sample, after raw material degreasing; **b)** Zr-EAD at − 1.0 V/AA1100; **c)** Zr-EAD at − 1.5 V/AA1100; **d)** AA2024 bare sample, after raw material degreasing; **e)** Zr-EAD at − 1.0 V/AA2024; **f)** Zr-EAD at − 1.5 V/AA2024.

3.3.4 Wettability

The density of oxide clusters observed in Zr-EAD specimens, showed in **Figure 3.3.8**, influenced both the homogeneity and the wettability of the films. The Zr-oxide films assessed in this study were hydrophilic in nature, with WCAs below 90°, as can be seen in **Figure 3.3.12**.

This can be easily explained by comparing the different pre-treatments and the chemical nature changes provoked by each one. Raw samples have similar WCA in both AA1100 and AA2024 surfaces because the metal-air interface was not altered from etching treatments and the influence of the alloying elements is insignificant. By contrary, superhydrophilic surface was observed when the aluminum was exposed to alkaline etching (Bare samples), with WCA of 15-18°.[46] In this case, the presence of Al_2O_3/AlOOH passivation layers, observed either

in AA1100 or in AA2024 samples (**Figure 3.3.5**), are the responsible for the great affinity of water molecules to this surface. Additionally, the etching of the surface with alkaline solution and the formation of oxide-hydroxide layers enhanced the roughness (**Table 3.3.1**) and it is another reason for their high wettability.[47,48]

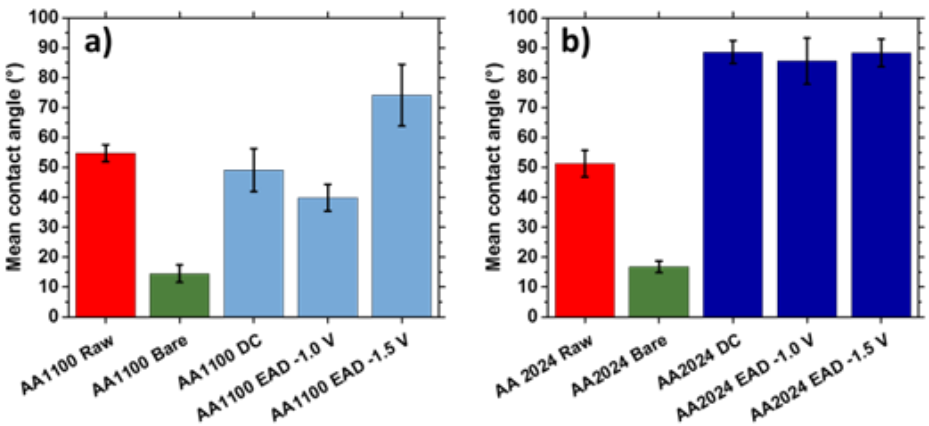

Figure 3.3.12. Wettability of **a)** AA1100 and **b)** AA2024 substrates before and after the application of the following treatments: Raw (metal plates cleaned with acetone); Bare (metal plates degreased with Saloclean 667N and grinded); DC (dip-coating method); and EAD (electro-assisted deposition at two different potentials).

Moving to the zirconium oxide layers generated after conventional ZrCC (DC method) and comparing with Zr-EAD method, the most important changes were again observed in AA2024 samples (**Figure 3.3.12b**). The water affinity decreased, demonstrating that the chemical nature of this substrate plays an important role, causing the reduction of coating roughness and, consequently, the changes observed in the wettability properties.

3.3.5 Mechanism of ZrO_2 deposition in AA1100 and AA2024 surfaces

In conventional zinc phosphate pre-treatment, the initial step is a pickling attack of the metal surface by free phosphoric acid and evolution of hydrogen gas in aqueous solution. The following steps are: the coating deposition (usually 2-4 μm in thickness) and the generation of high amount of sludge. Thus, replacement of zinc phosphate pre-treatments by zirconium oxide coatings is

estimated to corroborate on both, the reduction of industry waste and reduction of piece weight by the deposition of an ultrathin metal oxide film (15-30 nm).[49]

The chemical conversion coating of Zr oxide is strongly dependent on the consumption of protons[50] and on the presence of intermetallic compounds[51] on the metal surface. It is generally accepted that the first process occurring during the conversion coating formation is the thinning and partial removal of the native aluminum oxide layer by the free fluorides in the conversion bath, generating aluminum fluorides (**Equation 3.1**), as represented in the upper part of both substrates at **Figure 3.3.13**. Then, the metal surface faces a localized shift on the pH towards alkaline values due to the water electrolysis, through the generation of oxygen and consuming of protons (**Equation 3.2a-b**). Afterwards, the precipitation of hydrated zirconium oxides takes place, according to the reaction shown in **Equation (3.3)**.

Alumina pickling:

$$Al^{3+}_{(aq)} + ZrF_6^{2-}_{(aq)} \rightarrow AlF_6^{3-}_{(aq)} + Zr^{4+}_{(aq)} \quad \textbf{(3.1)}$$

Water electrolysis:

$$2\,H^+_{(aq)} + 2e^- \rightarrow H_{2\,(g)} \quad \textbf{(3.2a)}$$

$$H_2O_{(l)} \rightarrow \tfrac{1}{2}\,O_{2\,(g)} + 2\,H^+_{(aq)} + 2e^- \quad \textbf{(3.2b)}$$

Coating deposition:

$$Zr^{4+}_{(aq)} + 4\,H_2O_{(l)} \rightarrow ZrO_2{\cdot}2\,H_2O_{(s)} + 4\,H^+_{(aq)} \quad \textbf{(3.3)}$$

Hydrogen evolution consumes one of the products of the fourth reaction (H^+), that occurs in the cathode, therefore, this unbalances the reaction in the direction of products formation, enabling the production of more electro-assisted deposited coating (autocatalytic effect). Control over the cathodic potential applied (−1.0 V instead of −1.5 V) regulates the hydrogen gas

generation, and thus, it can be reduced to avoid the obtaining of high porous films; which in turn is not possible with DC method.

Those reactions are particularly favored in aluminum alloys where the intermetallic particles are cathodic relative to the aluminum matrix, as other authors have already observed for the application of tri-cationic phosphate pre-treatments on AA2024 alloy.[52,53] The abundance of such cathodic sites and the preferential deposition on their surroundings is depicted in **Figure 3.3.13a**.

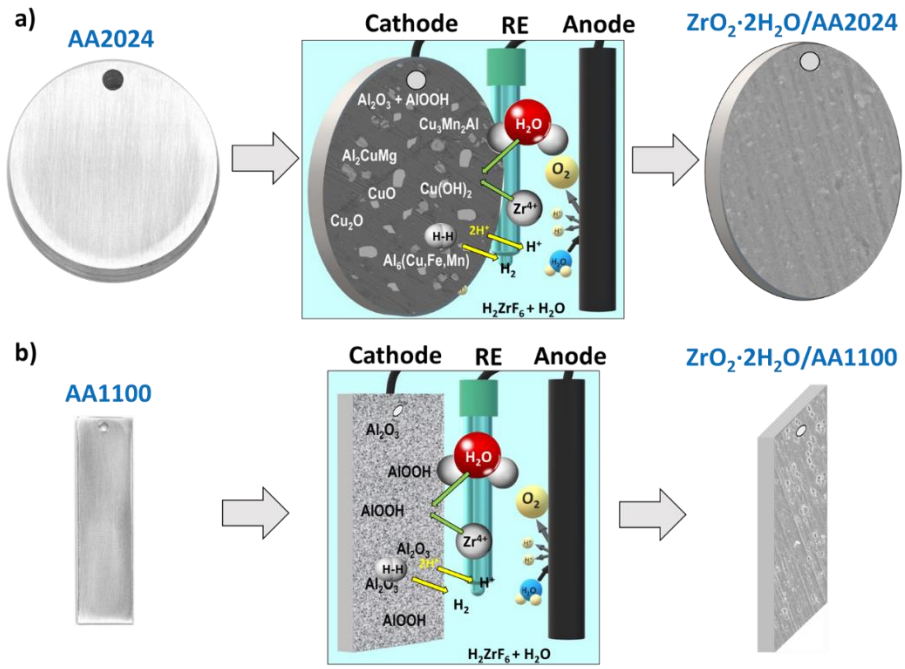

Figure 3.3.13. Illustration of the best conditions for Zr-EAD deposition on: **a)** AA2024 disks and **b)** AA1100 aluminum plates. From left to right: Bare substrates; application of −1.0 V of cathodic potential and 4 min of electrochemical reaction; Zr-EAD coated specimen. Arbitrary scale has been used for the visual representation of the reactions.

It should be mentioned that the representation shown in **Figure 3.3.13** is a simplification of the whole process and dissolution reactions of the native oxides and hydroxides were not shown. The key aspect regarding the role of the substrate is the presence of intermetallic particles on AA2024 surfaces (**Figure 3.3.13a**), which are absent in AA1100 (**Figure 3.3.13b**). The presence of intermetallics and other Cu-rich particles offers a faster deposition of ZrO_2

molecules in AA2024 substrates; and it would be one of the reasons for obtaining thicker films in such samples, as explained above. In both substrates, the porosity of the native oxide/hydroxide Al molecules also helps Zr^{4+} migration to the inner interface layer. This effect is raised by the potential application, which did not occur with chemical conversion coating deposition.

In summary, both EAD and DC techniques enable an uniform film deposition [18,54]. It has been observed that, despite the ZrO_2 coating formation is supposedly favored by the application of low cathodic potential in electro-assisted method, the correct mechanism is probably a combination of both a chemisorption process and the electro-assisted one happening simultaneously.

3.3.6 ZrO_2 nanocoating stability in sodium chloride solution

Finally, the ZrO_2 nanocoatings, generated by DC and EAD methods, were evaluated by potentiodynamic polarization curves and EIS, after 30 min of immersion in NaCl 0.05 M for E_{ocp} stabilization (**Figure 3.3.14**). As can be seen, AA1100 exhibits a passivation behaviour corresponding to a contribution of a pseudo-stable interface layer in all substrates, with the exception of surfaces degreased with alkaline solution. This bare sample results in more active cathodic and anodic regions due to the growth of highly higroscopic and porous compounds, like AlOOH or $Al(OH)_3$ hydroxide compositions (**Figure 3.3.14a**), as evidenced by XPS (section 3.3.2). The measured corrosion current densities (j_{corr}), corrosion potentials (E_{corr}) and breakdown potentials (E_b) for the AA1100 curves are shown in **Table 3.3.4**.

All samples, with the exception of the bare one, display more positive breakdown potentials (E_b) respect to E_{corr}. Conversely, AA2024 surfaces show the behavior of active corrosion, even though both the cathodic and the anodic polarization current densities decrease with respect to pure Al surfaces (**Figure 3.3.14b**). The less negative E_{corr} in open circuit potential, which is observed for AA2024 samples with ZrO_2 nanocoating, and the

less oxigen reduction (cathodic curves) are benefitial for this substrate compared to AA1100/ZrO_2. Altogether allow us to conclude that ZrO_2 layer is more compact on AA2024 than on AA1100, which is in accordance to the SEM and AFM results, as noted earlier.

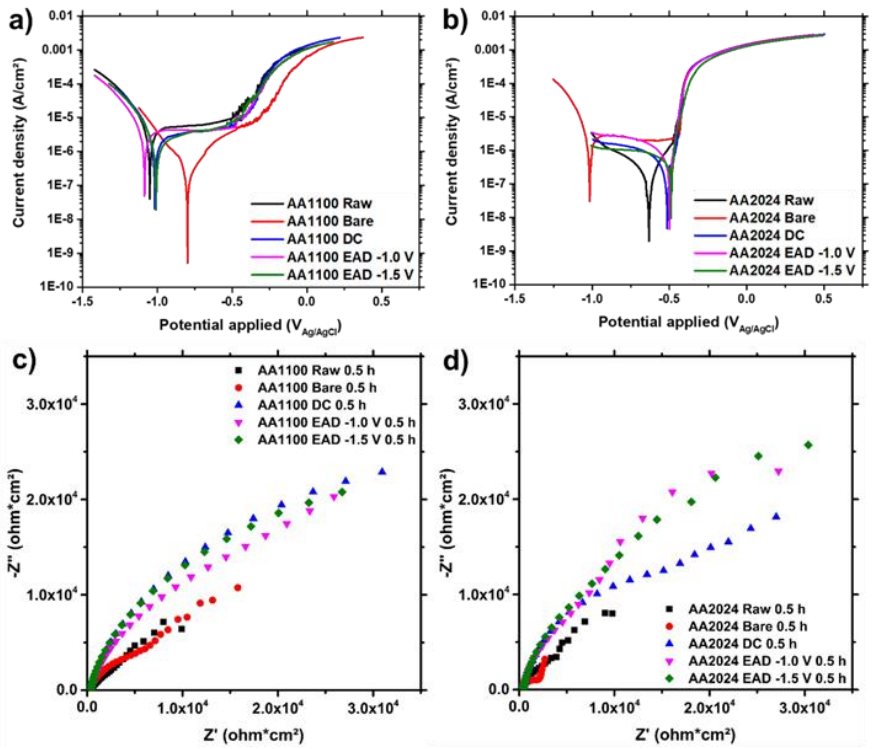

Figure 3.3.14. a-b) Polarization curves and **c-d)** Nyquist plots of AA1100 (**a**, **c**) and AA2024 (**b**, **d**) specimens after 30 min of immersion in aqueous NaCl 0.05 M electrolyte.

Moreover, the AA2024 surface in bare samples (**Figure 3.3.14b**) probably has a positive barrier contribution of CuO, Cu_2O and $Cu(OH)_2$ species, which are much more stable than Al hydroxides in similar potential and pH ranges (Pourbaix diagrams). However, the E_{corr} is too low (−0.82 V) and close to the standard reduction potential of pure Al (−0.76 V). After DC and EAD ZrO_2 depositions, the E_{corr} moves to positive values and j_{corr} values are the lowest ones (10^{-7} A/cm²).

Analyzing the DC and EAD methods for the ZrO_2 conversion nanocoating deposition on AA1100 and AA2024 substrates, the E_{corr} and

the j_{corr} are very similar for short exposition time. A detailed inspection of the effect of the the lowest cathodic potential (−1.5 V), in the coating generation compared to the highest potential (−1.0 V), proves that they also have similar electrochemical behaviour. Therefore, we conclude that the differences on the potential applied do not affect the barrier protection of the film, whereas it is mostly influenced by the substrate nature and the pre-treatments applied.

Table 3.3.4. Corrosion potentials (E_{corr}) and corrosion current densities (j_{corr}) measured by Tafel fitting of the experimental curves obtained after samples immersion in NaCl 0.05M for 30 min.

Sample code	E_{corr} (V) (Value ± *SD*)	j_{corr} (A/cm²) (Value ± *SD*)	E_b (V) (Value ± *SD*)
AA1100 Raw	− 0.923 *(± 0.200)*	3.35E−6 *(± 2.48E−6)*	− 0.495 *(± 0,024)*
AA1100 Bare	− 0.851 *(± 0.055)*	7.23E−7 *(± 3.41E−7)*	-
AA1100 DC	− 0.997 *(± 0.012)*	2.91E−6 *(± 4.17E−7)*	− 0.492 *(± 0.017)*
AA1100 EAD − 1.0 V	− 1.089 *(± 0.031)*	5.56E−6 *(± 2.11E−6)*	− 0.461 *(± 0.017)*
AA1100 EAD − 1.5 V	− 0.995 *(± 0.009)*	2.59E−6 *(± 2.11E−7)*	− 0.457 *(± 0.074)*
AA2024 Raw	− 0.576 *(± 0.045)*	4.52E−7 *(± 2.59E−7)*	-
AA2024 Bare	− 0.802 *(± 0.268)*	1.57E−6 *(± 9.21E−7)*	-
AA2024 DC	− 0.517 *(± 0.033)*	8.13E−7 *(± 2.94E−7)*	-
AA2024 EAD − 1.0 V	− 0.575 *(± 0.145)*	9.77E−7 *(± 7.39E−7)*	-
AA2024 EAD − 1.5 V	− 0.518 *(± 0.042)*	7.68E−7 *(± 4.00E−7)*	-

The corrosion resistance on Al substrates is better evaluated by measurements of polarization resistances (R_p) by EIS analysis, and these measurements are shown in **Table 3.3.5**.

The higher the polarization resistance (*i.e.*, the larger the Nyquist plot diameter, **Figure 3.3.14c-d**), the greater the barrier effect of the coating. The highest R_p values were found for substrates covered with the ZrO_2 nanocoating. **Table 3.3.5** indicates that the data for such samples were one

order of magnitude higher than for Raw and Bare samples, for both AA1100 and AA2024 aluminium alloys. The resistance behaviour of ZrO_2 generated by DC and EAD methods was similar on AA1100 plates (**Figure 3.3.14c**), whereas on AA2024 the first denoted the beginning of a second time constant, probably associated to a electrolyte diffusion at low frequencies (**Figure 3.3.14d**).

Table 3.3.5. Electrochemical impedance parameters for all samples, after immersion in NaCl 0.5M for 30 min.[a)]

Sample code	R_s ($\Omega \cdot cm^2$)	R_p ($\Omega \cdot cm^2$)	CPE_{dl} ($F \cdot cm^{-2} \cdot s^{n-1}$)	n_{CPE}
AA1100 Raw	349.3	6.2×10^3	3.7×10^{-5}	0.695
AA1100 Bare	348.6	9.9×10^3	1.9×10^{-5}	0.798
AA1100 DC	220.4	7.0×10^4	2.1×10^{-5}	0.792
AA1100 EAD – 1.0 V	288.1	4.0×10^4	2.4×10^{-5}	0.779
AA1100 EAD – 1.5 V	235.3	5.4×10^4	2.9×10^{-5}	0.781
AA2024 Raw	388.8	5.6×10^3	3.9×10^{-5}	0.896
AA2024 Bare	363.0	2.3×10^3	5.7×10^{-5}	0.868
AA2024 DC	383.2	2.9×10^4	1.4×10^{-5}	0.855
AA2024 EAD – 1.0 V	394.5	2.7×10^4	2.7×10^{-5}	0.890
AA2024 EAD – 1.5 V	408.8	5.3×10^4	1.8×10^{-5}	0.851

Note: [a)] The data were fitted using an electrical equivalent circuit (EEC) composed by one time constant $R_s(R_pCPE_{dl})$, where R_s represents the ohmic resistance between the working and the reference electrodes, R_p is the polarization resistance and CPE_{dl} corresponds to the constant phase element of the double-layer capacitance.

The capacitance of the double layer, measured as a constant phase element (CPE), was invariable. This is generally attributed to the surface reactivity, surface heterogeneity, and surface roughness regarding to current and potential distribution. Therefore, the Al-rich interface established in **Figure 3.3.3e** proves to be thin and homogenous in all samples.

The presence of low content of copper is known to be beneficial for the formation of Zr-based conversion coatings on aluminium alloys due to the difference of potential observed between the aluminium matrix and the Cu-rich intermetallic boundaries.[24,35,55,56] Polarization results after DC and EAD ZrO_2 conversion pre-treatments in pure copper plates are presented in **Figure 3.3.15**. As can be seen, aparently none passivation layers were obtained in any of the treatments applied (**Figure 3.3.15b**). It proves that the effect of Cu elements in AA2024 surfaces is due to its cathodic nature respect to the Al main matrix.

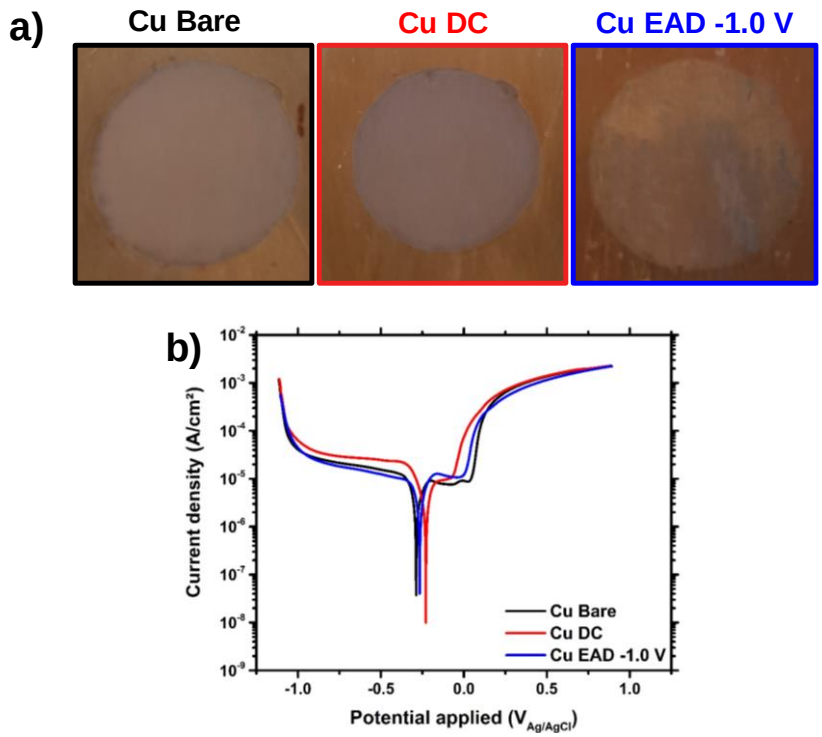

Figure 3.3.15. Electrochemical and visual inspection of the tested pure copper: **a)** photographs of the analyzed areas after polarization assays, and **b)** potentiodynamic polarization curves in NaCl 0.05 M electrolyte (0.5 h).

These observations reinforce the understanding that the utilization of DC and EAD techniques in H_2ZrF_6 aqueous solution enables the deposition of the zirconium conversion coating in specific substrates, like those showed in this study for AA1100, AA2024 and ITO, whereas are

prevented in others, like pure copper. Moreover, the electrochemical results evidence that such nanometric coatings do not represent a real protection barrier but rather a intermediate layer for further multilayer coatings depositions.[26]

3.4 *Conclusions*

In this work, the control over the zirconium conversion nanocoating deposition on aluminum substrates was successfully achieved by the application of chemisorption (DC) and electro-assisted deposition (EAD technique). The novelty of the research relies on the absence of any co-additive in the hexafluorozirconic acid aqueous solution, which represents a great advantage with respect to other bath solutions previously investigated.

The ZrO_2 nanocoating generated by EAD or DC methods completely covers both the aluminum matrix and the intermetallic particles. One of the advantages of the electro-assisted method is the adequate control over the deposition parameters. The presence of copper alloying elements on AA2024 surface has also been proved to play an important role, favoring the ZrO_2 deposition in this aluminum alloy and showing that the EAD method occurs simultaneously with the adsorption chemical conversion reactions.

Furthermore, the deposition of the Zr conversion coating on conductive ITO substrates can be obtained exclusively by EAD, proving that it has potential application to be explored in other conductive substrates for which the conventional DC method is prevented.

Therefore, the results obtained in this study drive forces towards the use of ZrO_2 nanocoating as an electrochemically stable layer for future primer deposition in similar multicoated systems, like that employed with phosphate processes at industry.

3.5 *References*

(1) Streitberger, H.-J.; Goldschmidt, A. *BASF Handbook Basics of Coating Technology*, 3rd Ed.; Streitberger, H.-J., Goldschmidt, A., Eds.; European Coatings: Munster, 2018.

(2) Schütze, M.; Wieser, D.; Bender, B. *Corrosion Resistance of Aluminium and Aluminium Alloys*; Schütze, M., Wieser, D., Bender, B., Eds.; John Wiley & Sons, Ltd: Frankfurt, 2010.

(3) Narayanan, T. S. N. S. Surface Pretreatment by Phosphate Conversion Coatings - A Review. *Rev. Adv. Mater. Sci.* **2005**, *9* (2), 130–177.

(4) Freeman, D. B. *Phosphating and Metal Pre-Treatment : A Guide to Modern Processes and Practice*; Freeman, D. B., Ed.; Industrial Press: Michigan, 1986.

(5) Sander, J.; Kirmaier, L.; Manea, M.; Shchukin, D.; Skorb, E. *Anticorrosive Coatings : Fundamentals and New Concepts*; Sander, J., Kirmaier, L., Manea, M., Shchukin, D., Skorb, E., Eds.; Vincentz Network: Hanover, 2010.

(6) Nicole, L.; Laberty-Robert, C.; Rozes, L.; Sanchez, C. Hybrid Materials Science: A Promised Land for the Integrative Design of Multifunctional Materials. *Nanoscale* **2014**, *6* (12), 6267–6292. https://doi.org/10.1039/c4nr01788a.

(7) Kim, M. M.; Kapun, B.; Tiringer, U.; Šekularac, G.; Milošev, I. Protection of Aluminum Alloy 3003 in Sodium Chloride and Simulated Acid Rain Solutions by Commercial Conversion Coatings Containing Zr and Cr. *Coatings* **2019**, *9* (9). https://doi.org/10.3390/coatings9090563.

(8) Milošev, I.; Frankel, G. S. Conversion Coatings Based on Zirconium and/or Titanium. *J. Electrochem. Soc.* **2018**, *165* (3), C127–C144. https://doi.org/10.1149/2.0371803jes.

(9) Zhang, H.; Zhang, X.; Zhao, X.; Tang, Y.; Zuo, Y. Preparation of Ti-Zr-Based Conversion Coating on 5052 Aluminum Alloy, and Its Corrosion Resistance and Antifouling Performance. *Coatings* **2018**, *8* (11). https://doi.org/10.3390/COATINGS8110397.

(10) Eivaz Mohammadloo, H.; Sarabi, A. A.; Asemani, H. R.; Ahmadi, P. A Comparative Study of Eco-Friendly Hybrid Thin Films: With and without Organic Coating Application. *Prog. Org. Coatings* **2018**, *125*, 432–442. https://doi.org/10.1016/j.porgcoat.2018.09.023.

(11) Cardoso, H. R. P.; Rapacki, C.; Ferreira, J. Z. Monitoring of a Zr-Based Conversion Coating on Galvanised Steel and Its Performance against Corrosion. *Corros. Eng. Sci. Technol.* **2019**, *54* (8), 726–730. https://doi.org/10.1080/1478422X.2019.1657703.

(12) Liu, X.; Vonk, D.; Jiang, H.; Kisslinger, K.; Tong, X.; Ge, M.; Nazaretski, E.; Ravel, B.; Foster, K.; Petrash, S.; et al. Environmentally Friendly Zr-Based Conversion Nanocoatings for Corrosion Inhibition of Metal Surfaces Evaluated by Multimodal X-Ray Analysis. *ACS Appl. Nano Mater.* **2019**, *2* (4), 1920–1929. https://doi.org/10.1021/acsanm.8b02309.

(13) Han, J.; Thierry, D.; Ogle, K. Zr-Based Conversion Coating on Zn and Zn-Al-Mg Alloy Coating: Understanding the Accelerating Effect of Cu(II) and NO3−. *Surf. Coat. Technol.* **2020**. https://doi.org/doi.org/10.1016/

j.surfcoat.2020.126236.

(14) Ogle, K.; Buchheit, R. G. Conversion Coatings. In *Encyclopedia of Electrochemistry*; Wiley-VCH Verlag GmbH & Co. KGaA, 2007; pp 460–499. https://doi.org/10.1002/9783527610426.bard040503.

(15) Ramanathan, E.; Balasubramanian, S. Comparative Study on Polyester Epoxy Powder Coat and Amide Cured Epoxy Liquid Paint over Nano-Zirconia Treated Mild Steel. *Prog. Org. Coatings* **2016**, *93*, 68–76. https://doi.org/10.1016/j.porgcoat.2016.01.007.

(16) Cerezo, J.; Vandendael, I.; Posner, R.; Lill, K.; de Wit, J. H. W.; Mol, J. M. C.; Terryn, H. Initiation and Growth of Modified Zr-Based Conversion Coatings on Multi-Metal Surfaces. *Surf. Coatings Technol.* **2013**, *236*, 284–289. https://doi.org/10.1016/j.surfcoat.2013.09.059.

(17) Giacomelli, F. C.; Giacomelli, C.; De Oliveira, A. G.; Spinelli, A. Effect of Electrolytic ZrO2 Coatings on the Breakdown Potential of NiTi Wires Used as Endovascular Implants. *Mater. Lett.* **2005**, *59* (7), 754–758. https://doi.org/10.1016/j.matlet.2004.11.015.

(18) Dong, X.; Argekar, S.; Wang, P.; Schaefer, D. W. In Situ Evolution of Trivalent Chromium Process Passive Film on Al in a Corrosive Aqueous Environment. *ACS Appl. Mater. Interfaces* **2011**, *3* (11), 4206–4214. https://doi.org/sw.

(19) Moreira, V. B.; Ferreira, J. Z.; Meneguzzi, A. Pré-Tratamento Por Deposição Eletroassistida de Viniltrietoxissilano (VTES) Para a Pintura de Alumínio. *Tecnol. em Metal. Mater. e Mineração* **2018**, *15* (1), 68–74. https://doi.org/10.4322/2176-1523.1329.

(20) Moreira, V. B.; Cardoso, H. R. P.; Ferreira, J. Z.; Meneguzzi, Á. DEPOSIÇÃO ELETROASSISTIDA DE ORTOSSILICATO DE TETRAETILA (TEOS) COMO PRÉ-TRATAMENTO PARA A PINTURA DE ALUMÍNIO AA1100. *Tecnol. em Metal. Mater. e Mineração* **2018**, *15* (1), 56–62. https://doi.org/10.4322/2176-1523.1323.

(21) Li, L.; Swain, G. M. Effects of Aging Temperature and Time on the Corrosion Protection Provided by Trivalent Chromium Process Coatings on AA2024-T3. *ACS Appl. Mater. Interfaces* **2013**, *5* (16), 7923–7930. https://doi.org/10.1021/am4020023.

(22) Oliver, W. C.; Pharr, G. M. Measurement of Hardness and Elastic Modulus by Instrumented Indentation: Advances in Understanding and Refinements to Methodology. *J. Mater. Res.* **2004**, *19* (1), 3–20. https://doi.org/10.1557/jmr.2004.19.1.3.

(23) Roa, J. J.; Jiménez-Piqué, E.; Anglada, M. J. Nanoindentation of Advanced Ceramics: Applications to ZrO2 Materials. In *Applied nanoindentation in advanced materials*; Tiwari, A., Natarajan, S., Eds.; John Wiley & Sons, Ltd, 2017; pp 459–480.

(24) Sarfraz, A.; Posner, R.; Lange, M. M.; Lill, K.; Erbe, A. Role of Intermetallics

and Copper in the Deposition of ZrO 2 Conversion Coatings on AA6014. *J. Electrochem. Soc.* **2014**, *161* (12), C509–C516. https://doi.org/10.1149/2.0121412jes.

(25) Gusmano, G.; Montesperelli, G.; Rapone, M.; Padeletti, G.; Cusmà, A.; Kaciulis, S.; Mezzi, A.; Maggio, R. Di. Zirconia Primers for Corrosion Resistant Coatings. *Surf. Coatings Technol.* **2007**, *201* (12), 5822–5828. https://doi.org/10.1016/j.surfcoat.2006.10.036.

(26) Andreatta, F.; Paussa, L.; Lanzutti, A.; Rosero Navarro, N. C.; Aparicio, M.; Castro, Y.; Duran, A.; Ondratschek, D.; Fedrizzi, L. Development and Industrial Scale-up of ZrO2 Coatings and Hybrid Organic–Inorganic Coatings Used as Pre-Treatments before Painting Aluminium Alloys. *Prog. Org. Coatings* **2011**, *72* (1–2), 3–14. https://doi.org/10.1016/j.porgcoat.2011.01.011.

(27) Liu, X.; Vonk, D.; Jiang, H.; Kisslinger, K.; Tong, X.; Ge, M.; Nazaretski, E.; Ravel, B.; Foster, K.; Petrash, S.; et al. Environmentally Friendly Zr-Based Conversion Nanocoatings for Corrosion Inhibition of Metal Surfaces Evaluated by Multimodal X-Ray Analysis. *ACS Appl. Nano Mater.* **2019**, *2* (4), 1920–1929. https://doi.org/10.1021/acsanm.8b02309.

(28) Gaillard, Y.; Anglada, M.; Jiménez-Piqué, E. Nanoindentation of Yttria-Doped Zirconia: Effect of Crystallographic Structure on Deformation Mechanisms. *J. Mater. Res.* **2009**, *24* (3), 719–727. https://doi.org/10.1557/jmr.2009.0091.

(29) Jiménez-Piqué, E.; González-García, L.; Rico, V. J.; González-Elipe, A. R. Nanoindentation of Nanocolumnar TiO2 Thin Films with Single and Stacked Zig-Zag Layers. *Thin Solid Films* **2014**, *550*, 444–449. https://doi.org/10.1016/j.tsf.2013.10.022.

(30) Gaillard, Y.; Rico, V. J.; Jiménez-Piqué, E.; González-Elipe, A. R. Nanoindentation of TiO2 Thin Films with Different Microstructures. *J. Phys. D Appl. Phys.* **2009**, *42*, 145305.

(31) Kassavetis, S.; Logothetidis, S.; Zyganitidis, I. Nanomechanical Testing of the Barrier Thin Film Adhesion to a Flexible Polymer Substrate. *J. Adhes. Sci. Technol.* **2012**, *26* (20–21), 2393–2404. https://doi.org/10.1163/156856111X599526.

(32) Fockaert, L. I.; Taheri, P.; Abrahami, S. T.; Boelen, B.; Terryn, H.; Mol, J. M. C. Zirconium-Based Conversion Film Formation on Zinc, Aluminium and Magnesium Oxides and Their Interactions with Functionalized Molecules. *Appl. Surf. Sci.* **2017**, *423*, 817–828. https://doi.org/10.1016/j.apsusc.2017.06.174.

(33) Šekularac, G.; Kovač, J.; Milošev, I. Comparison of the Electrochemical Behaviour and Self-Sealing of Zirconium Conversion Coatings Applied on Aluminium Alloys of Series 1xxx to 7xxx. *J. Electrochem. Soc.* **2020**, *167* (11), 111506. https://doi.org/10.1149/1945-7111/aba875.

(34) George, F. O.; Skeldon, P.; Thompson, G. E. Formation of Zirconium-Based Conversion Coatings on Aluminium and Al–Cu Alloys. *Corros. Sci.* **2012**, *65*, 231–237. https://doi.org/10.1016/j.corsci.2012.08.031.

(35) Cerezo, J.; Vandendael, I.; Posner, R.; de Wit, J. H. W.; Mol, J. M. C.; Terryn, H. The Effect of Surface Pre-Conditioning Treatments on the Local Composition of Zr-Based Conversion Coatings Formed on Aluminium Alloys. *Appl. Surf. Sci.* **2016**, *366*, 339–347. https://doi.org/10.1016/j.apsusc.2016.01.106.

(36) Torras, J.; Azambuja, D. S.; Wolf, J. M.; Alemán, C.; Armelin, E. How Organophosphonic Acid Promotes Silane Deposition onto Aluminum Surface: A Detailed Investigation on Adsorption Mechanism. *J. Phys. Chem. C* **2014**, *118* (31), 17724–17736. https://doi.org/10.1021/jp5046707.

(37) Cerezo, J.; Taheri, P.; Vandendael, I.; Posner, R.; Lill, K.; de Wit, J. H. W.; Mol, J. M. C.; Terryn, H. Influence of Surface Hydroxyls on the Formation of Zr-Based Conversion Coatings on AA6014 Aluminum Alloy. *Surf. Coatings Technol.* **2014**, *254*, 277–283. https://doi.org/10.1016/j.surfcoat.2014.06.030.

(38) Buchheit, R. G.; Martinez, M. A.; Montes, L. P. Evidence for Cu Ion Formation by Dissolution and Dealloying the Al2CuMg Intermetallic Compound in Rotating Ring-Disk Collection Experiments. *J. Electrochem. Soc.* **2000**, *147* (1), 119. https://doi.org/10.1149/1.1393164.

(39) Vukmirovic, M. B.; Dimitrov, N.; Sieradzki, K. Dealloying and Corrosion of Al Alloy 2024-T3. *J. Electrochem. Soc.* **2002**, *149* (9), B428. https://doi.org/10.1149/1.1498258.

(40) Hashimoto, T.; Zhang, X.; Zhou, X.; Skeldon, P.; Haigh, S. J.; Thompson, G. E. Investigation of Dealloying of S Phase (Al2CuMg) in AA 2024-T3 Aluminium Alloy Using High Resolution 2D and 3D Electron Imaging. *Corros. Sci.* **2016**, *103*, 157–164. https://doi.org/10.1016/j.corsci.2015.11.013.

(41) Zhang, X.; Hashimoto, T.; Lindsay, J.; Zhou, X. Investigation of the De-Alloying Behaviour of θ-Phase (Al2Cu) in AA2024-T351 Aluminium Alloy. *Corros. Sci.* **2016**, *108*, 85–93. https://doi.org/10.1016/j.corsci.2016.03.003.

(42) Šekularac, G.; Kovač, J.; Milošev, I. Prolonged Protection, by Zirconium Conversion Coatings, of AlSi7Mg0.3 Aluminium Alloy in Chloride Solution. *Corros. Sci.* **2020**, *169*, 108615. https://doi.org/10.1016/j.corsci.2020.108615.

(43) Lostak, T.; Krebs, S.; Maljusch, A.; Gothe, T.; Giza, M.; Kimpel, M.; Flock, J.; Schulz, S. Formation and Characterization of Fe3+-/Cu2+-Modified Zirconium Oxide Conversion Layers on Zinc Alloy Coated Steel Sheets. *Electrochim. Acta* **2013**, *112*, 14–23. https://doi.org/10.1016/j.electacta.2013.08.161.

(44) Yen, S. .; Guo, M. .; Zan, H. . Characterization of Electrolytic ZrO2 Coating on Co–Cr–Mo Implant Alloys of Hip Prosthesis. *Biomaterials* **2001**, *22* (2), 125–133. https://doi.org/10.1016/S0142-9612(00)00133-2.

(45) Eivaz Mohammadloo, H.; Sarabi, A. A.; Sabbagh Alvani, A. A.; Sameie, H.; Salimi, R. Nano-Ceramic Hexafluorozirconic Acid Based Conversion Thin Film: Surface Characterization and Electrochemical Study. *Surf. Coatings Technol.* **2012**, *206* (19–20), 4132–4139. https://doi.org/10.1016/j.surfcoat.2012.04.009.

(46) Zhang, F.; Jacobi, A. M. Aluminum Surface Wettability Changes by Pool Boiling of Nanofluids. *Colloids Surfaces A Physicochem. Eng. Asp.* **2016**, *506*, 438–444. https://doi.org/10.1016/j.colsurfa.2016.07.026.

(47) Gonzalez-Canche, N. G.; Flores-Johnson, E. A.; Cortes, P.; Carrillo, J. G. Evaluation of Surface Treatments on 5052-H32 Aluminum Alloy for Enhancing the Interfacial Adhesion of Thermoplastic-Based Fiber Metal Laminates. *Int. J. Adhes. Adhes.* **2018**, *82* (December 2017), 90–99. https://doi.org/10.1016/j.ijadhadh.2018.01.003.

(48) Mrad, M.; Ben Amor, Y.; Dhouibi, L.; Montemor, M. F. Effect of AA2024-T3 Surface Pretreatment on the Physicochemical Properties and the Anticorrosion Performance of Poly(γ-Glycidoxypropyltrimethoxysilane) Sol-Gel Coating. *Surf. Interface Anal.* **2018**, *50* (3), 335–345. https://doi.org/10.1002/sia.6373.

(49) Doerre, M.; Hibbitts, L.; Patrick, G.; Akafuah, N. Advances in Automotive Conversion Coatings during Pretreatment of the Body Structure: A Review. *Coatings* **2018**, *8* (11), 405. https://doi.org/10.3390/coatings8110405.

(50) Li, L.; Desouza, A. L.; Swain, G. M. In Situ PH Measurement during the Formation of Conversion Coatings on an Aluminum Alloy (AA2024). *Analyst* **2013**, *138* (15), 4398. https://doi.org/10.1039/c3an00663h.

(51) Parvizi, R.; Marceau, R. K. W.; Hughes, A. E.; Tan, M. Y.; Forsyth, M. Atom Probe Tomography Study of the Nanoscale Heterostructure around an Al20Mn3Cu2 Dispersoid in Aluminum Alloy 2024. *Langmuir* **2014**, *30* (49), 14817–14823. https://doi.org/10.1021/la503418u.

(52) Li, L.; Whitman, B. W.; Swain, G. M. Characterization and Performance of a Zr/Ti Pretreatment Conversion Coating on AA2024-T3. *J. Electrochem. Soc.* **2015**, *162* (6), C279–C284. https://doi.org/10.1149/2.0901506jes.

(53) Shruthi, T. K.; Swain, G. M. Communication—Role of Trivalent Chromium on the Anti-Corrosion Properties of a TCP Conversion Coating on Aluminum Alloy 2024-T3. *J. Electrochem. Soc.* **2018**, *165* (2), C103–C105. https://doi.org/10.1149/2.1301802jes.

(54) Dong, X.; Wang, P.; Argekar, S.; Schaefer, D. W. Structure and Composition of Trivalent Chromium Process (TCP) Films on Al Alloy. *Langmuir* **2010**, *26* (13), 10833–10841. https://doi.org/10.1021/la100699u.

(55) Adhikari, S.; Unocic, K. A.; Zhai, Y.; Frankel, G. S.; Zimmerman, J.; Fristad, W. Hexafluorozirconic Acid Based Surface Pretreatments: Characterization and Performance Assessment. *Electrochim. Acta* **2011**, *56* (4), 1912–1924. https://doi.org/10.1016/j.electacta.2010.07.037.

(56) Van Ingelgem, Y.; Hubin, A.; Vereecken, J. Investigation of the First Stages of the Localized Corrosion of Pure Copper Combining EIS, FE-SEM and FE-AES. *Electrochim. Acta* **2007**, *52* (27 SPEC. ISS.), 7642–7650. https://doi.org/10.1016/j.electacta.2006.12.039.

4 Aluminum protection by using green zirconium oxide layer and organic coating: An efficient and adherent dual system

SUMMARY

In this chapter, the use of ZrO_2 nanocoating in aluminum substrates, generated by controlled electrochemical chronoamperometry in hexafluorozirconic acid solutions, resulted in less porous films than that obtained by chemical conversion coating. After the application of an epoxy coating, long-term cyclic immersion corrosion tests and scratch tests proved the superior protection of the dual system and the coating lifespan, thanks to the enhanced adhesion of ZrO_2 intermediate layer and the organic coating. As zirconium-based electrolytes are considered more friendly baths if compared to that of other conversion coating processes, like chromating, phosphating or anodizing processes, this study opens new insights to the protection of structural metals in sectors such as automotive, naval and aerospace industries. The main advantages are the employment of lightweight intermediate pre-treatment (nanoscale), compared to conventional ones (microscale), and reduction of waste slurry (electrolyte bath free of additives).

Publication derived from this work:

Moreira, V. B.; Meneguzzi, A.; Jiménez-Piqué, E.; Alemán, C. and Armelin, E. Green Nanocoatings Based on the Deposition of Zirconium Oxide: The Role of the Substrate. *Sustainability* **2021**, *13*, 9688. https://doi.org/10.3390/su13179688

4.1 *Introduction*

The painting processes start with careful cleaning and pre-treatment of the substrate. Currently, in the technology for body car painting, common pre-treatment involves phosphating process, where the body-in-white of the vehicle is cleaned and coated with phosphate solution. The most important function of phosphate conversion coating is the adhesion promotion between galvanized body car structure and the cathodic electrodeposition primer (commonly known by KTL coating). Tricationic phosphating renders a basic level of corrosion protection and, usually, the thickness of the conversion coating is optimized by adding oxidants like molybdate, chlorate, organic nitro compounds, among other accelerators, in the phosphate bath.[1] Altogether result in an increase of sludge with hazardous contaminants for water effluents and elevated costs for waste recovery.[2] By other hand, since the implementation of REACH regulation in 2006,[3] chromate-based coating processes have been eliminated as chemical passivation pretreatment in galvanized structures due to their technically proven hazardous to human health and environment.[4] Fortunately, non-phosphated zirconium-based conversion coatings are emerging as a green alternative to this conventional technology and are being considered less aggressive to the environment if compared to chromate conversion coatings and phosphating processes.[5–7]

Nowadays, zirconium-based chemical conversion coatings (ZrCC) are the most studied pre-treatment for metal surface.[8–10] A ZrCC layer is usually formed by dip-coating of the metal substrates in aqueous hexafluorozirconic acid-based conversion solution (H_2ZrF_6).[6] The resulting films are typically very thin (< 100 nm)[11–14] and their composition depends on the solubility and transport of ions in the bath solution (bath agitation),[6] bath additives and pH, with zirconium oxides and hydroxides being the main components of the passivation layer. For instance, Zoppas and co-workers[15] tested the efficacy of ZrCC obtained by dip-coating deposition (DC), as a sealing agent for aluminum anodized substrates. The samples treated with H_2ZrF_6 showed higher corrosion resistance compared to the unsealed aluminum samples. They also applied the same strategy to galvanized steel substrates, proving that the ZrCC deposition is highly dependent on the solution

pH and on the reaction time.[16] Such pre-treatments have demonstrated to improve both the corrosion resistance and the adhesion of top coats and adhesives.[9,10,17–20] There are several metals that were approached, such as carbon and galvanized steel,[21–23] zinc,[24] magnesium[25] and aluminum surfaces.[13,26,27] All of them of utmost importance for the automotive and aircraft industry that strongly uses pre-treatment processes prior to structure protection by organic coatings.

Although good results are obtained with the dip-coating method of ZrCC, the zirconium electro-assisted deposition (Zr-EAD) technique has come into force thanks to the excellent control over the film homogeneity and compactness.[28] This procedure consists of promoting water electrolysis in the conversion bath, thus the cathodic half-reaction in acidic medium is the proton reduction reaction, leading to a pH shift on the cathode surface towards alkaline values.[29–35] In fact, the Zr-EAD deposition takes place simultaneously with the chemical conversion process driven by ions diffusion, as expressed in the previous thesis chapter. The films are usually amorphous, which is in agreement with previous reports of similar conversion coatings produced at room temperature,[31,32] and provide corrosion protection by increasing the breakdown potential of the passive layer.

This work investigates the corrosion protection properties of ZrO_2 nanocoating, electrochemically (Zr-EAD) and dip-coated (Zr-DC) deposited, on two types of aluminium substrates (pure and copper rich alloy), in order to understand the influence of the metal alloying elements in the ZrO_2 layer. Furthermore, the final applicability of such electro-assisted and chemically adsorbed zirconium oxide layer is act as an intermediate layer for long-term metal protection. Thus, an anticorrosive coating was also applied on the inorganic ZrCC layer and was investigated with cyclic accelerated corrosion test, by using NaCl 3.5 wt. % aqueous solution as corrosive medium; and with scratch hardness measurements for adhesion assessment.

4.2 *Materials and methods*

4.2.1 Materials

Hexafluorozirconic acid hydrated (H_2ZrF_6, 50 % wt. in water) was supplied by Sigma-Aldrich Co. (Madrid, Spain); sodium hydroxide (pellets) was purchased from Panreac S.A. (Castellar del Vallès, Spain) and alkaline degreaser Saloclean 667N was kindly supplied by Klintex Insumos Industriais Ltda. (Cachoeirinha, Brazil). AA1100 and AA2024 plates (5.0 × 1.4 × 0.3 cm^3) were used as substrates for Zr-DC and Zr-EAD formation in the morphological and electrochemical studies; whereas AA1100 plates (5.0 × 1.4 × 0.3 cm^3), and AA2024 disks (3.5 cm of diameter and 4 mm of thickness) were used in the accelerated corrosion tests, in order to have a large area of analysis. The composition analysis of aluminum substrates is provided. AA1100 is a commercially pure Al class (in wt. %): Cu (0.34); Fe (0.42); Si (0.19); Mn (<0.01); Ti (<0.02); Zn (<0.01) and balanced Al. The chemical composition was provided by the supplier (Irmãos Galeazi Ltda., Brazil). The AA2024-T3 is the structural reinforced Cu-rich grade with metallurgical temper code T3, which is referred to solution heat treated, cold worked and naturally aged. The AA2024 panel has chemical composition of (in wt. %): Cu (4.63); Mg (1.66); Mn (0.55); Fe (0.36); Si (0.31); and balanced to Al. The compositional analysis for this alloy was determined by ICP-AES (spectrometer SPECTROMAXx). Hempadur Primer 15304 (Codes: 15308 and 95040, for epoxy base and curing agent, respectively), commercialized by Hempel S.A. (Polinyà, Spain), was used as anticorrosive organic coating.

4.2.2 Preparation of aluminum substrates for the chemical and electrochemical deposition of ZrO_2

Prior the zirconium oxide deposition, the substrates were ground with silicon carbide paper from #600, down to grade #2500, to ensure similar roughness. Reproducible cleaned substrates were obtained by cleaning the surface, by one side, (i) in organic solvents and, by other, (ii) using chemical etching. The first consisted of dipping the samples in a vessel with isopropanol, followed by ethanol and, at last, acetone, at room temperature, with 5 min of time in each solvent, and

using an ultrasound bath. This procedure provides a mild cleaning, aiming for the preservation of the naturally formed aluminum oxide layer (hereafter coded as "Raw"). In the second method, the samples were thoroughly washed with water and acetone, and immersed in Saloclean 667N degreasing agent (pH 9.4, 70 g/L, 70 °C) for 5 min, washed with distilled water in a sonication bath for 5 min, dried under a hot air stream, and stored under vacuum before use (hereafter coded as "Bare"). The cleaning procedure can be visualized in the **Figure 4.2.1a**.

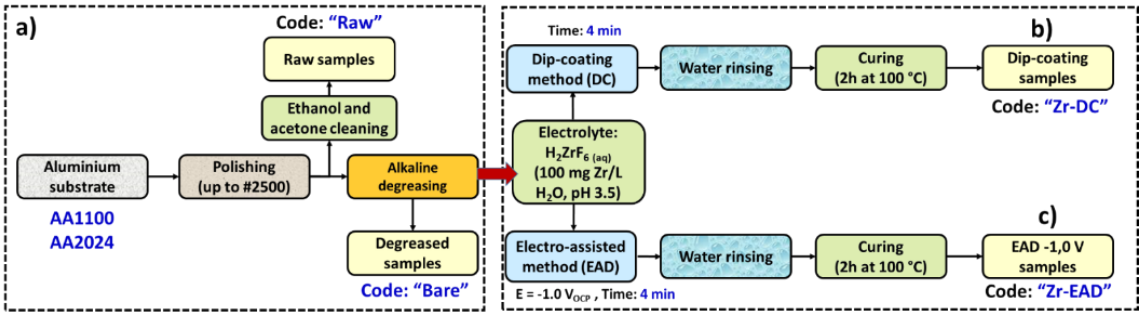

Figure 4.2.1. Flow chart for the whole processes in the preparation of the ZrO_2 nanocoating: **a)** substrate polishing and cleaning steps; **b)** dip-coating of aluminum substrates in H_2ZrF_6 aqueous solution; and **c)** EAD in H_2ZrF_6 electrolyte, by using Al plates or discs as substrates.

4.2.3 Zirconium chemical conversion coating deposition (Zr-DC)

The conversion bath consists of H_2ZrF_6 aqueous solution with 100 mg of Zr/L (0.015% *v*/*v*) in water. The pH was adjusted to 3.5 with a solution of NaOH 1M. In order to produce the ZrCC samples (hereafter coded as "DC", corresponding to dip-coating process), panels were immersed in the conversion solution for 4 min, followed by water rinsing and hot air stream drying before curing step for 2 h at 100 °C in a vacuum oven (**Figure 4.2.1b**).

4.2.4 Zirconium electro-assisted deposition (Zr-EAD)

The Zr-EAD samples were obtained by potentiostatic electrochemical method, using the same bath described before as an electrolyte. The experiments were carried out in an Autolab PGSTAT302N potentiostat-galvanostat (Metrohm, Herisau, Switzerland), by using three electrodes cell, where the substrate is the working electrode with a Ag|AgCl reference electrode (3M of KCl) and graphite

counter electrode. The electrolyte used in the cell is the same as used for the conversion solution. The samples were stabilized in open circuit potential (OCP) for short time (30 s) and subjected to the desired potential (− 1.0 V relative to the measured OCP) during 4 min. According to this procedure, the samples generated were named as "EAD". Samples coated by EAD method were further post-treated for 2 h at 100 °C, in a vacuum oven, to achieve a good compactness of oxide layer and reduction of defects (**Figure 4.2.1c**), i.e., the same post-treatment operated with DC samples (**Section 4.2.3**). The film topography and the cross-section thicknesses were measured by scanning electron microscopy (SEM), with a Focus Ion Beam (FIB) Zeiss Neon 40 instrument (Carl Zeiss, Oberkochen, Germany). The samples were previously coated with a sputtered carbon layer and received a thin protective layer of platinum (gas injection) before surface cutting. An electron beam of 5 kV was applied for cutting the cross-sections and the thickness of each sample was evaluated after 50 measurements, using high magnification images.

4.2.5 Electrochemical characterization of ZrCC samples

The experiments were performed in an Autolab PGSTAT302N potentiostat-galvanostat (Metrohm, Herisau, Switzerland) equipment. The electrochemical cell consisted of three electrodes, having the sample set as the working electrode, a platinum wire as counter electrode and a Ag|AgCl (KCl, 3M) as reference electrode. The tested area was 0.785 cm^2 and the electrolyte used in both potentiodynamic polarization and electrochemical impedance spectroscopy (EIS) tests was a NaCl aqueous solution (0.05 M). The curves were registered after 30 min of open circuit potential (OCP) stabilization.

In the potentiodynamic study (polarization tests), the potential sweep ranged from − 0.3 V_{OCP} to + 1.0 V_{OCP} with a scan rate of 1 mV/s. The run times for each experiment were: 24 h (1 day), 48 h (2 days), 96 h (5 days) and 168 h (7 days).

EIS experiments were also performed to evaluate the stability of the ZrO_2 nanocoating as a function of time exposure to the electrolyte solution. The amplitude of the EIS perturbation signal was 10 mV/peak, the frequency ranged from 10^5 to 10^{-1} Hz taking measurements of 10 frequencies per decade. The same run times as that used in the polarization tests were used. The Randles circuit

$[R_s \cdot (R_p \cdot CPE_{dl})]$ was applied to calculate the electrochemical parameters expressed in the Results and Discussion section (**Section 4.3**).

The coating porosity (*P*), after the metal bare pre-treatment with alkaline degreasing solution and after the formation of zirconium oxide coating, was evaluated following the procedure described by previous authors (**Equation 4.1**):[2,36,37]

$$P = \frac{R_p'}{R_p} \times 10^{-(\Delta E_{corr}/\beta_a)} \times 100 \quad \textbf{(4.1)}$$

Where R_p' and R_p are the polarization resistance of Raw and coated substrates, respectively; ΔE_{corr} is the corrosion potential difference between the Raw substrate and the coated substrates and β_a is the anodic Tafel coefficient of bare substrate obtained in the potentiodynamic anodic polarization study. Polarization resistance was calculated from parameters obtained with the Tafel extrapolation method, using Nova 2.1 software. Those parameters were taken after 24 h of immersion in NaCl 0.05 M, to ensure the OCP stabilization of aluminum substrates.

4.2.6 Organic coating deposition, accelerated corrosion tests and scratch resistance

The primer used as a second coating layer for the protection of AA1100 and AA2024 surfaces is a commercial polyamide cured anticorrosive epoxy primer of two-components, containing zinc phosphate as a corrosion inhibiting pigment. This primer is characterized by a high performance in protection against corrosion and the dry film paint has good mechanical properties. Therefore, the aim of this study is to verify the adherence properties of the samples electrochemically treated, i.e., with the ZrO_2 nanocoating generated by EAD method, compared to the degreased samples (Bare), under a long period of exposition in a corrosive medium.

The resin-hardener ratio (*v*/*v*) (Hempadur 15308 and curing agent 95040) used was 4/1, according to the manufacturer recommendations (Pinturas Hempel S.A., Polinyà, Spain). The mixture was prepared in a polyethylene reservoir at room temperature (25 °C) by stirring it for about 15 min. The specimens, properly

treated (**Section 4.2.2** and **Section 4.2.4**), were manually painted using a paint roller. Afterwards, all the painted specimens were allowed to cure for 7 days at room temperature in a fume hood. The edges and holes were additionally protected with impermeable polyester tapes (Polyester tape 8992, 3M Company, Madrid, Spain) to avoid corrosion. Once the paint was completely dried, thickness was measured by using Mega-Check Pocket (Neurtek S.A) meter. It was previously calibrated to non-ferrous basis by using the supplied gauges. The final dry film thickness (DFT) was 135 ± 27 μm. One single paint layer was applied in order to ensure reproducibility in the scratch hardness measurements.

Accelerated corrosion studies were carried out with both painted and non-painted samples. The test was performed using a patented equipment for cyclic test, developed at our laboratory.[38–40] The corrosion medium was an aqueous solution of NaCl (3.5 wt. %, pH = 6.6) stored in a glass container at room temperature. The operating cyclic conditions are described in previous works.[41,42] Before testing, the samples were scribed and photographed with a digital camera. The total exposure time was 90 days for the painted specimens and 3 days (72 h) for the non-painted ones. ASTM D1654 standard was employed to evaluate the scribed area on painted specimens and optical microscopy was used to observe the epoxy coating delamination from the specimen cross-section sides.

For the non-painted samples, a computational image analysis technique was used for quantifying the corroded areas during the test.[43] This analysis was carried out, with three repetitions, only with AA2024 substrates with Bare, DC and EAD treatments in order to have a direct comparison of the protection provided by such pretreatments. In the appendix A, the author's published work[43] was included for the thesis committee consultancy.

The scratch tests were carried out with a CSM Revetest Scratch Tester (Anton Paar GmbH) with a Rockwell C tip of 200 μm radius. The measurement was performed with samples used in the abovementioned cyclic immersion test in order to evaluate coating adhesion and scratch resistance over time. The length of the scratch was 4 mm and the applied load was linearly incremented up to a force

of 80 N. After the test, the specimens were visually inspected by optical microscopy (Dino-Lite AM3113T microscope, AnMo Electronics Corporation).

4.3 *Results and discussion*

4.3.1 The stability of ZrO_2 nanocoating comparing the DC and EAD deposition methods

It has been observed in a previous work that the potential applied for ZrO_2 electro-assisted deposition influences the dry film thickness of the passivation layer, i.e., more negative potentials result in thicker films, whereas long deposition times are detrimental for good barrier layer formation.[28,34] Moreover, it has been observed that the film growth is fast in the first ten minutes of deposition, as recently pointed out by Milosev and co-workers for several types of Al alloys.[17] Unfortunately, for longer periods, pores and defects usually appear on the film, hindering the oxide barrier protection properties. Based on such previous evidences, the ZrO_2 coatings were obtained after cathodic deposition at negative potential (− 1.0 V) and after a constant electrodeposition time of 4 min. The coating thickness was measured by cross-section scanning electron microscopy images and varied depending on the substrate (31.1 ± 8.2 nm and 18.7 ± 4.0 nm, for AA1100 and AA2024, respectively). **Figure 4.3.1** contains topography SEM images of the studied coatings and their cross-sections.

Those differences in the ZrO_2 coating thicknesses are associated to the presence of thick and stable Al_2O_3 and $Al(OH)_3$ passivation layers in AA1100 grade after treatment with alkaline solutions (dissolution of $Al(OH)_4^-$) and neutralization.[44] In AA2024 surfaces, the alkaline etching of Al surface prevents such thick structures in a certain way, due to the oxide/hydroxide enrichment with Cu compounds (dealloying process) in presence of basic solutions.[45,46] The detection of Al_2O_3/AlOOH and Cu_2O and $Cu(OH)_2$ compounds in AA1100 and AA2024, respectively, was already proved by XPS analysis in our previous study (**Chapter 3**).[28]

Comparing EAD controlled ZrO_2 film formation with the classical chemical conversion coating method, the coating thickness on the latter is only dependent

on ions diffusion. Therefore, it was slightly lower than that obtained from EAD method (24.9 ± 6.7 nm and 14.5 ± 4.1 nm, for AA1100 and AA2024, respectively). Additionally, topography SEM images evidenced that Zr-EAD process is able to cover the whole substrates with less apparent defects and less visible polishing marks than Zr-DC.

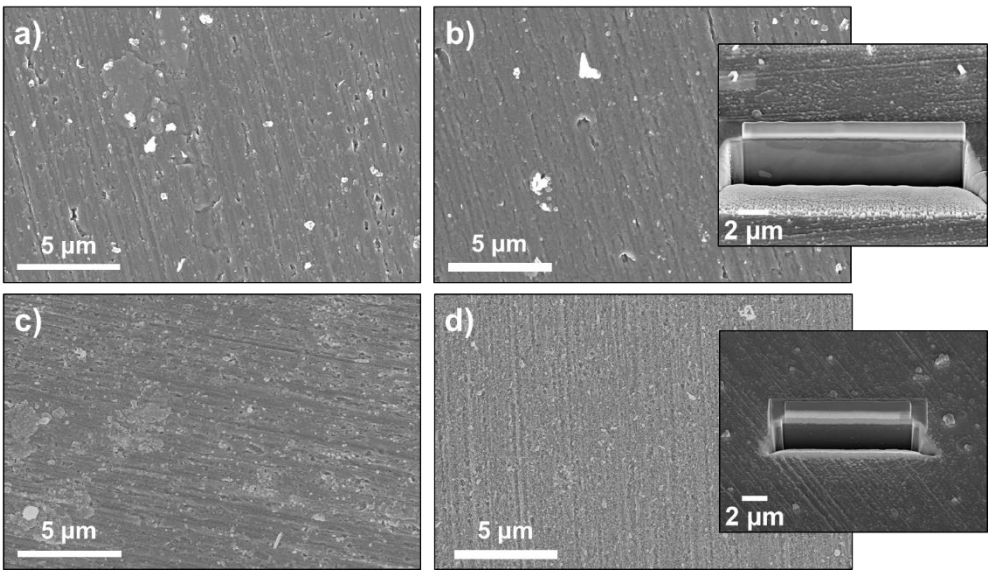

Figure 4.3.1. Topography SEM images of: **a)** AA1100/Zr-DC coating; **b)** AA1100/Zr-EAD coating; **c)** AA2024/Zr-DC coating; and **d)** AA2024/Zr-EAD coating. The insets on **b)** and **d)** images represent the cross-cut of those sample surfaces (by focused ion beam), used for the thicknesses measurements.

From polarization curves of AA1100 substrates with progressive immersion time it is possible to note a pseudo-passivation region in the potential range of − 1.0 V to 0 V (**Figure 4.3.2a**), with the exception of Bare sample (**Figure 4.3.2b**). In pure aluminum alloy, due to the absence of noble intermetallic particles, there is a lack of local galvanic couples and it shows an enhanced passivity,[17] which may be the reason for the more protective character of the non-coated specimens (Raw) observed in this alloy. Data obtained from the polarization curves shown in **Figure 4.3.2** using the Tafel extrapolation method are presented in **Table 4.3.1**.

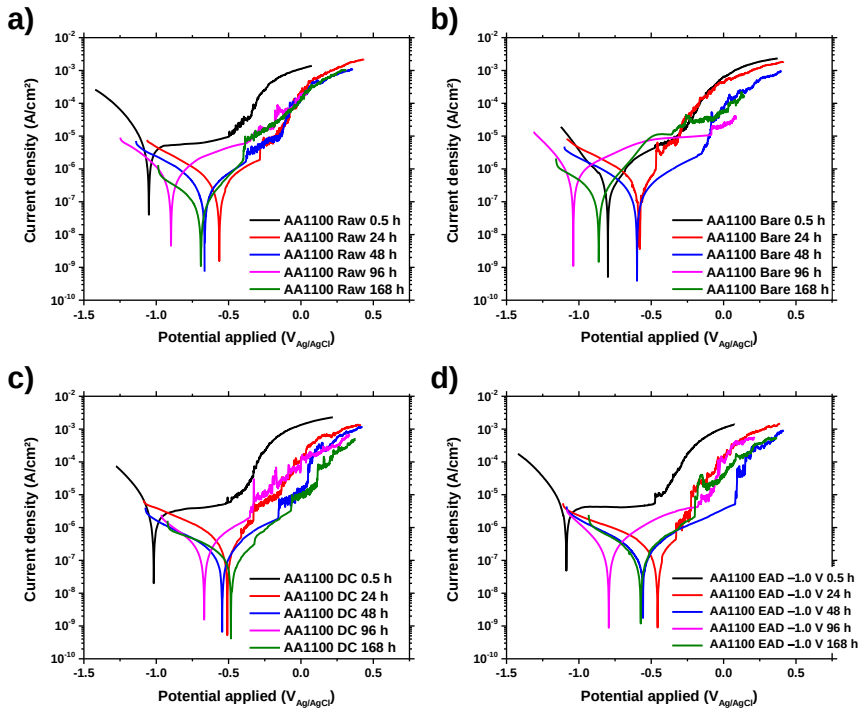

Figure 4.3.2. Polarization curves obtained for AA1100 specimens, throughout 168 h (7 days) of exposure in 0.05 M of NaCl solution, comparing the two methods used for the ZrO_2 metal deposition: **a)** Raw, **b)** Bare, **c)** Zr-DC method, and **d)** EAD method.

Although the corrosion potentials shift to high values in only 24 h, after 48 h of immersion, the pseudo-passivation layer found for Zr-EAD (**Figure 4.3.2d**) has higher breakdown potential (E_b) than that obtained for either Raw or DC samples (**Figure 4.3.2a**, **Figure 4.3.2c**, respectively, and **Table 4.3.1**), showing better stability of the zirconium nanocoating promoted by the EAD method if compared to the untreated metal and chemical conversion treatment. After 96 h and 168 h such stability has been decreased, proving the poor barrier protection of ZrO_2 nanocoatings, generated by either DC or EAD methods. The E_b is supposed to be related to the penetration of chlorine ions across the ZrO_2 nanolayer, causing the displacement of the breakdown potential to more negative values. It is more evident on Bare plates, in which the interfacial porous and hygroscopic structure of $Al/Al(OH)_3$ layer plays a detrimental barrier effect if compared to Raw, Zr-DC and Zr-EAD samples.

Table 4.3.1. Measured values of corrosion current density (j_{corr}), corrosion potential (E_{corr}) and breakdown potential (E_b) of AA1100 samples, during polarization tests with increased exposure time in 0.05 M NaCl solution.

Sample	Exposure time (h)	j_{corr} (A/cm²)	E_{corr} (V)	E_b (V)
AA1100 Raw	0.5	3.35×10^{-6}	− 0.923	− 0.495
	24	3.62×10^{-7}	− 0.564	− 0.283
	48	2.73×10^{-7}	− 0.665	− 0.380
	96	4.54×10^{-7}	− 0.898	− 0.353
	168	8.27×10^{-7}	− 0.691	− 0.397
AA1100 Bare	0.5	7.23×10^{-7}	− 0.851	-
	24	4.34×10^{-7}	− 0.585	-
	48	2.23×10^{-7}	− 0.598	− 0.152
	96	6.77×10^{-7}	− 1.039	− 0.084
	168	1.68×10^{-7}	− 0.862	-
AA1100 DC	0.5	2.91×10^{-6}	− 0.997	− 0.492
	24	3.53×10^{-7}	− 0.509	-
	48	1.59×10^{-7}	− 0.544	− 0.156
	96	2.13×10^{-7}	− 0.668	− 0.353
	168	9.08×10^{-8}	− 0.484	-
AA1100 EAD	0.5	5.56×10^{-6}	− 1.089	− 0.461
	24	1.58×10^{-7}	− 0.456	-
	48	1.80×10^{-7}	− 0.557	+0.080
	96	1.77×10^{-7}	− 0.793	− 0.175
	168	1.50×10^{-7}	− 0.573	− 0.201

Note: All data were obtained by Tafel extrapolation, using Nova 2.1 software.

Showing the effect of the surface treatment on another substrate, **Figure 4.3.3** contains the polarization curves observed with AA2024 metal in the same conditions as those of the AA1100 samples. The Tafel extrapolation data obtained from such analysis are shown in **Table 4.3.2**.

As opposed to the observed in AA1100 specimens, AA2024 substrates do not present any pseudo-passive behavior (**Figures 4.3.3a, c, d**), with exception of Bare sample at the initial immersion time (0.5 h, **Figure 4.3.3b**). Therefore, in this sample, the oxide/hydroxide Al layer is highly unstable and the anodic current increases sharply in only 24 h of sample exposition. From **Figure 4.3.3d** and **Table 4.3.2**, it is evident that AA2024 Zr-EAD specimens show lower anodic current density (j_{corr}), after 24 h of electrolyte immersion, if compared to the other specimens. This probably happens due to the better covering of intermetallic

particles (Al_2CuMg, Cu_3Mn_2Al and $Al_6(Cu,Fe,Mn)$, such as that reported by Birbilis et al.[47]), caused by the ZrO_2 compact nanolayer, generated by controlled voltage application. The Cu-rich Al alloy is highly corrosion prone in Cl^- ion environment due to the presence of such compounds.[48] Fortunately, after 48 h of immersion time, the system stabilizes and j_{corr} of Zr-EAD/AA2024 disc shifts to more negative values compared to Raw plates.

The j_{corr} values enhanced gradually with immersion time for all the other samples, including Zr-DC. After 96 h of immersion, the anodic current density obtained for Zr-EAD on AA2024 plates is approximately one third part of the one observed for DC. Therefore, we can conclude that the electrodeposition method produces films with better barrier properties over time.

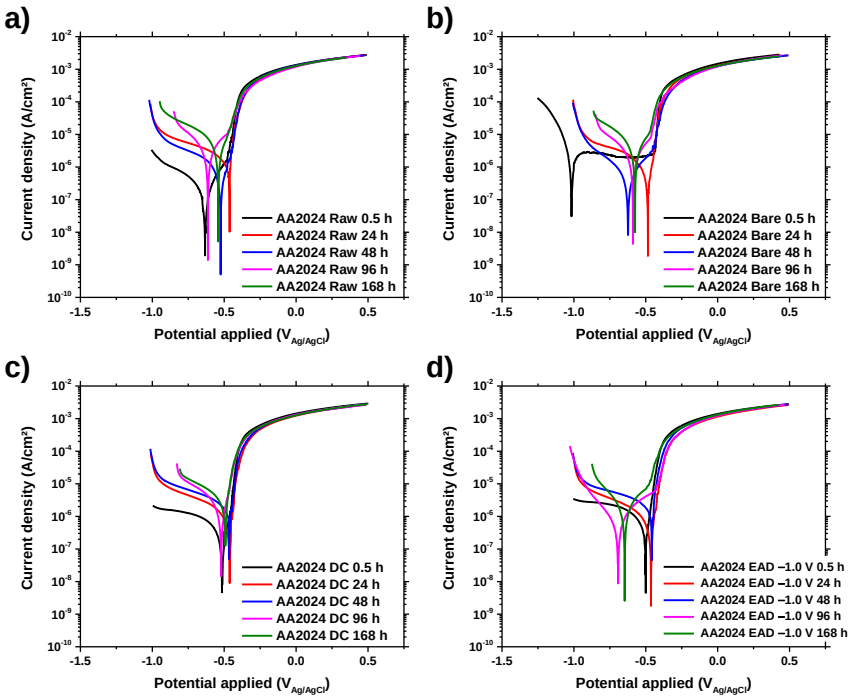

Figure 4.3.3. Polarization curves obtained for AA2024 specimens, throughout 168 h (7 days) of exposure in 0.05 M of NaCl solution, comparing the two methods used for the ZrO_2 metal deposition: **a)** Raw, **b)** Bare, **c)** Zr-DC method, and **d)** EAD method.

Table 4.3.2. Measured values of corrosion current density (j_{corr}) and corrosion potential (E_{corr}) of AA2024 samples, during polarization tests with increased exposure time in 0.05 M NaCl solution.

Sample	Exposure Time (h)	j_{corr} (A/cm²)	E_{corr} (V)
AA2024 Raw	0.5	4.52×10^{-7}	− 0.576
	24	1.83×10^{-6}	− 0.462
	48	1.10×10^{-6}	− 0.525
	96	3.36×10^{-6}	− 0.613
	168	5.12×10^{-6}	− 0.541
AA2024 Bare	0.5	1.57×10^{-6}	− 0.802 [1]
	24	1.37×10^{-6}	− 0.485
	48	5.93×10^{-7}	− 0.623
	96	2.15×10^{-6}	− 0.589
	168	3.98×10^{-6}	− 0.575
AA2024 DC	0.5	8.13×10^{-7}	− 0.517
	24	1.33×10^{-6}	− 0.462
	48	2.17×10^{-6}	− 0.468
	96	2.31×10^{-6}	− 0.520
	168	3.89×10^{-6}	− 0.491
AA2024 EAD	0.5	9.77×10^{-7}	− 0.575
	24	7.53×10^{-7}	− 0.463
	48	2.21×10^{-6}	− 0.458
	96	7.82×10^{-7}	− 0.692
	168	1.74×10^{-6}	− 0.647

Notes: [1] The breakdown potential (E_b) found for this sample was − 0.485 V. All data were obtained by Tafel extrapolation, using Nova 2.1 software.

In **Figure 4.3.4** the evolution of j_{corr} and E_{corr} with time is presented for comparison of the pre-treatments effects on both AA1100 and AA2024 substrates.

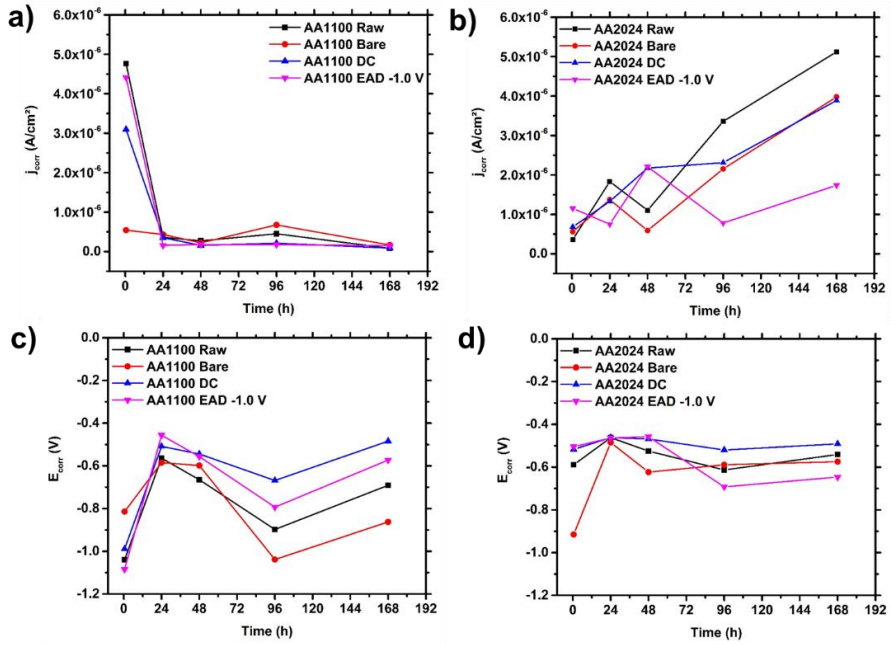

Figure 4.3.4. Corrosion current densities (j_{corr}) measured on: **a)** AA1100 and **b)** AA2024 substrates; and corrosion potentials (E_{corr}) measured on: **c)** AA1100 and **d)** AA2024 treated specimens. The values correspond to the Tafel extrapolation of the polarization curves (**Table 4.3.2**) obtained during the exposure of the analyzed samples to a NaCl 0.05M electrolyte, throughout 168 h (7 days).

4.3.2 Porosity and barrier properties of Zr-EAD and Zr-DC coatings evaluated by potentiodynamic polarization curves and EIS analysis

Different methods can be used to approach the coatings' porosity. One of them is the polarization resistance, in which the porosity of a passivation layer is calculated from the electrical resistance of the substrate without and with the coat, according to the area in contact with the electrolyte, then the solution reaches the substrate through the open porosity across the coating. For the coating porosity analysis, the untreated and treated aluminum surfaces were compared using the polarization resistance data obtained from Tafel extrapolation for samples immersed during 24 h in NaCl solution (**Equation 1**). The porosity values evidence that ZrO_2, generated by electrochemical method, are more compact (32.6 % and 38.6 %, for AA1100 and AA2024, respectively) than that obtained by

adsorption chemical deposition (60.4 % and 58.6 %, for AA1100 and AA2024, respectively). These values being almost twice the porosity of Zr-EAD coatings. Another observation is that the metal composition does not affect the porosity of the ZrO_2 nanofilms. On the contrary, aluminum oxides and hydroxides formed after substrates degreasing in alkaline mixture (Bare) are highly porous (86.9 %) in AA1100 if compared to AA2024 (41.5 %). It is supported by the previous explanation about such oxides/hydroxides stability differences on both surfaces, mentioned in the **Section 4.3.1**.

After polarization studies, EIS measurements were performed to evaluate the Zr oxide-based coating barrier resistance, generated by DC and EAD techniques; comparing to the Raw and Bare samples.

The Nyquist plots are mainly represented by a single time constant behavior corresponding to the electrical equivalent circuit (EEC) of $R_s(R_pCPE_{dl})$, where R_s represents the ohmic resistance of electrolyte solution, R_p is the polarization resistance of the interface coating, and CPE_{dl} corresponds to the double-layer constant phase element of a non-ideal capacitor, when the phase angle is different from − 90°. With increasing immersion time, a second constant phase element can appear due to the production of corrosion or other passivating layers under the film.

This approach was first carried out without the epoxy coating bilayer system. The Nyquist and Bode plots were evaluated after 24, 48, 96 and 168 h of samples immersion in the aggressive medium. These results are enclosed in **Figures 4.3.6** and **4.3.7**.

Table 4.3.3. EIS data obtained for AA1100 substrates, after immersion in NaCl solution, from 0.5 h to 168 h of exposure time.

Sample Code	Exposure Time (h)	R_s (Ω cm^2)	R_p (Ω cm^2)	CPE_{dl} (F cm^{-2} s^{n-1})	n_{CPE}
AA1100 Raw	0.5	349	6.2×10^3	3.7×10^{-5}	0.695
	24	346	7.3×10^4	2.2×10^{-5}	0.774
	48	353	20.6×10^4	7.7×10^{-6}	0.786
	96	354	21.8×10^4	7.3×10^{-6}	0.802
	168	331	15.1×10^4	1.1×10^{-5}	0.805
AA1100 Bare	0.5	349	9.9×10^3	1.9×10^{-5}	0.798
	24	331	7.6×10^4	2.1×10^{-5}	0.821
	48	353	17.3×10^4	9.2×10^{-6}	0.826
	96	324	10.9×10^4	1.5×10^{-5}	0.844
	168	356	7.7×10^4	2.1×10^{-5}	0.855
AA1100 DC	0.5	220	7.0×10^4	2.1×10^{-5}	0.792
	24	317	18.0×10^4	8.8×10^{-6}	0.816
	48	342	22.6×10^4	7.0×10^{-6}	0.804
	96	338	15.1×10^4	1.1×10^{-5}	0.817
	168	335	18.9×10^4	8.4×10^{-6}	0.821
AA1100 EAD	0.5	288	4.0×10^4	2.4×10^{-5}	0.779
	24	317	9.3×10^4	1.7×10^{-5}	0.790
	48	318	14.9×10^4	1.1×10^{-5}	0.785
	96	346	8.3×10^4	1.9×10^{-5}	0.847
	168	338	6.7×10^4	1.9×10^{-5}	0.851

A comparison between the polarization resistance (R_p) values of all samples, obtained from EIS experiments, is displayed in **Figure 4.3.5**. As can be seen in **Figure 4.3.5**, the polarization resistance (R_p), which is associated to the porous oxide interface between the metal substrate and the electrolyte solution as well as to the charge transfer resistance of the coating, has opposite trend in pure Al and Cu-rich surfaces. The R_p gradually raises until 48 h (**Figure 4.3.5a**) indicating a passivation ability in AA1100. However, this effect is not stable over time and the observed fluctuations after this time demonstrate the instability of the oxide coatings (Al_2O_3/AlOOH and ZrO_2, in Raw/Bare and DC/EAD samples, respectively). On the other hand, the trend observed for R_p of AA2024 surfaces (**Figure 4.3.5b**), shows that the Zr-EAD coating loses its barrier protection more gradually than Zr-DC sample, which rapidly achieves a plateau of low resistance value in only 24 h. The slowest decay of R_p in Zr-EAD layer on AA2024 can be explained due to the presence of less defects if compared to the chemical

conversion coating induced by ions diffusion in Zr-DC method. The comparatively higher values of R_p found in DC and EAD conversion coatings with respect to Raw and Bare samples in AA2024 at initial time (0.5 h, **Table 4.3.4**) is due to the well-covered intermetallic sites enriched in copper alloying composition, which favors the preferential nucleation of zirconium compounds, as stated previously in several works.[6,14,48]

Table 4.3.4. EIS data obtained for AA2024 substrates, after immersion in NaCl solution, from 0.5 h to 168 h of exposure time.

Sample Code	Exposure Time (h)	R_s (Ω cm^2)	R_p (Ω cm^2)	CPE_{dl} (F cm^{-2} s^{n-1})	n_{CPE}
AA2024 Raw	0.5	389	5.6×10^3	3.9×10^{-5}	0.896
	24	335	4.6×10^3	7.5×10^{-5}	0.830
	48	379	6.1×10^3	9.3×10^{-5}	0.779
	96	373	4.2×10^3	7.8×10^{-5}	0.847
	168	365	2.3×10^3	1.5×10^{-4}	0.864
AA2024 Bare	0.5	363	2.3×10^3	5.7×10^{-5}	0.868
	24	358	3.4×10^3	6.7×10^{-5}	0.897
	48	364	4.0×10^3	8.3×10^{-5}	0.836
	96	368	3.4×10^3	9.9×10^{-5}	0.865
	168	368	2.8×10^3	1.8×10^{-4}	0.862
AA2024 DC	0.5	383	2.9×10^4	1.4×10^{-5}	0.855
	24	353	2.9×10^3	6.0×10^{-5}	0.864
	48	371	4.6×10^3	1.3×10^{-4}	0.844
	96	364	2.8×10^3	1.4×10^{-4}	0.860
	168	367	2.7×10^3	2.1×10^{-4}	0.855
AA2024 EAD	0.5	395	2.7×10^4	2.7×10^{-5}	0.890
	24	401	1.3×10^4	3.5×10^{-5}	0.856
	48	392	9.7×10^3	8.4×10^{-5}	0.804
	96	360	7.6×10^3	1.7×10^{-4}	0.817
	168	371	4.5×10^3	1.9×10^{-4}	0.833

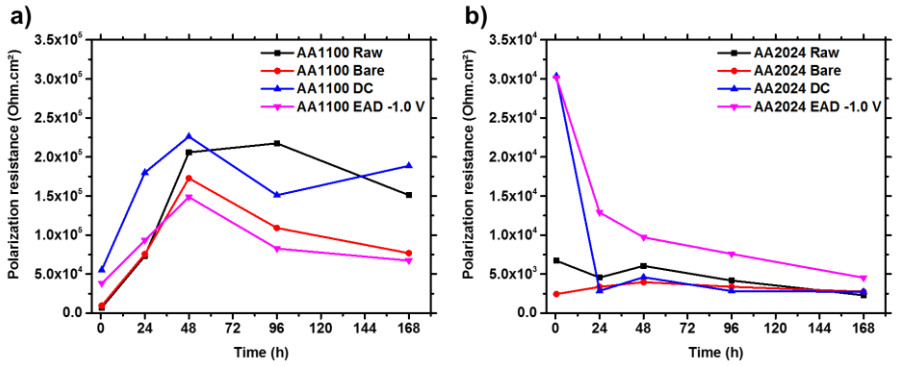

Figure 4.3.5. Polarization resistances of **a)** AA1100 and **b)** AA2024 samples, with increasing immersion time in NaCl solution (0.05 M).

The most relevant plots of Nyquist and Bode curves (24 h and 168 h) of AA1100 and AA2024 samples are showed in **Figures 4.3.6** and **4.3.7**.

After 168 h of test, it may be observed that all the AA1100 specimens suffered a slight reduction of their resistive property, if compared to the first immersion step (24h). Considering that the sample AA1100 Zr-DC is the one that had the less pronounced change throughout the test, there is a possibility that the pseudo-barrier protection provided by the ZrO_2 film partially avoids the growth of the Al_2O_3 layer. The Zr-DC film resulted in the highest impedance values after 168 h of analysis.

Contrasting with the observed impedance response of AA1100 alloy, it is noticeable in **Figure 4.3.7** that all the AA2024 samples had a decrease in the impedance values throughout the test duration and a second time constant appeared at low frequencies.

At the conclusion of the test, as seen in **Figure 4.3.7a1)** and **Figure 4.3.7b1)**, the Zr-EAD sample provided the best protection to the substrate, with increased exposure time. Thus, AA2024 Zr-EAD seems to have a more stable, more uniform and more compact film, as observed by SEM (**Figure 4.3.1**). Unlike the AA1100 alloy, it is evident that in Cu-rich alloy, whose native oxide layer does not provide a satisfactory barrier protection, the production of ZrO_2 by EAD method generates a more efficient barrier able to diminish electrolyte penetration.

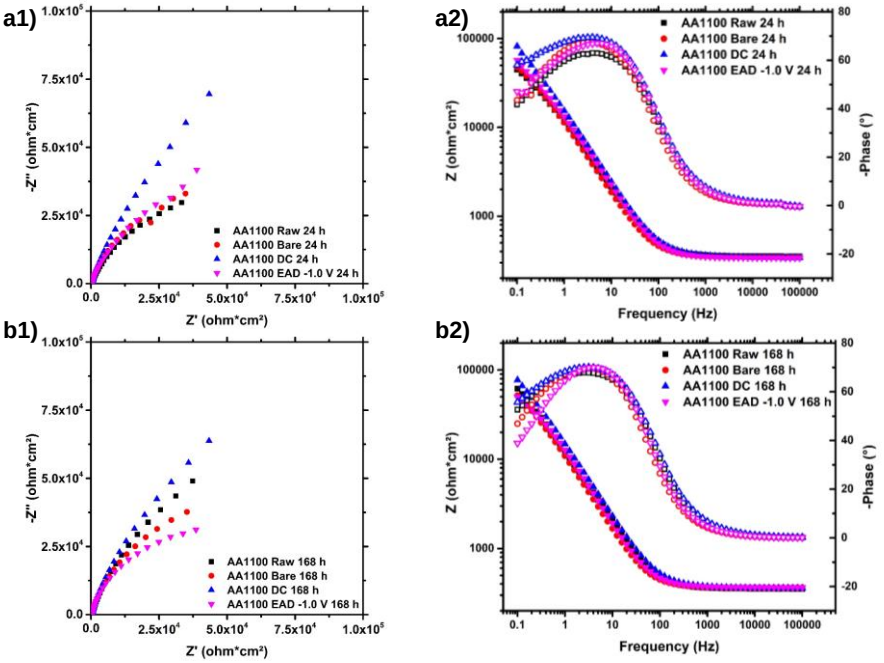

Figure 4.3.6. 1) Nyquist and **2)** Bode diagrams obtained from EIS tests of AA1100 pre-treated samples, after: **a)** 24 h and **b)** 168 h of exposure to the electrolyte solution.

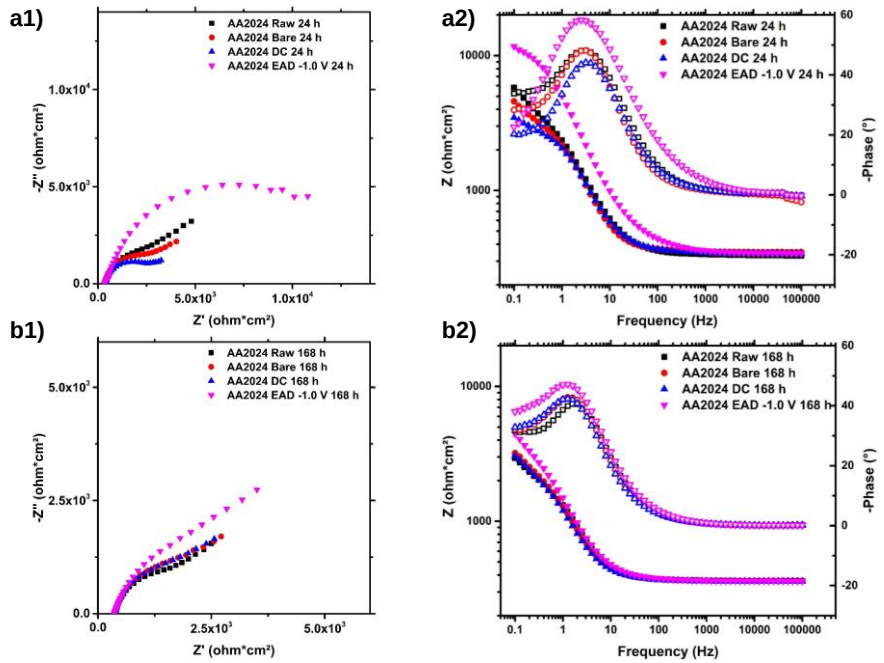

Figure 4.3.7. 1) Nyquist and **2)** Bode diagrams obtained from EIS tests of AA2024 pre-treated samples after: **a)** 24 h and **b)** 168 h of exposure to the electrolyte solution.

Another possible approach for the comparison of the different treatments throughout the exposure time is the analysis of the impedance module |Z| at low frequencies, which is proportionally related to the corrosion resistance.[17,49] Such comparison is shown in **Figure 4.3.8**. The results evidenced similar conclusions as that found with the R_p analysis.

A general trend of increase in |Z| is visible for all the surface treatments on AA1100 samples (**Figure 4.3.8a**), with the dip-coated sample (DC) having the highest impedance value during the entire test and maintaining almost constant over time. All other substrates exhibited a fast raise in |Z| modulus at first 48 h of immersion in aggressive solution, but their impedance values become instable after this time. The fact that the impedance module increases during the exposure to the electrolyte in both coated and non-coated samples evidences the self-healing behavior of such oxides in the protection of the metal surface. However, the instability of the oxide nanocoatings leads to a rapid penetration of chlorine ions, destroying the pseudo-barrier protection achieved at short immersion times.

On the other hand, in AA2024 (**Figure 4.3.8b**) samples, a general trend of |Z| modulus decrease was observed during the test. Meanwhile, the ZrO_2 generated by EAD method had a smooth decay if compared to the other substrates, showing a better coating resistance in NaCl solution for the analyzed period. Both samples coated with ZrO_2 presents a good impedance value at very short exposure time (0.5 h). The Zr-EAD treatment had the highest |Z| during the entire test. Generally, the sharp decrease in |Z| modulus is most likely a consequence of the presence of intermetallic particles in AA2024 surface. After 168 hours of test, EAD resulted in 4449 ohm·cm² and the other treatments' impedances were within the range between 2900 and 3100 ohm·cm².

Such results support the data of porosity calculated by the polarization resistance study for coatings with 24 h of salt solution immersion, i.e., higher porosity implies lower barrier protection.

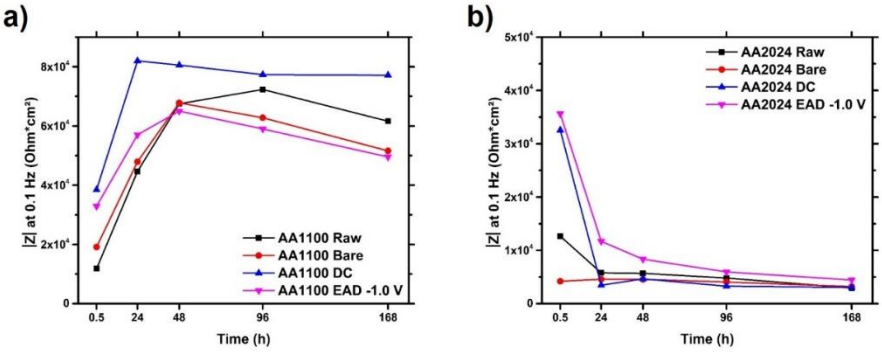

Figure 4.3.8. Impedance modules |Z| at 0.1 Hz, measured through electrochemical impedance spectroscopy, from 0.5 hour to 168 hours of immersion in NaCl 0.05 M solution: **a)** AA1100 and **b)** AA2024 substrates, with different pre-treatments.

4.3.3 Barrier properties of Zr-EAD and Zr-CCC nanocoatings in accelerated corrosion test

In order to have a direct comparison between the most relevant pretreatments in AA2024 substrates, a cyclic accelerated corrosion test was performed with Bare, Zr-DC and Zr-EAD non-painted specimens. **Figure 4.3.9** shows the evolution of the corroded areas during the test according to the computational image analysis method explained in the **Appendix A**.

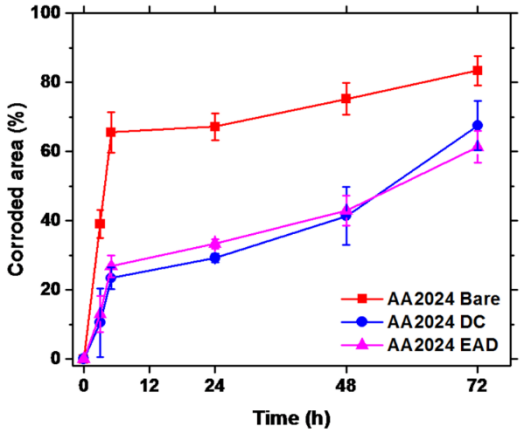

Figure 4.3.9. Measured corroded areas during 72 h of cyclic accelerated corrosion test with non-painted AA2024 substrates.

A sharp increase in the corroded area was observed for all samples during the first 5 hours of the test, after which a less pronounced corrosion growth is noticed until the end of the test. Despite the surface presented visible corrosion products

after initial electrolyte exposure, the corroded areas of the Zr- DC and Zr-EAD are consistently smaller than the ones observed in Bare samples throughout the entire test, being approximately half of it after 5 h. During the tested period both DC and EAD had similar results, which indicates that the differences observed between these two methods do not lead to significant changes in the barrier protection in the aggressive environment tested. Given the very thin thickness of such films and their porosities, this result is in agreement with the previous observations obtained by electrochemical assays. Photographs of representative specimens that underwent this test are available in **Figure 4.3.10**.

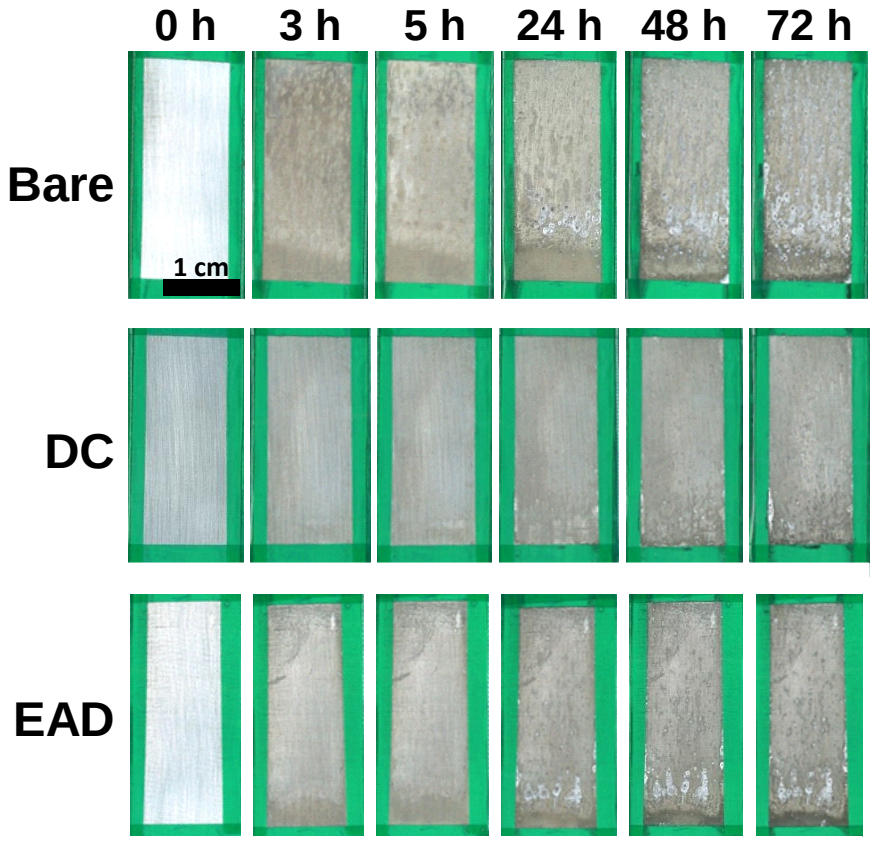

Figure 4.3.10. Photographs of AA2024 specimens submitted to cyclic accelerated corrosion test during 72 hours. The scale bar applies to all images.

The presence of corrosion products (white spots) confirms that the corrosion resistance provided by the Zr-based nanocoating is not enough to act as a protective barrier layer, as the progressive penetration of chlorine ions leads to the

barrier destruction. Therefore, a further layer of organic impermeable coating is urged. Even in conditions where the native oxide layer provides more barrier protection, the zirconium conversion coating uses can be seen as an effective solution for the subsequent deposition of organic coatings, as stated previously.[6,11,19] Thus, the ZrO_2 nanocoating effect in the promotion of organic coatings adherence will be discussed in the next section.

4.3.4 Evaluation of the dual organic-inorganic protected aluminum substrates under prolonged exposition to NaCl solution

Accelerated corrosion test was carried out in an automated robot and in a more aggressive environment (NaCl 3.5 wt. %) if compared to previous electrochemical studies. The samples were extracted every 30 days, until completing 90 days of testing. Taking into account that the best results of zirconium oxide layer (good homogeneity and compactness observed by polarization and SEM analyses) were obtained with the EAD method, it was the process tried for the deposition of an additional barrier coat. Bare substrates (*i.e.*, degreased AA1100 and AA2024 substrates) were chosen for comparison with the Zr-EAD samples, due to the worst case of such interface composed mainly by Al_2O_3 and hydroxide compounds. **Figure 4.3.11** includes the photographs of plates (AA1100) and discs (AA2024) used, before and after 90 days of cyclic assay.

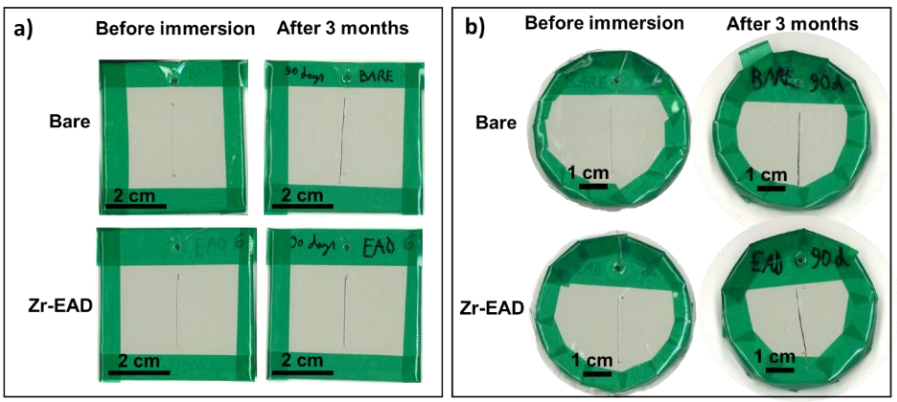

Figure 4.3.11. Digital photographs of **a)** AA1100 plates and **b)** AA2024 discs, before and after 90 days of accelerated corrosion assays (NaCl 3.5 wt.%).

Apparently, the macroscopic images do not evidence any corrosion product in the surface or in the cutting marks. However, cross-section SEM images of the samples submitted to this test (**Figure 4.3.12**) revealed important differences.

In this sense, although paint delamination or blistering were not observed during the accelerated corrosion test in the macroscopic images, microscopic observation of the metal/primer interface revealed a noticeable loss of organic coating adherence in Bare samples (**Figure 4.3.12a2** and **Figure 4.3.12c2**). On the contrary, the presence of Zr-EAD avoided the organic coating delamination (**Figure 4.3.12b2** and **Figure 4.3.12d2**). This observation indicates that the pre-treatment induced by EAD method efficiently maintains the protection of either AA1100 or AA2024 alloys throughout extended exposition periods, which is a fundamental requirement for its use as a pre-treatment for the application of organic topcoats.

Figure 4.3.12 shows only non-scribed zones. Additional cross section optical microscopy images from scribed area of both Bare and EAD samples coated with epoxy primer are presented in **Figure 4.3.13**.

It is observable that in all Zr-EAD specimens the paint adherence is not limited to the area far from the defect but also in the scribed mark surrounding, where the formation of corrosion products usually promotes the paint delamination. Altogether proves that zirconium oxide conversion coatings are a useful pre-treatment to potentiate the integrity of the metal/primer interface, even in structural alloys, like AA2024, that is more prone to corrosion due to the presence of Cu-rich intermetallic clusters.

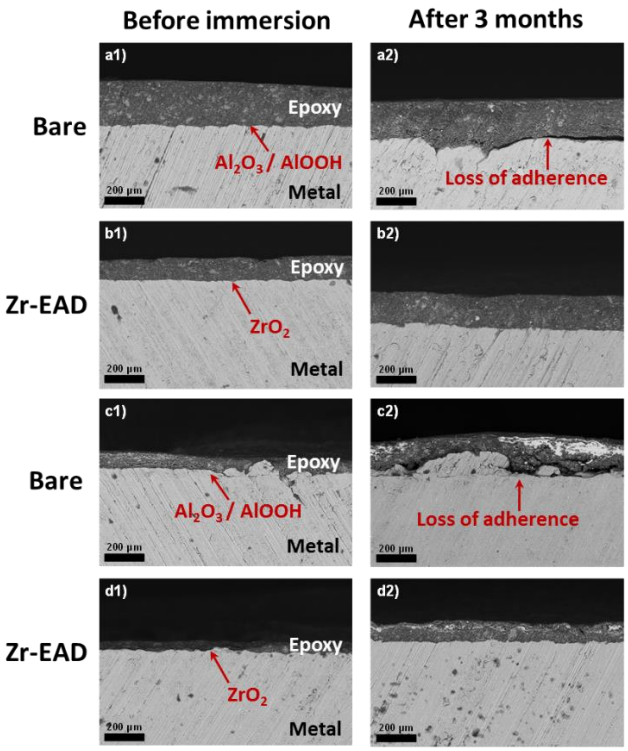

Figure 4.3.12. Cross-section SEM images of the following specimens: **a)** AA1100 Bare, **b)** AA1100 EAD, **c)** AA2024 Bare and **d)** AA2024 EAD; **1)** before and **2)** after 90 days of cyclic immersion corrosion test in NaCl 3.5 wt. %.

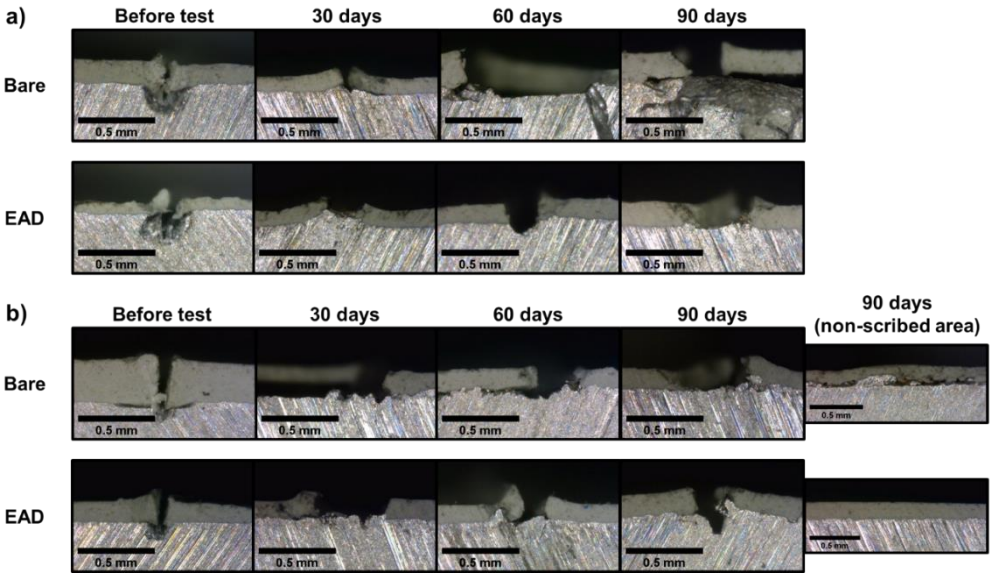

Figure 4.3.13. Optical microscopy images of the cross-section of scribed areas in: **a)** AA1100 and **b)** AA2024 specimens, submitted to accelerated corrosion test during 90 days.

4.3.5 Scratch testing

Scratch tests did not produce a clear delamination differences between Bare/epoxy coating and Zr-EAD/epoxy coating in AA1100 samples. However, detailed inspection of the deformation produced by scratching in AA2024/epoxy material revealed some dissimilarity.

In **Figure 4.3.14**, the mark produced in the scratch test of AA2024 specimens after 90 days of cyclic immersion test is presented. The abovementioned loss of epoxy coating adhesion in Bare samples may have been initiated in small defects or irregularities present on the Al oxide/hydroxide interface. Careful inspection of the image shown in **Figure 4.3.14a** reveals that the organic coating is also microcracked, which implies that, not only it loses adhesion after immersion, but also the structural integrity of the epoxy coating as well. Moreover, Zr-EAD/epoxy coating (**Figure 4.3.14b**), in contrast, presents a good adhesion and with no visible microcracking after immersion, indicating that the mechanical performance on service is better than the Bare pre-treatment.[19]

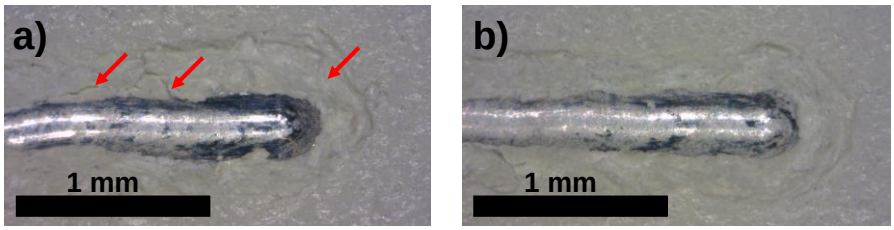

Figure 4.3.14. Optical microscopy images of the scratch zone, produced after indentation test of AA2024 specimens, under 90 days of cyclic immersion corrosion test in NaCl (3.5 wt. %): **a)** AA2024 Bare/epoxy coating and **b)** AA2024 Zr-EAD/epoxy coating. Red arrows indicate microcracking zones.

4.4 *Conclusions*

In this work, AA1100 surfaces containing ZrO_2 nanocoatings proved to have high instability of its native oxide/hydroxide interface layer, in long exposition time, than that of AA2024 structural alloy. Although the Zr-based nanocoatings are porous, the presence of such nanometric zirconium oxide film is still beneficial for both substrates if compared to the aluminum surface uniquely ground or degreased with alkaline solution.

The low barrier property of the zirconium oxide films was overcome by the application of a further layer of an anticorrosive organic coating. The long-term accelerated corrosion tests and the scratch assays demonstrated the superior adherence of samples with an ultra-thin layer of ZrO_2, generated by electro-assisted technique, probably due to the lower porosity found with this technique. The dual system is able to maintain the integrity of the metal surface and the coating adherence as long as 90 days, whereas samples without Zr-based nanocoatings cannot do. Altogether Zr-EAD represents an alternative to chromate and phosphatizing processes, which have several environmental problems related to the toxicity of chemical baths and to the large amount of waste generation.

4.5 *References*

(1) Narayanan, T. S. N. S. Surface Pretreatment by Phosphate Conversion Coatings - A Review. *Rev. Adv. Mater. Sci.* **2005**, *9* (2), 130–177.

(2) Velasquez, C. S.; Pimenta, E. P. S.; Lins, V. F. C. Anticorrosive Behavior and Porosity of Tricationic Phosphate and Zirconium Conversion Coating on Galvanized Steel. *J. Mater. Eng. Perform.* **2018**, *27* (5), 2138–2147. https://doi.org/10.1007/s11665-018-3294-x.

(3) European Parliament and of the Council. *Regulation (EC) No 1907/2006 - Registration, Evaluation, Authorisation and Restriction of Chemicals (REACH)*; 2006.

(4) Becker, M. Chromate-Free Chemical Conversion Coatings for Aluminum Alloys. *Corros. Rev.* **2019**, *37* (4), 321–342. https://doi.org/10.1515/corrrev-2019-0032.

(5) Gharbi, O.; Thomas, S.; Smith, C.; Birbilis, N. Chromate Replacement: What Does the Future Hold? *npj Mater. Degrad.* **2018**, *2* (1), 23–25. https://doi.org/10.1038/s41529-018-0034-5.

(6) Milošev, I.; Frankel, G. S. Review—Conversion Coatings Based on Zirconium and/or Titanium. *J. Electrochem. Soc.* **2018**, *165* (3), C127–C144. https://doi.org/10.1149/2.0371803jes.

(7) Doerre, M.; Hibbitts, L.; Patrick, G.; Akafuah, N. Advances in Automotive Conversion Coatings during Pretreatment of the Body Structure: A Review. *Coatings* **2018**, *8* (11), 405. https://doi.org/10.3390/coatings8110405.

(8) Yoganandan, G.; Pradeep Premkumar, K.; Balaraju, J. N. Evaluation of Corrosion Resistance and Self-Healing Behavior of Zirconium–Cerium Conversion Coating Developed on AA2024 Alloy. *Surf. Coatings Technol.* **2015**, *270*, 249–258. https://doi.org/10.1016/j.surfcoat.2015.02.049.

(9) Asemani, H. R.; Ahmadi, P.; Sarabi, A. A.; Eivaz Mohammadloo, H. Effect of Zirconium Conversion Coating: Adhesion and Anti-Corrosion Properties of Epoxy Organic Coating Containing Zinc Aluminum Polyphosphate (ZAPP) Pigment on Carbon Mild Steel. *Prog. Org. Coatings* **2016**, *94*, 18–27. https://doi.org/10.1016/j.porgcoat.2016.01.015.

(10) Liu, Y.; Yang, Y.; Zhang, C.; Zhang, T.; Yu, B.; Meng, G.; Shao, Y.; Wang, F.; Liu, L. Protection of AA5083 by a Zirconium-Based Conversion Coating. *J. Electrochem. Soc.* **2016**, *163* (9), C576–C586. https://doi.org/10.1149/2.1021609jes.

(11) Fockaert, L. I.; Taheri, P.; Abrahami, S. T.; Boelen, B.; Terryn, H.; Mol, J. M. C. Zirconium-Based Conversion Film Formation on Zinc, Aluminium and Magnesium Oxides and Their Interactions with Functionalized Molecules. *Appl. Surf. Sci.* **2017**, *423*, 817–828. https://doi.org/10.1016/j.apsusc.2017.06.174.

(12) Cerezo, J.; Vandendael, I.; Posner, R.; Lill, K.; de Wit, J. H. W.; Mol, J. M. C.; Terryn, H. Initiation and Growth of Modified Zr-Based Conversion Coatings on Multi-Metal Surfaces. *Surf. Coatings Technol.* **2013**, *236*, 284–289. https://doi.org/10.1016/j.surfcoat.2013.09.059.

(13) George, F. O.; Skeldon, P.; Thompson, G. E. Formation of Zirconium-Based Conversion Coatings on Aluminium and Al–Cu Alloys. *Corros. Sci.* **2012**, *65*, 231–237. https://doi.org/10.1016/j.corsci.2012.08.031.

(14) Sarfraz, A.; Posner, R.; Lange, M. M.; Lill, K.; Erbe, A. Role of Intermetallics and Copper in the Deposition of ZrO 2 Conversion Coatings on AA6014 . *J. Electrochem. Soc.* **2014**, *161* (12), C509–C516. https://doi.org/10.1149/2.0121412jes.

(15) Pinheiro, J. S.; Regio, G.; Cardoso, H. R. P.; Oliveira, C. T.; Ferreira, J. Z. Influence of Concentration and PH of Hexafluorozirconic Acid on Corrosion Resistance of Anodized AA7075-T6. *Mater. Res.* **2019**, *22* (suppl 1), 1–11. https://doi.org/10.1590/1980-5373-MR-2019-0048.

(16) Cardoso, H. R. P.; Rapacki, C.; Ferreira, J. Z. Monitoring of a Zr-Based Conversion Coating on Galvanised Steel and Its Performance against Corrosion. *Corros. Eng. Sci. Technol.* **2019**, *54* (8), 726–730. https://doi.org/10.1080/1478422X.2019.1657703.

(17) Šekularac, G.; Milošev, I. Electrochemical Behavior and Self-Sealing Ability of Zirconium Conversion Coating Applied on Aluminum Alloy 3005 in 0.5 M NaCl Solution. *J. Electrochem. Soc.* **2020**, *167* (2), 021509. https://doi.org/10.1149/1945-7111/ab6b0d.

(18) van Dam, J. P. B.; Abrahami, S. T.; Yilmaz, A.; Gonzalez-Garcia, Y.; Terryn, H.; Mol, J. M. C. Effect of Surface Roughness and Chemistry on the Adhesion and Durability of a Steel-Epoxy Adhesive Interface. *Int. J. Adhes. Adhes.* **2020**, *96* (October), 102450. https://doi.org/10.1016/j.ijadhadh.2019.102450.

(19) Fockaert, L. I.; Pletincx, S.; Ganzinga-Jurg, D.; Boelen, B.; Hauffman, T.; Terryn, H.; Mol, J. M. C. Chemisorption of Polyester Coatings on Zirconium-Based Conversion Coated Multi-Metal Substrates and Their Stability in Aqueous Environment. *Applied Surface Science*. 2020. https://doi.org/10.1016/j.apsusc.2019.144771.

(20) Eivaz Mohammadloo, H.; Sarabi, A. A.; Mohammad Hosseini, R.; Sarayloo, M.; Sameie, H.; Salimi, R. A Comprehensive Study of the Green Hexafluorozirconic Acid-Based Conversion Coating. *Prog. Org. Coatings* **2014**, *77* (2), 322–330. https://doi.org/10.1016/j.porgcoat.2013.10.006.

(21) Lostak, T.; Krebs, S.; Maljusch, A.; Gothe, T.; Giza, M.; Kimpel, M.; Flock, J.; Schulz, S. Formation and Characterization of Fe3+-/Cu2+-Modified Zirconium Oxide Conversion Layers on Zinc Alloy Coated Steel Sheets. *Electrochim. Acta* **2013**, *112*, 14–23. https://doi.org/10.1016/j.electacta.2013.08.161.

(22) Ghanbari, A.; Attar, M. M. Surface Free Energy Characterization and Adhesion Performance of Mild Steel Treated Based on Zirconium Conversion Coating: A Comparative Study. *Surf. Coatings Technol.* **2014**, *246*, 26–33. https://doi.org/10.1016/j.surfcoat.2014.02.057.

(23) Sababi, M.; Terryn, H.; Mol, J. M. C. The Influence of a Zr-Based Conversion Treatment on Interfacial Bonding Strength and Stability of Epoxy Coated Carbon Steel. *Prog. Org. Coatings* **2017**, *105*, 29–36. https://doi.org/10.1016/j.porgcoat.2016.11.016.

(24) Taheri, P.; Laha, P.; Terryn, H.; Mol, J. M. C. An in Situ Study of Zirconium-Based Conversion Treatment on Zinc Surfaces. *Appl. Surf. Sci.* **2015**, *356*, 837–843. https://doi.org/10.1016/j.apsusc.2015.08.205.

(25) Reck, J.; Wang, Y.-M.; Kuo, H.-H. H. Development of Zirconium-Based Conversion Coatings for the Pretreatment of AZ91D Magnesium Alloy Prior to Electrocoating. In *Magnesium Technology 2011*; Sillekens W.H., Agnew S.R., Neelameggham N.R., M. S. N., Ed.; Springer International Publishing, 2011; pp 523–529. https://doi.org/10.1007/978-3-319-48223-1_97.

(26) Andreatta, F.; Paussa, L.; Lanzutti, A.; Rosero Navarro, N. C.; Aparicio, M.; Castro, Y.; Duran, A.; Ondratschek, D.; Fedrizzi, L. Development and Industrial Scale-up of ZrO2 Coatings and Hybrid Organic–Inorganic Coatings Used as Pre-Treatments before Painting Aluminium Alloys. *Prog. Org. Coatings* **2011**, *72* (1–2), 3–14. https://doi.org/10.1016/j.porgcoat.2011.01.011.

(27) Santa Coloma, P.; Izagirre, U.; Belaustegi, Y.; Jorcin, J. B.; Cano, F. J.; Lapeña, N. Chromium-Free Conversion Coatings Based on Inorganic Salts (Zr/Ti/Mn/Mo) for Aluminum Alloys Used in Aircraft Applications. *Appl. Surf. Sci.* **2015**, *345*, 24–35. https://doi.org/10.1016/j.apsusc.2015.02.179.

(28) Moreira, V. B.; Puiggalí-Jou, A.; Jiménez-Piqué, E.; Alemán, C.; Meneguzzi, A.; Armelin, E. Green Nanocoatings Based on the Deposition of Zirconium Oxide: The Role of the Substrate. *Materials (Basel).* **2021**, *14* (4), 1–18. https://doi.org/10.3390/ma14041043.

(29) Dong, X.; Argekar, S.; Wang, P.; Schaefer, D. W. In Situ Evolution of Trivalent Chromium Process Passive Film on Al in a Corrosive Aqueous Environment. *ACS Appl. Mater. Interfaces* **2011**, *3* (11), 4206–4214. https://doi.org/sw.

(30) Gal-Or, L.; Silberman, I.; Chaim, R. Electrolytic ZrO2 Coatings: I. Electrochemical Aspects. *J. Electrochem. Soc.* **1991**, *138* (7), 1939–1942. https://doi.org/10.1149/1.2085904.

(31) Chaim, R.; Silberman, I.; Gal-Or, L. Electrolytic Zr02 Coatings: II. Microstructural Aspects. *J. Electrochem. Soc.* **1991**, *138* (7), 5.

(32) Yen, S. K. Characterization of Electrolytic ZrO2 Coating on AISI 316L Stainless Steel. *J. Electrochem. Soc.* **1999**, 5.

(33) Yen, S. .; Guo, M. .; Zan, H. . Characterization of Electrolytic ZrO2 Coating on Co–Cr–Mo Implant Alloys of Hip Prosthesis. *Biomaterials* **2001**, *22* (2), 125–133. https://doi.org/10.1016/S0142-9612(00)00133-2.

(34) Shacham, R.; Mandler, D.; Avnir, D. Electrochemically Induced Sol–Gel Deposition of Zirconia Thin Films. *Chem. - A Eur. J.* **2004**, *10* (8), 1936–1943. https://doi.org/10.1002/chem.200305469.

(35) Liu, L.; Mandler, D. Electrochemical Deposition of Sol-Gel Films. In *Handbook of Sol-Gel Science and Technology*; Springer International Publishing: Cham, 2018; pp 531–568. https://doi.org/10.1007/978-3-319-32101-1_113.

(36) Creus, J.; Mazille, H.; Idrissi, H. Porosity Evaluation of Protective Coatings onto Steel, through Electrochemical Techniques. *Surf. Coatings Technol.* **2000**, *130* (2–3), 224–232. https://doi.org/10.1016/S0257-8972(99)00659-3.

(37) Chai, Z.; Li, J.; Lu, X.; He, D. Use of Electrochemical Measurements to Investigate the Porosity of Ultra-Thin Al2O3 Films Prepared by Atomic Layer Deposition. *RSC Adv.* **2014**, *4* (74), 39365–39371. https://doi.org/10.1039/c4ra04565c.

(38) Liesa, F.; Alemán, C.; Iribarren, J. I. Brazo Mecánico Para Realizar Ensayos de Corrosión Acelerados. ES2304267A1, 2005.

(39) Liesa, F.; Ocampo, C.; Alemán, C.; Armelin, E.; Oliver, R.; Estrany, F. Application of Electrochemically Produced and Oxidized Poly(3,4-Ethylenedioxythiophene) as Anticorrosive Additive for Paints: Influence of the Doping Level. *J. Appl. Polym. Sci.* **2006**, *102* (2), 1592–1599. https://doi.org/10.1002/app.23925.

(40) Ocampo, C.; Armelin, E.; Liesa, F.; Alemán, C.; Ramis, X.; Iribarren, J. I. Application of a Polythiophene Derivative as Anticorrosive Additive for Paints. *Prog. Org. Coatings* **2005**, *53* (3), 217–224. https://doi.org/10.1016/j.porgcoat.2005.02.009.

(41) Armelin, E.; Pla, R.; Liesa, F.; Ramis, X.; Iribarren, J. I.; Alemán, C. Corrosion Protection with Polyaniline and Polypyrrole as Anticorrosive Additives for Epoxy Paint. *Corros. Sci.* **2008**, *50* (3), 721–728. https://doi.org/10.1016/j.corsci.2007.10.006.

(42) Iribarren-Mateos, J. I.; Buj-Corral, I.; Vivancos-Calvet, J.; Alemán, C.; Iribarren, J. I.; Armelin, E. Silane and Epoxy Coatings: A Bilayer System to Protect AA2024 Alloy. *Prog. Org. Coatings* **2015**, *81*, 47–57. https://doi.org/10.1016/j.porgcoat.2014.12.014.

(43) Bonamigo Moreira, V.; Krummenauer, A.; Zoppas Ferreira, J.; Veit, H. M.; Armelin, E.; Meneguzzi, A. Computational Image Analysis as an Alternative Tool for the Evaluation of Corrosion in Salt Spray Test. *Stud. Univ. Babeș-Bolyai*

Chem. **2020**, *65* (3), 45–61. https://doi.org/10.24193/subbchem.2020.3.04.

(44) Boukerche, I.; Djerad, S.; Benmansour, L.; Tifouti, L.; Saleh, K. Degradability of Aluminum in Acidic and Alkaline Solutions. *Corros. Sci.* **2014**, *78*, 343–352. https://doi.org/10.1016/j.corsci.2013.10.019.

(45) de Frutos, A.; Arenas, M. A.; Liu, Y.; Skeldon, P.; Thompson, G. E.; de Damborenea, J.; Conde, A. Influence of Pre-Treatments in Cerium Conversion Treatment of AA2024-T3 and 7075-T6 Alloys. *Surf. Coatings Technol.* **2008**, *202* (16), 3797–3807. https://doi.org/10.1016/j.surfcoat.2008.01.027.

(46) Li, L.; Desouza, A. L.; Swain, G. M. Effect of Deoxidation Pretreatment on the Corrosion Inhibition Provided by a Trivalent Chromium Process (TCP) Conversion Coating on AA2024-T3. *J. Electrochem. Soc.* **2014**, *161* (5), C246–C253. https://doi.org/10.1149/2.031405jes.

(47) Birbilis, N.; Zhu, Y. M.; Kairy, S. K.; Glenn, M. A.; Nie, J. F.; Morton, A. J.; Gonzalez-Garcia, Y.; Terryn, H.; Mol, J. M. C.; Hughes, A. E. A Closer Look at Constituent Induced Localised Corrosion in Al-Cu-Mg Alloys. *Corros. Sci.* **2016**, *113*, 160–171. https://doi.org/10.1016/j.corsci.2016.10.018.

(48) Torras, J.; Azambuja, D. S. D. S.; Wolf, J. M. J. M.; Alemán, C.; Armelin, E. How Organophosphonic Acid Promotes Silane Deposition onto Aluminum Surface: A Detailed Investigation on Adsorption Mechanism. *J. Phys. Chem. C* **2014**, *118* (31), 17724–17736. https://doi.org/10.1021/jp5046707.

(49) Šekularac, G.; Kovač, J.; Milošev, I. Prolonged Protection, by Zirconium Conversion Coatings, of AlSi7Mg0.3 Aluminium Alloy in Chloride Solution. *Corrosion Science*. 2020. https://doi.org/10.1016/j.corsci.2020.108615.

5 Epoxy coatings from limonene and CO_2: looking into the future of promising biobased thermosets with tunable properties

SUMMARY

In the area of coatings development, it is extremely difficult to find a substitute for bisphenol A diglycidyl ether (DGEBA), the classical petroleum based raw material used for the formulation of epoxy thermosets. This epoxy resin offers fast curing reaction with several hardeners and the best thermal and chemical resistance properties to be used in coatings and adhesive technologies. In this work, a new biobased epoxy, derived from poly(limonene carbonate) oxide (PLCO), was combined with polyetheramine and polyamineamide curing agents, offering a spectrum of thermal and mechanical properties comparable to DGEBA-based thermosets. The best formulation was found to be a combination of PLCO and a commercial curing agent (Jeffamine) in a stoichiometric 1:1 ratio. Although PLCO is a solid due to its high molecular weight, it was possible to create a two-components partially biobased epoxy paint without the need of volatile organic compounds (i.e., solvent-free formulation), intended to be used in coatings technology to partially replace DGEBA-based thermosets.

THE CONTENT OF THE PRESENT CHAPTER CANNOT BE DISCLOSED DUE TO A CONFIDENTIALITY AGREEMENT REGARDING A PATENT SUBMISSION.

THE NON-DISCLOSURE AGREEMENT IS VALID UNTIL **OCTOBER 31ST 2024**.

6 Biosourced epoxy resin for adhesive thermoset applications

SUMMARY

Biobased epoxy-derived raw materials will be essential for future coating and adhesive designs in industry. Here, a facile approach is reported towards the incorporation of limonene into an epoxy-functionalized polycarbonate and its crosslinking with a polyamine curing agent to obtain a thermoset material. For the first time, a solvent-borne adhesive with excellent film-forming, mechanical and adhesion strength properties is described.

Thus, this chapter compiles the applicability of the ZrO_2 nanocoating generated by electro-assisted deposition, described in the previous Chapters 3 and 4, with the deposition of a thermoset polymer, derived from poly(limonene carbonate) oxide (PLCO) introduced in the Chapter 5.

THE CONTENT OF THE PRESENT CHAPTER CANNOT BE DISCLOSED DUE TO A CONFIDENTIALITY AGREEMENT REGARDING A PATENT SUBMISSION.

THE NON-DISCLOSURE AGREEMENT IS VALID UNTIL **OCTOBER 31ST 2024**.

7. Conclusions

7 Conclusions

This chapter comprises a summary of the main conclusions drawn from the studies presented in the **Chapters 3**, **4**, **5** and **6** of this thesis.

The production of ZrCC films using the EAD technique can be carried out without adding any additive in the conversion bath, being necessary only the presence of the precursor (H_2ZrF_6) and a control over the voltage applied, for a successful coating deposition on multiple substrates. These substrates include conductive materials on which the reactions necessary for the conventional deposition method are not sufficient for the film formation, such as ITO and pure copper.

The substrate has an influence on the ZrCC formation even when EAD is used, indicating that the deposition reactions that occur during dip-coating still take place when the electrolysis of water is induced electrochemically in the EAD method. Therefore, substrates with more active sites, such as Cu-rich intermetallic particles in the AA2024 alloy, are more favorable to film formation regardless of the used method.

The thickness of the ZrCC films can be increased with enhanced EAD time, but there is a compromise between film thickness and film integrity. Thicker films may be brittle, cracked and loosely adhered to the substrate.

Short-term corrosion protection may be provided by ZrCC, but the main benefit in using it relies in its application as a pretreatment for top coats. In this scenario, a dual layer coating system comprising a ZrCC pretreatment produced by EAD method and an commercial epoxy primer has proved to be able to protect aluminum substrates in cyclic corrosion tests for over 90 days, preventing corrosion and paint delamination. The same protection was not achieved without the ZrCC pretreatment.

The production of new thermoset epoxy polymers, by using PLCO and PCO biobased resins with industrial hardeners, was achieved for the first time. The properties of such thermosets may be altered by tuning the epoxy/hardener proportions and nature, enabling various potential applications.

As PLCO is less reactive than the commercial DGEBA, it requires thermal curing in order to provide fully crosslinked thermosets. The calorimetric curing study led to the conclusion that the most adequate hardener among the studied ones was polyoxypropylenediamine (Jeffamine® D-400).

PLCO-biobased polymeric films were produced on aluminum substrates with previous Zr-EAD deposition. This adherent bilayer system has also provided corrosion protection for the Al substrate under NaCl electrolyte exposition. The new thermoset film did not contain any other components generally used in paint formulations to improve the barrier permeation, so further improvements may be achieved with the addition of usual paint additives, such as pigments, fillers and corrosion inhibitors.

A PLCO derivative compound, namely PCO, was also used for the production of new epoxy thermosets with industrial hardener. PCO presents two different epoxy components in its molecule, with the most frequent repeating unit being the same as in PLCO. The polymers obtained by reacting PCO with polyoxypropylenediamine hardener are less brittle and more adherent than the DGEBA-based ones. PCO and DGEBA may be combined to generate a partial biobased epoxy resin in order to produce thermosets with different mechanical and thermal properties, enabling to reduce the amount of DGEBA in epoxy formulations, i.e. decreasing the footprint of synthetic polymers.

The addition of small amounts of a catalyst (2 % wt.) enabled the complete curing of PCO:hardener thermosets at room temperature without any significant change in its properties. Therefore, eliminating the thermal curing (stoving conditions), a production process with lower energetic consumption is possible, moving towards more environmentally friendly technologies.

PCO-based films were used as adhesive films on aluminum substrates pretreated with ZrO_2 layer deposited by EAD method. These films did not present adhesive failure with the substrate in pull-off adhesion tests, indicating a satisfactory adhesion of the dual layer system (ZrCC + PCO:Jeffamine thermoset)

to the aluminum surface. Moreover, the mechanical properties are clearly better for pure PCO-based thermoset than PCO/DGEBA blend films.

Altogether, this work introduces new environmental aspects regarding the replacement of conventional passivation techniques, generally used with aluminum substrates, by Zr-EAD method; and by the development of a new partial biobased thermoset polymer useful for coatings and adhesive applications. This implies in a lower environmental impact due to a cleaner manufacturing procedure in comparison to the standard conversion coatings and in the use of bio-based feedstock in order to reduce the use of petroleum derivatives in epoxy thermoset formulations.

Further developments of this research may include the use of PLCO and PCO-based resins in the formulation of more commercial-like epoxy coatings and adhesives for aluminum substrate, including traditional additives from the coatings industry; and verify the coating system compatibility with different substrates.

Appendix A Computational image analysis as an alternative tool for the evaluation of corrosion in salt spray test

SUMMARY

The current standards for evaluating corrosion during salt spray tests rely on the visual analysis of the specimens, and this may be a limitation when higher resolution quantitative outputs are desired. In the work presented in this chapter, computational image analysis was used to measure the area affected by corrosion during salt spray tests with aluminum alloy, copper, carbon steel and galvanized steel plates. The software ImageJ was used to select and measure the corroded areas differentiating the corrosion products from the metals' uncorroded surfaces according to their different colors. With ten measurements for each selected exposure time, a 95 % confidence interval was calculated for each material and time of exposure, giving an indication of the precision of the estimated corroded area. These data were compared with a visual inspection carried out by an experienced technician following the current standards. The results indicate that computational image analysis may be a powerful tool to obtain higher resolution in the results interpretation in comparison with the standard visual analysis.

Publication derived from this work:

Moreira, V. B.; Krummenauer, A.; Ferreira, J. Z.; Veit, H. M.; Armelin, E.; Meneguzzi, A. Computational Image Analysis as an Alternative Tool for the Evaluation of Corrosion in Salt Spray Test. Stud. Univ. Babes-Bolyai Chem. 2020, 65 (3), 45–61. https://doi.org/10.24193/subbchem.2020.3.04

A.1 *Introduction*

Although salt spray is extensively used as a comparative corrosion test, its outcome may be limited by the current standards. Corrosion evaluation standards, such as ASTM D610–08, which uses visual examples as reference for comparison and subsequent rating of corrosion grades, are based on visual analysis. As such, they add some uncertainty to the results due to the adoption of subjective criteria and lowering the results resolution by limiting the outcome to an interval from 0 (zero) to 10, a discrete scale based on the estimate percentage of corroded area.

Computational image analysis may be an alternative to overcome this limitation by obtaining higher resolution data in order to improve the comparative investigation. One example was the standard D 7087-5a (2010) issued by ASTM International, in which a procedure for measuring rust creepage at scribe by an imaging technique was reported. However, the withdrawal of this standard in 2019 showed that there are still challenges to be tackled in order to provide reliable methods for computational corrosion evaluation.

In a recent work, Denissen and Garcia[1] used iterative algorithms in the computational image analysis during electrochemical impedance spectroscopy (EIS) tests in order to obtain complementary interpretation for such tests, showing the relevance of adequate assessment of the visible changes in the materials surface as an evidence of corrosive processes. Other authors[2–4] have already used image analysis for measuring corroded areas after corrosion tests. Although the successful use of those tools, there are no studies regarding the uncertainty of such analyses, from a statistical point of view, in salt spray tests.

Moreover, uncoated bare metal surfaces are not considered by the current corrosion evaluation standards. The inspection of the samples is usually limited by weight loss and corrosion analyses localized on the scribe of painted panels. Iribarren et al.[5] have demonstrated that dark and colored iron oxides and oxyhydroxides are associated with advanced carbon steel

deterioration, due to their non-adherent properties and high permeability to ions. Therefore, the use of color evaluation not only allows to distinguish the uncorroded and corroded zones, but also indicates the severity of the corrosive process which the material has undergone. Based on such examples, colors enable the use of image analysis tools to measure the fraction of the specimens' surface affected by corrosion.

In this work, salt spray tests were carried out with bare plates of four different metals: aluminum alloy, copper, carbon steel and galvanized steel. These specimens were evaluated periodically using ImageJ software (National Institutes of Health, Bethesda, Maryland, USA) in order to quantify the area affected by corrosion on each sample and perform the statistical analysis of the measurements. The observed results are represented in terms of failed area (%) versus the time of salt spray exposition, for each material. These plots were used to assess and to compare the 95 % confidence intervals (CI), of the means of different datasets.[6]

For first time, the statistical reliability of the proposed technique, has been addressed. The main aim of such validation is to introduce a novel evaluation method in order to obtain high resolution results after conventional corrosion tests. The method can be extended to other destructive tests used for coatings and surface characterization, such as adhesion tests, blistering evaluation, and others.

A.2 *Materials and Methods*

A.2.1 Metallic samples

The metal plates used for this work were: aluminum (AA7075-T6; 80 mm x 40 mm x 3 mm), copper (UNS – C11000; 100 mm x 40 mm x 1 mm), carbon steel (AISI 1020; 100 mm x 50 mm x 1 mm) and galvanized steel (100 mm x 50 mm x 1 mm).

Such metals were chosen due to the different surface contrast (by color) they present, as well as, due to the different contrast of their corrosion products.

Aluminum provides a bright gray substrate with the formation of white corrosion products, which may not be easily distinguishable by visual analysis. Copper, as well as galvanized steel, may form more than one single corrosion product. Carbon steel, besides being one of the main structural materials for engineering applications, also form different corrosion products, with different colors. Therefore, its study is important for a broader application of the proposed technique.

A.2.2 Preparation of metallic samples

All samples were degreased during 10 minutes at 70 °C with an industrial alkaline degreaser (Saloclean 667N – Klintex Insumos Industriais Ltda.) and subsequently washed with distilled water to eliminate the excess of degreaser agent.

Three specimens of each metal were tested. Individual specimens are referred to throughout this manuscript as: Al #, for aluminum alloy; Cu #, for copper; CS #, for carbon steel; GS #, for galvanized steel, being # a number from 1 to 3 that refers to the specimen tested.

A.2.3 Salt spray test

Salt spray tests were carried out according to ASTM B117. Four analysis times were selected for each metal for the image analysis: 164 h, 380 h, 476 h and 644 h for aluminum; 476 h, 716 h, 1052 h and 1388 h for copper; 1 h, 2 h, 3 h and 5 h for carbon steel; 2 h, 5 h, 10 h and 24 h for galvanized steel; and 0 (before salt fog chamber conditioning). Such time intervals were defined individually for each material due to the differences in their reactivity, so that a wide range of corrosion levels would be measured.

A.2.4 Computational image analysis

For the computational image analysis, each specimen was scanned using an image scanner (HP Color LaserJet CM1312 MPF - Hewlett-Packard Company) as an important tool to eliminate the effect of picture perspective; which cannot be neglected if conventional photographs are used.

For image analysis, the "Color threshold" function was used. The desired area was selected and was measured by setting the adequate parameters in hue,

saturation and brightness (HSB color system), after eliminating the edges and holes of the specimens and evaluating the visible corrosion products. Specifically for carbon steel specimens, the Red, Green and Blue (RGB) color system was more adequate for selecting the correct areas. This measurement was repeated ten times for each sample and time, adjusting manually the parameters for each one of them in order to measure experimental error. These parameter adjustments were made for each repetition independently, without necessarily matching the previous measurements for the same specimen, allowing the evaluation of the experimental variability, shown graphically in the interval plots. **Figure A.2.1** illustrates this procedure for one aluminum plate.

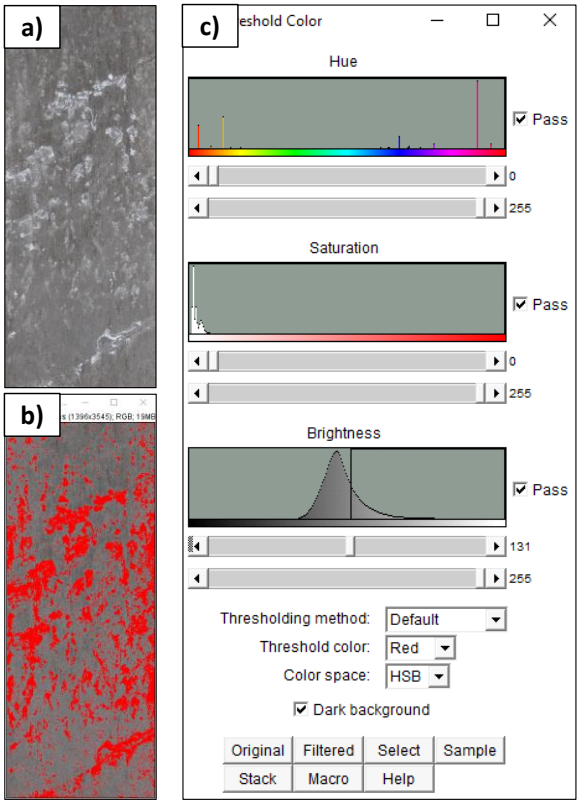

Figure A.2.1. a) Aluminum sample with white corrosion products after salt spray test; **b)** ImageJ screen during color threshold adjustments for selecting the corroded area (in red); **c)** Parameters adjustments screen for color threshold in HSB color system.

The 95 % confidence interval (CI) were calculated using the software Minitab 17 (Minitab Inc., USA) by the statistical inference for small samples (less than 30

measurements) that uses the t distribution, also referred to as Student's t distribution. These CI are defined by the lower confidence limit (LCL) and the upper confidence limit (UCL), which are calculated using the **Equations [1]** and **[2]**, respectively.[7]

$$LCL = \bar{x} - t \cdot \frac{s}{\sqrt{n}} \quad \textbf{[1]}$$

$$UCL = \bar{x} + t \cdot \frac{s}{\sqrt{n}} \quad \textbf{[2]}$$

Where $\bar{x}$ represents the sample mean, s stands for the sample standard deviation, n is the number of measurements and t is a factor depending on the degrees of freedom ($\nu = n - 1$) and the significance level (α). This way, being calculated for each sample at each time, the length of the CI is a measurement of the precision of the estimate value for the corroded area.[7]

Each interval plot shows the results for a single material, with three analyzed samples and five different exposure times on the salt spray test. These plots were generated by the software Minitab 17. The whiskers show the lower and upper confidence limits, while the center marker indicates the mean value for the group.[6]

With the lack of adequate standards for evaluating corrosion in uncoated bare metal samples, an adapted version of the ASTM D610 standard, which describes the practice for evaluating degree of rusting on painted steel surfaces by visual inspection, was used in order to compare to the computational image analysis proposed in the present study. The adaption of the standard was made comparing the test images of bare plates with the standard images for painted plates. Then, the corroded area was evaluated as if it was a paint failure area. Each specimen is then associated to a corresponding corrosion grade from 10 (0 % of corroded area) to 0 (zero, > 50 % of corroded area) in each evaluation time.

A.3 *Results and discussion*

A.3.1 Aluminum

Aluminum corrosion product is known to be white; therefore, it can be adequately identified by adjusting the brightness threshold. The interval plot of the measurements carried out in aluminum samples is depicted in **Figure A.3.1**.

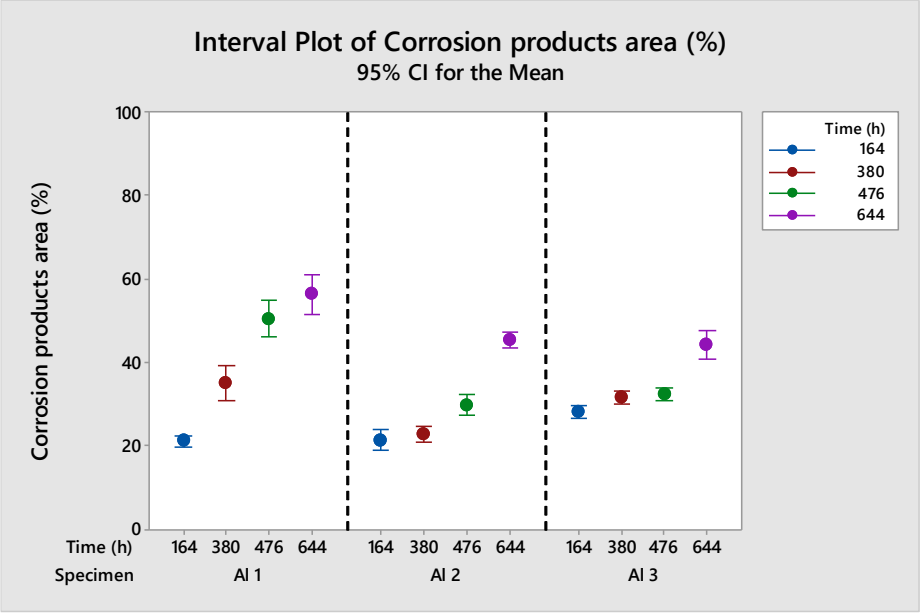

Figure A.3.1. Interval plot of measurements performed in aluminum alloy samples using color threshold function on ImageJ. CI means the confidence interval of 95 % obtained by statistical analysis.

The visual aspect of white aluminum oxide formed changed throughout the test duration, being evidently enlarged over increasing salt fog exposition time, as can be seen in **Figure A.3.2**.

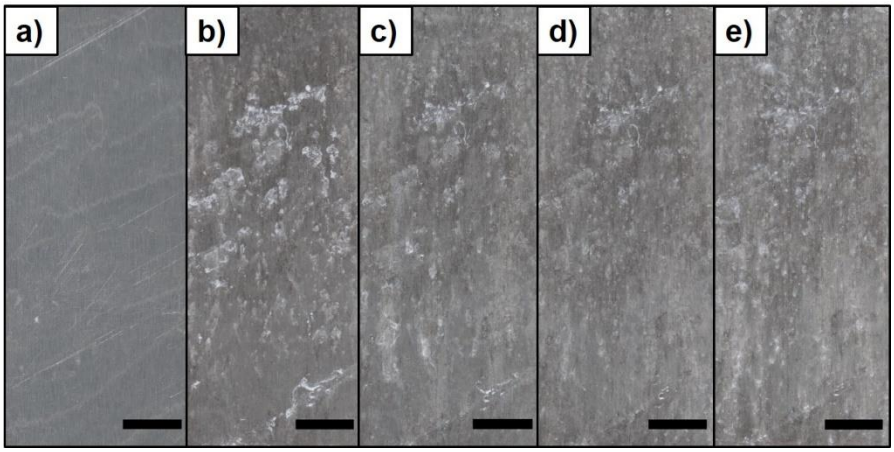

Figure A.3.2. Aluminum sample (Al 1) during visual analysis **a)** before the test, **b)** after 164 h, **c)** 380 h, **d)** 476 h and **e)** 644 h. The bars correspond to 1 cm.

It is noticeable that the corrosion products formed above the aluminum alloy surface, clearly delineated after 164 h of test, became less distinguishable assuming the aspect of the large stains with less brightness (light gray in color) in the following measurements. Therefore, the reduction of well-defined white oxides may be the reason why the data dispersion was increased for 380 h, 476 h and 644 h; resulting in broader confidence intervals. Those confidence intervals varied from 2.9 % for 164 h to 9.7 % for 644 h, for the sample Al 1; which are the lowest and the highest length of CI, respectively, for all measurements carried out in aluminum.

The comparison between the dispersion observed for Al 1 and Al 3 in the 380 h analysis confirms this hypothesis, once Al 3 still has well delineated corroded areas at this point, which does not occur with the sample Al 1. Comparison of both specimens is shown in the photograph images of **Figure A.3.3**.

Despite the difficulty imposed by the mentioned factor, the corroded areas are mostly statistically distinct and significant increases were observed for all samples during the test, as expected.

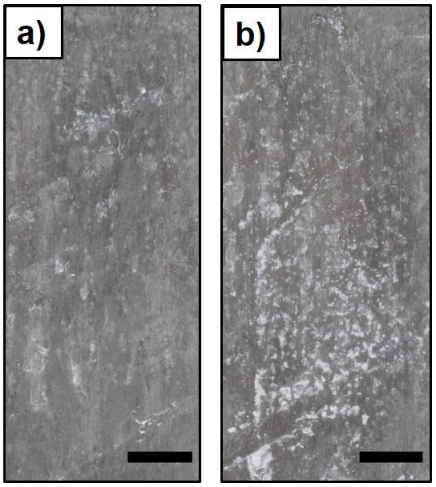

Figure A.3.3. Visual aspect of the surface of: **a)** Al 1 and **b)** Al 3 specimens, after 380 h of exposure on salt spray.

Figure A.3.4 consists in a graphical comparison between the values measured using the ImageJ computer software and the values of corrosion grade, obtained with an adapted version of the standard ASTM D610 (described in the experimental section), for each aluminum sample.

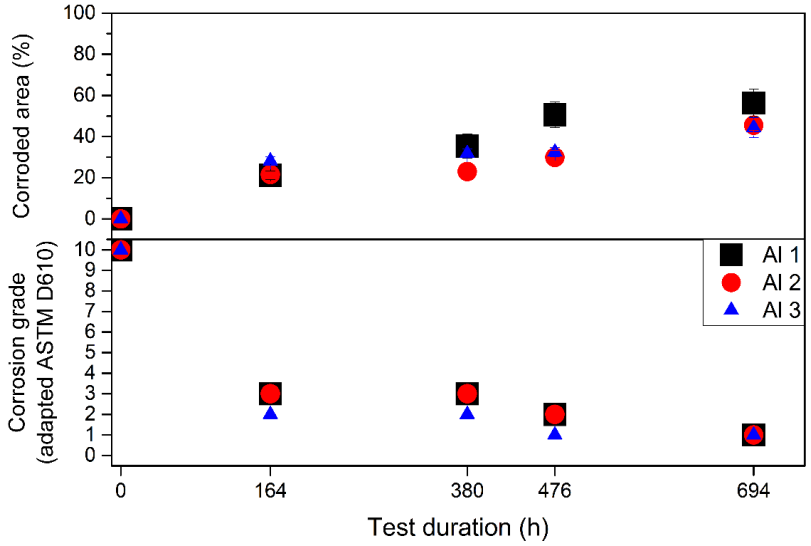

Figure A.3.4. Comparison of the computational measure using the ImageJ software (above) and the corrosion grade obtained with the standard ASTM D610 (below) for aluminum specimens.

The corrosion grade measured for the aluminum specimens decreased from 3 to 2 at the first salt spray exposition (164 h), and then decreased more slowly until grade 1 at the end of the test. This sharp exponential curve decrease traduces in a less accurate measure for the samples with more corroded area, once the interval for the failed area does not allow differentiating a fine corrosion grade, in the ASTM D610 standard. On the other hand, the image analysis by adjusting the brightness for identifying the white aluminum oxides offers a linear ascending curve. This effect is noticeable during the test at 694 h, as the computational analysis provides distinct areas while the visual inspection, following the ASTM D610 criteria, results in the same corrosion grades for the three samples studied. Thus, the computational measure ensures a statistically relevant difference of approximately 20 % in the corroded area of these specimens. This can be explained because the standard corrosion grades regard only corrosion up to 50 % in total area, so it was expected that for higher corroded areas the visual analysis could not provide adequate differentiation.

A.3.2 Copper

Considering the testing environment, the possible corrosion products from copper and their respective colors are: Cu_2O (red); CuO (black); $Cu(OH)_2$ (blue); and, possibly, CuCl after the replacement of oxygen by chloride ions in Cu_2O composition, changing it to a yellow colored layer.[8,9]

The scan images of one copper specimen (Cu 1) are depicted in **Figure A.3.5**.

In the first exposition time (476 h), remembering that either the salt fog spray exposition or the adjustments for the image analysis were not the same for each metal, the corrosion products were predominantly light red, and they were adequately selected by setting the saturation spectrum and allowing the establishment of the appropriate hues and brightness values. After 476 h, the predominant color of the corrosion products was a dark shade of red, possibly a mixture of CuO and Cu_2O, with some blue areas, possibly from $Cu(OH)_2$. Those corrosion products are easily distinguished from the substrate by the control of the brightness values for all hue and saturation spectra.

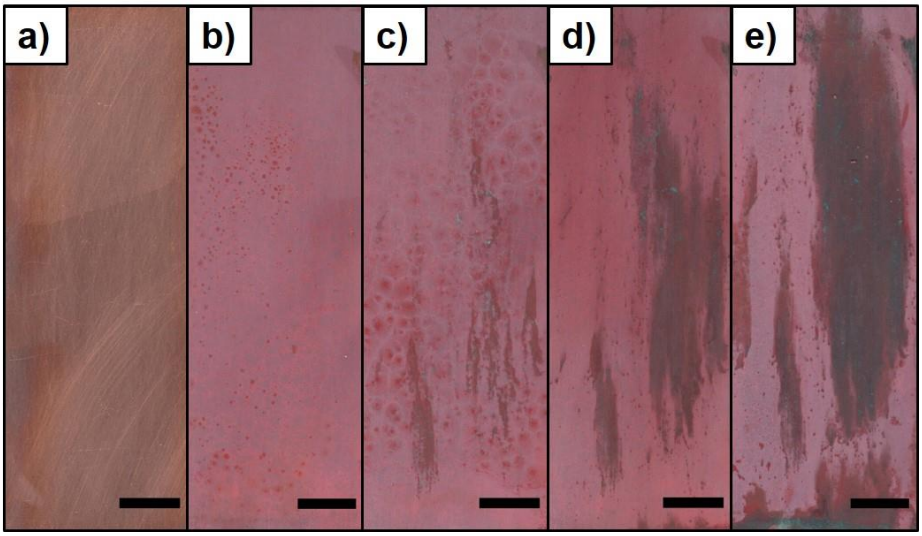

Figure A.3.5. Copper sample (Cu 1) during visual analysis **a)** before the test, **b)** after 476 h, **c)** 716 h, **d)** 1052 h and **e)** 1388 h. The bars correspond to 1 cm.

The interval plot for all measurements performed in copper samples is presented in **Figure A.3.6**.

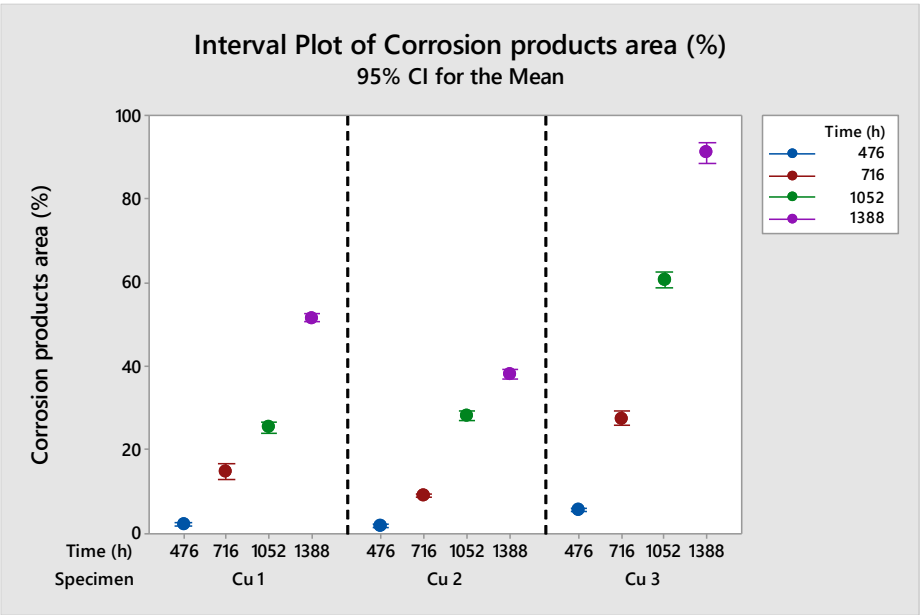

Figure A.3.6. Interval plot of the measurements carried out in copper specimens using color threshold function on ImageJ. CI means the confidence interval of 95% obtained by statistical analysis.

The clear visual distinction of the corrosion products by color has influenced the data dispersion. The three analyzed specimens showed significant differences regarding the evolution of the corrosive process, but even with the observed differences all samples had a narrow data dispersion, indicating the reliability of our analysis method. The lowest length of CI for copper samples was observed for Cu 2 after 476 h, which was only 0.5 %; while the highest value was obtained for the sample Cu 3, 5.1 % length of CI. It is also noticeable that there are statistically significant differences for all of the points measured for each sample, indicating the expected evolution of the corroded area for all the specimens.

A graphical comparison between the computational image analysis and the visual inspection of copper corrosion products by using the adapted version of ASTM D610 is shown in **Figure A.3.7**.

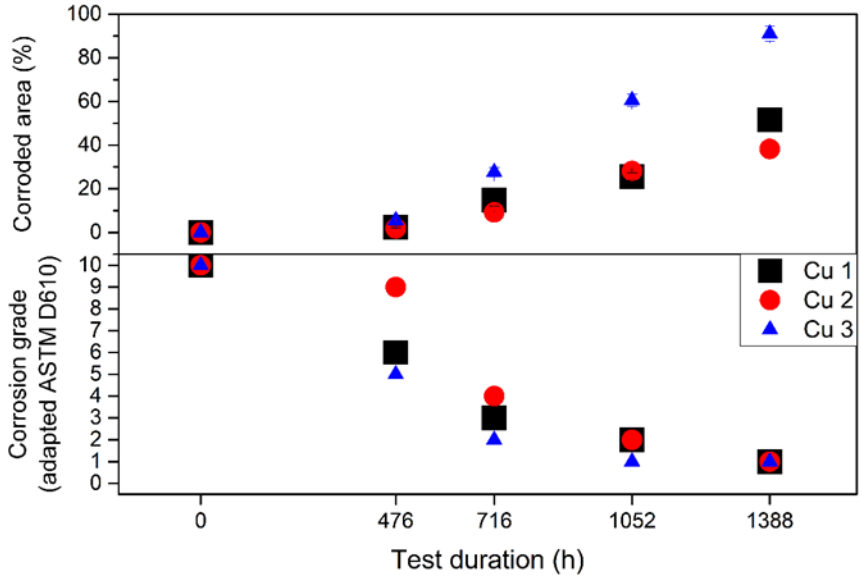

Figure A.3.7. Comparison of the computational measure using the ImageJ software (above) and the corrosion grade obtained with the standard ASTM D610 (below) for copper specimens.

As observed previously in the aluminum specimens (**Figure A.3.4**), the corrosion grade from the ASTM D610 fails again to differentiate samples with large corroded areas, while computational image analysis detects significant differences between the samples. One example of this evidence is the evolution of corrosion in sample Cu 3, which increased only one corrosion grade from 716 h

to 1388 h after testing. Computational image analysis showed that, in the same time interval, this increase corresponds to an evolution of approximately 60 % more of copper oxide products respect to the total of the corroded area.

A.3.3 Carbon steel

The images used for the evaluation of one of the carbon steel samples (CS 1) throughout the test can be seen in **Figure A.3.8**.

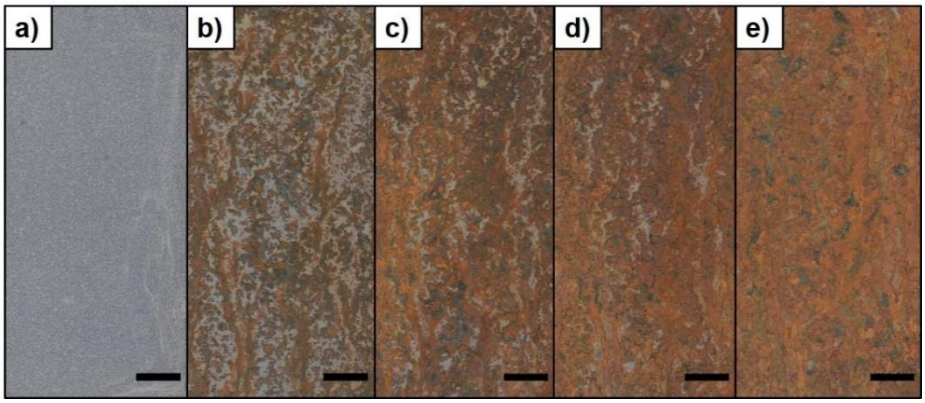

Figure A.3.8. Carbon steel sample (CS 1) during visual analysis **a)** before the test, **b)** after 1 h, **c)** 2 h, **d)** 3 h and **e)** 5 h. The bars correspond to 1 cm.

For carbon steel samples the HSB color system adjustment fails for selecting the darker areas. Therefore, the RGB color system was chosen, and it offers a more efficient setting by limiting the green spectrum to a desired value and allowing the entire red and blue spectra to be selected, as observed experimentally. The interval plot of the performed measurements is shown in **Figure A.3.9**.

Carbon steel presents many corrosion products within a wide color range. For more details regarding the correlation among the oxides and oxyhydroxides products and specific colors, please, refer to the references.[5,10,11] The mean value of the corroded area was higher than 60 % for all of the analyzed time intervals for all the specimens. These large areas did not lead to inconsistent data dispersion, with the lengths of CI being very low, between 1.1 % and 4.1 % for all samples. This range of lengths of CI is similar to that one observed for copper samples (with exception of Cu 3). As observed in copper analyses, the high contrast between the corrosion products and the bare metal substrate results in a narrow data dispersion once the visual distinction is facilitated.

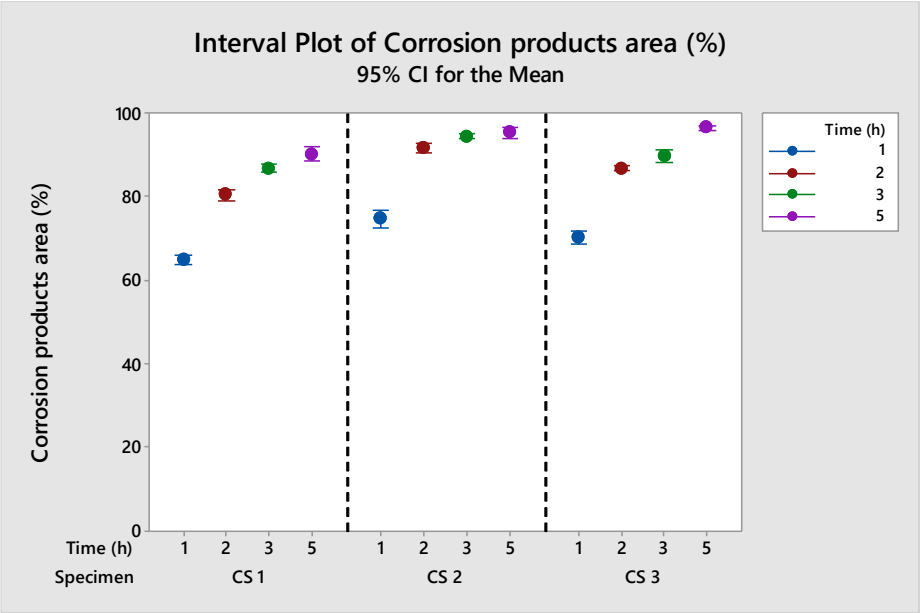

Figure A.3.9. Interval plot of measurements performed in AISI 1020 steel samples using color threshold function on ImageJ. CI means the confidence interval of 95 % obtained by statistical analysis.

The graphical comparison between the proposed technique and the visual analysis offered by ASTM D610 of carbon steel specimens is shown in **Figure A.3.10**.

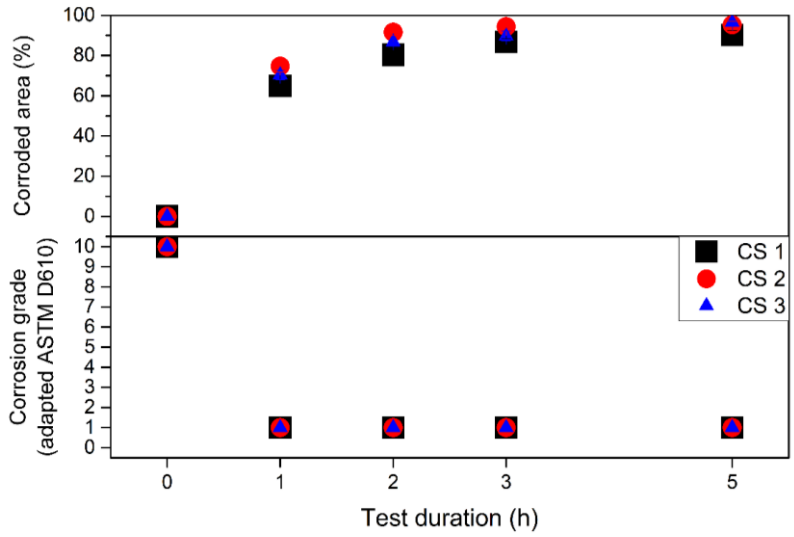

Figure A.3.10. Comparison of the computational measure using the ImageJ software (above) and the corrosion grade obtained by with the standard ASTM D610 (below) for carbon steel specimens.

As can be seen in the **Figure A.3.10**, the corrosion grade obtained with visual analysis (ASTM D610) resulted in no differentiation for large corroded areas, reaching the maximum rating number of 1 for any exposition time in salt spray test. By contrary, the corroded area measured with the computational image analysis indicated an exponential rise of the corroded area up to approximately 30 % from 1 h to 5 h of test. Altogether evidence that the computational software ImageJ can be used to achieve comparisons that are more accurate.

A.3.4 Galvanized steel

The corrosion products formed in galvanized steel are initially white, corresponding to ZnO molecules, and, after a severe corrosion of the zinc layer, red corrosion products are visible as a result of the underlying carbon steel corrosion process, as observed in **Figure A.3.11**, which contains the analyzed images of a galvanized steel specimen (GS 1).

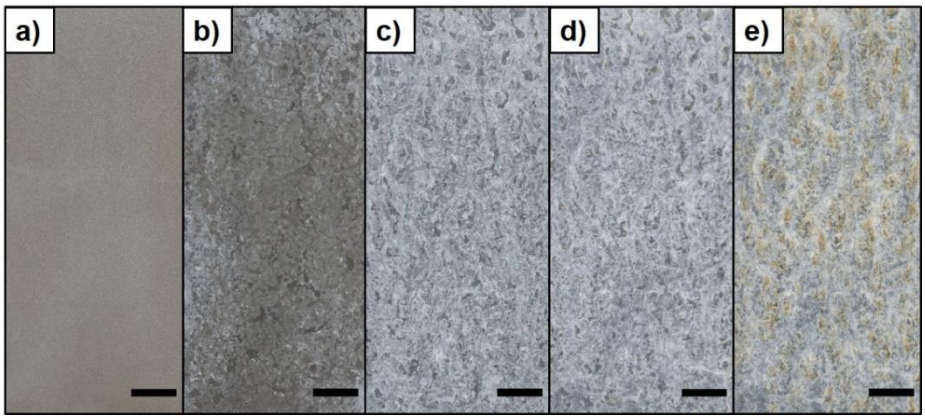

Figure A.3.11. Galvanized steel sample (GS 1) during visual analysis **a)** before the test, **b)** after 2 h, **c)** 5 h, **d)** 10 h and **e)** 24 h. The bars correspond to 1 cm.

For the measurements carried out on galvanized steel specimens, the adjustment of the brightness was efficient for selecting the corroded area. The resulting interval plots are depicted in **Figure A.3.12**.

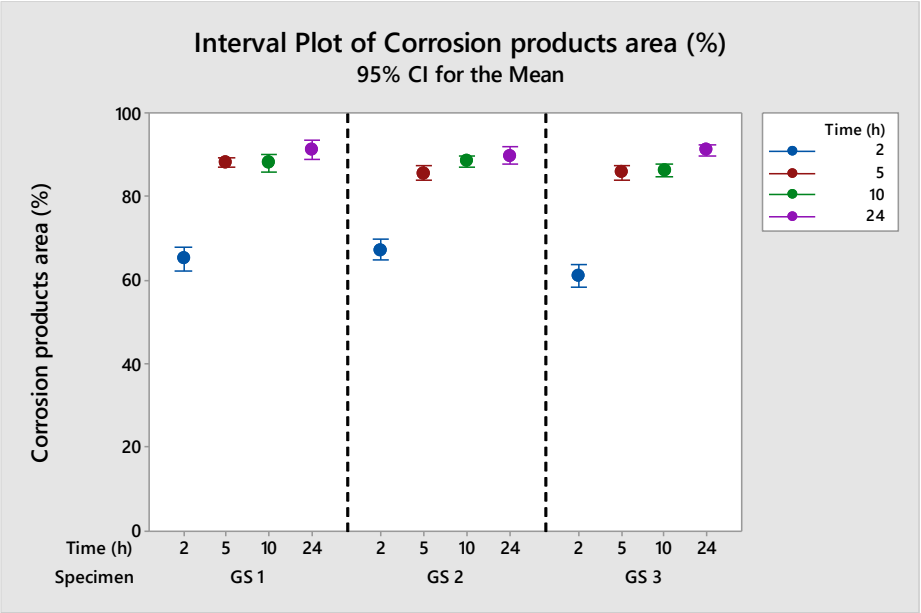

Figure A.3.12. Interval plot of measurements performed in galvanized steel samples using color threshold function on ImageJ. CI means the confidence interval of 95 % obtained by statistical analysis.

Differently from that observed in aluminum, the white corrosion products on galvanized steel do not have a significant change regarding their visual aspect, i.e. the corroded areas on galvanized steel are more clearly delimited with the evolution of the corrosive process than in aluminum alloy. In other words, the specific corroded areas that are visible in the first analysis time remain well defined until the end of the test. This has resulted in a narrow data dispersion on larger testing times.

Although some of the measurements for 5 h, 10 h and 24 h in salt fog test are statistically equivalent, this is a result of a stabilization in the corrosion evolution on the tested specimens. Between 5 h and 24 h the CI length did not exceed 4.7 % for all samples, which indicates that even with large corroded areas the computational method may provide significant data. The lowest and the highest lengths of CI observed for galvanized steel were 2.3 % and 5.8 %, respectively.

Figure A.3.13 shows the graphical comparison between both the image and the visual analyses, obtained from adapted ASTM 610, for galvanized steel specimens.

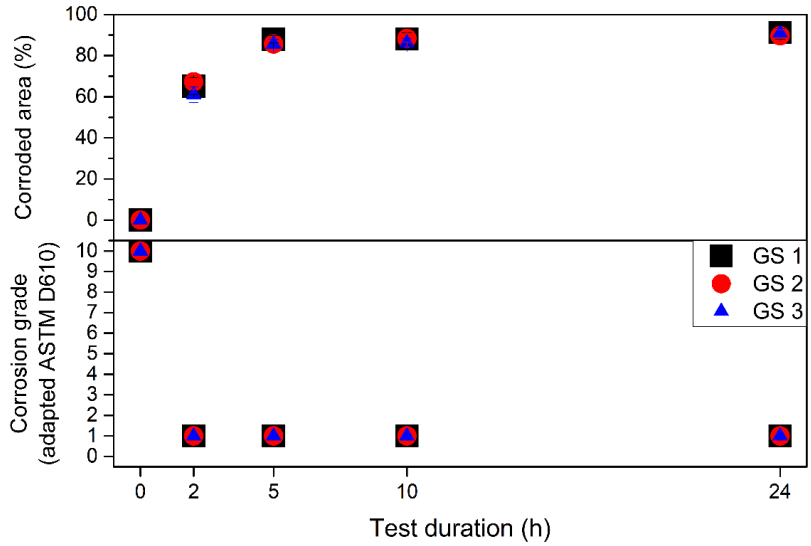

Figure A.3.13. Comparison of the computational measure using the ImageJ software (above) and the corrosion grade obtained with the standard ASTM D610 (below) for galvanized steel specimens.

If we compare the **Figure A.3.10** and **A.3.13** (lower plots), it can be seen that there are no differences on the evaluation of the corroded area between carbon steel and galvanized steel, by using ASTM D610 visual inspection. Nevertheless, the fast increase of corrosion areas from the first measurement (65 %, 2 h) towards the second time (88 %, 5 h) in the galvanized samples (**Figure A.3.13**, upper plot) was discriminated by the computational image analysis. It corresponds to the elimination of the ZnO layer and the starting of under layer corrosion, which is more similar to that reported for the carbon steel (**Figure A.3.10**, upper plot).

A.4 *Conclusions*

The use of a computational image analysis to measure corroded areas during salt spray test resulted in higher differentiation between specimens with statistically significant difference at 95 % confidence level for all the tested metals, if compared to the visual inspection suggested by ASTM D610 standard. Among the different metal compositions, a clear linear curve of corroded area over time was found to

aluminum alloy and copper substrates, whereas the carbon steel and the galvanized steel showed an exponential increase of corrosion rate.

Thus, for first time, a reliable and reproducible method for the evaluation of corrosion products by contrast, brightness, hue and saturation adjustment after salt spray test was demonstrated, which will undoubtedly enrich the interpretation of the data obtained from such assays.

This technique may enable differentiation in the performance of materials that would not be measurable with the conventional evaluation methods, providing a quantitative character to such experiment, which is typically limited by the intrinsically qualitative aspect of simple visual analysis.

It must be mentioned that the proposed method is limited by the ability of acquiring representative two-dimensional images of the tested surfaces with no dimensional distortions. In this way, complex three-dimensional shapes inevitably introduce misleading inputs, as affected areas may appear smaller with increasing distance to the image foreground. Additional image processing or alternative image acquisition methods would be necessary to overcome this limitation.

The authors expect to set ground for further developments in the improvement of accelerated corrosion analysis, as the technique herein described can be applied to other tests, such as immersion or 100 % relative humidity tests. This can be also the initial step towards the development of automated corrosion evaluation by computational image analysis in accelerated corrosion tests. The new insights presented here can be extended to other destructive analyses, like those performed on coatings industry (pull-off test, blistering, rust creepage at scribe, and others).

A.5 *References*

(1) Denissen, P. J.; Garcia, S. J. Reducing Subjectivity in EIS Interpretation of Corrosion and Corrosion Inhibition Processes by In-Situ Optical Analysis. *Electrochim. Acta* **2019**, *293*, 514–524. https://doi.org/10.1016/j.electacta.2018.10.018.

(2) Rodošek, M.; Koželj, M.; Slemenik Perše, L.; Cerc Korošec, R.; Gaberšček, M.; Surca, A. K. Protective Coatings for AA 2024 Based on Cyclotetrasiloxane and Various Alkoxysilanes. *Corros. Sci.* **2017**, *126* (June), 55–68. https://doi.org/10.1016/j.corsci.2017.06.011.

(3) Daure, J. L.; Voisey, K. T.; Shipway, P. H.; Stewart, D. A. The Effect of Coating Architecture and Defects on the Corrosion Behaviour of a PVD Multilayer Inconel 625/Cr Coating. *Surf. Coatings Technol.* **2017**, *324*, 403–412. https://doi.org/10.1016/j.surfcoat.2017.06.009.

(4) Chen, X.-B.; Birbilis, N.; Abbott, T. B. Effect of [Ca^{2+}] and [$(PO_4)^{3-}$] Levels on the Formation of Calcium Phosphate Conversion Coatings on Die-Cast Magnesium Alloy AZ91D. *Corros. Sci.* **2012**, *55*, 226–232. https://doi.org/10.1016/j.corsci.2011.10.022.

(5) Iribarren, J. I.; Liesa, F.; Meneguzzi, Á.; Alemán, C.; Armelin, E. Spectroscopy Investigations Reveal Unprecedented Details in the Corrosion of AISI 1012 UPN Profiles Installed in a Modernist Building of Beginning of 20th Century. *J. Cult. Herit.* **2020**, *42*, 240–248. https://doi.org/10.1016/j.culher.2019.08.006.

(6) Gardiner, W. P. *Statistical Analysis Methods for Chemists*; Royal Society of Chemistry: Cambridge, 2007. https://doi.org/10.1039/9781847551924.

(7) Montgomery, D. C.; Runger, G. C. *Applied Statistics and Probability for Engineers*, 6th editio.; John Wiley and Sons Inc, Ed.; Hoboken, USA, 2014.

(8) Groysman, A. *Corrosion for Everybody*; Springer Netherlands: Dordrecht, 2010. https://doi.org/10.1007/978-90-481-3477-9.

(9) Sathiyanarayanan, S.; Sahre, M.; Kautek, W. In-Situ Grazing Incidence X-Ray Diffractometry Observation of Pitting Corrosion of Copper in Chloride Solutions. *Corros. Sci.* **1999**, *41* (10), 1899–1909. https://doi.org/10.1016/S0010-938X(99)00021-9.

(10) Antunes, R. A.; Costa, I.; Faria, D. L. A. de. Characterization of Corrosion Products Formed on Steels in the First Months of Atmospheric Exposure. *Mater. Res.* **2003**, *6* (3), 403–408. https://doi.org/10.1590/S1516-14392003000300015.

(11) Antunes, R. A.; Ichikawa, R. U.; Martinez, L. G.; Costa, I. Characterization of Corrosion Products on Carbon Steel Exposed to Natural Weathering and to Accelerated Corrosion Tests. *Int. J. Corros.* **2014**, *2014*, 1–9. https://doi.org/10.1155/2014/419570.